ISSN 0038-531X

Russian Original Vol. 49, No. 3, September, 1980

March, 1981

SATEAZ 49(3) 603-656 (1980)

SOVIET ATOMIC ENERGY

АТОМНАЯ ЭНЕРГИЯ
(ATOMNAYA ÉNERGIYA)

TRANSLATED FROM RUSSIAN

CONSULTANTS BUREAU, NEW YORK

SOVIET ATOMIC ENERGY

Soviet Atomic Energy is a translation of *Atomnaya Énergiya*, a publication of the Academy of Sciences of the USSR.

An agreement with the Copyright Agency of the USSR (VAAP) makes available both advance copies of the Russian journal and original glossy photographs and artwork. This serves to decrease the necessary time lag between publication of the original and publication of the translation and helps to improve the quality of the latter. The translation began with the first issue of the Russian journal.

Consultants Bureau journals appear about six months after the publication of the original Russian issue. For bibliographic accuracy, the English issue published by Consultants Bureau carries the same number and date as the original Russian from which it was translated. For example, a Russian issue published in December will appear in a Consultants Bureau English translation about the following June, but the translation issue will carry the December date. When ordering any volume or particular issue of a Consultants Bureau journal, please specify the date and, where applicable, the volume and issue numbers of the original Russian. The material you will receive will be a translation of that Russian volume or issue.

Subscription (2 volumes per year)
Vols. 48 & 49: $335 (domestic); $374 (foreign)
Vols. 50 & 51: $380 (domestic); $423 (foreign)

Single Issue: $50
Single Article: $7.50

Soviet Atomic Energy is abstracted or indexed in *Chemical Abstracts, Chemical Titles, Pollution Abstracts, Science Research Abstracts, Parts A and B, Safety Science Abstracts Journal, Current Contents, Energy Research Abstracts,* and *Engineering Index.*

CONSULTANTS BUREAU, NEW YORK AND LONDON

c/b
233 Spring Street
New York, New York 10013

Published monthly. Second-class postage paid at Jamaica, New York 11431.

SOVIET ATOMIC ENERGY

A translation of *Atomnaya Énergiya*

March, 1981

Volume 49, Number 3 September, 1980

CONTENTS

CONTENTS

(continued)

Engl./Russ.

The Russian press date (podpisano k pechati) of this issue was 8/22/1980. Publication therefore did not occur prior to this date, but must be assumed to have taken place reasonably soon thereafter.

ARTICLES

THE ENERGY SOURCE OF THE SUN

N. A. Vlasov

UDC 539.165.8:539.12...164

A remarkable rejuvenation and birth of new ideas has been taking place in solar physics in the last decade. The principal reason for this rejuvenation is the neutrino deficit detected in the observations of Davis [1] in comparison with the predictions based on the standard models of the sun. Attempts to achieve consistency of the calculations with the observations by revision of the standard models and reevaluation of the constants used in the calculations have not led to comforting results. The deficit has been maintained; therefore, researchers have begun to doubt the premises on which the standard models are based. Suggestions have appeared that the interior of the sun is appreciably richer in the heavy elements than the outer visible layers and that mixing of material is occurring in the solar interior. The more unexpected hypotheses have been directed towards searches for unknown effects, e.g., new particles or new types of interaction (in addition to the four known), the inclusion of the gravitational interaction of black holes, and assumptions of different neutrino transformations on the way from the sun to the earth. This abundance of hypotheses has created the impression of serious trouble in solar physics. Actually, the situation is not so alarming. It is true that some "first approximations" are in need of review, but many "lunatic" ideas are clearly unsound and scarcely deserving of discussion. On the other hand, observations are revealing new phenomena whose analysis promises real ways to resolve the problem.

Gravitation and Energy Sources in the Universe. The most powerful energy-generating processes in nature occur under the action of gravitational forces. Due to its universality and slow decline with distance, the gravitational interaction involves enormous masses of matter. The larger the masses of the bodies are, the more significant are the gravitational forces. We observe such effective phenomena as the burnup of meteors and the fall of meteorites already on such a small celestial body as the earth ($M = 6.6 \cdot 10^{27}$ g). On the moon and the planets large meteorites have formed craters and were in general one of the chief factors determining the nature of planetary evolution. The formation of the sun and the solar system occurred under the action of gravitational forces. It is almost indisputably recognized that the origin of all celestial bodies, planets, stars, intragalactic star clusters, galaxies, clusters of galaxies, and superclusters, is due to the gravitational contraction of matter. In the course of stellar evolution the gravitational contraction is slowed down at some stage by transformations of matter within the stars. But in the final evolutionary stages gravitational contraction turns out to be decisive. It leads to the formation of very dense objects: white dwarfs, neutron stars, and black holes. The formation of such objects is usually accompanied by large explosive processes of energy liberation — the outbursts of novae and supernovae. Although nuclear transformations, e.g., thermonuclear carbon burning, may be the direct cause of the explosions, gravitational contraction serves as the original energy source. In a supernova outburst of a star an enormous amount of energy is liberated — $\sim 10^{52}$ ergs ($1 \text{ erg} = 1 \cdot 10^{-7}$ J). A supernova emits more energy in a week than the sun does in its entire lifetime of 10^{10} years.

Even more immense energy releases are observed in some galaxies and the quasars. An amount of energy on the order of 10^{60} ergs $\approx 10^6 M_0 c^2$ equivalent to the rest energy of millions of suns, emerges in the form of the kinetic energy of dispersing masses of material, in the form of electromagnetic radiation of a broad spectral region from γ quanta to radio waves, and in the form of cosmic radiation. Thermonuclear reactions, in which tenths of a percent of the rest energy are released, seem insufficient for such immense conflagrations. It is necessary to "incinerate" an entire "galaxy of hydrogen" in thermonuclear reactions in order to cause such a conflagration. Whatever the mechanisms might be for the release of such great energy, there can be no doubt that it occurs due to gravitational contraction (approach) of large masses of material.

Translated from Atomnaya Énergiya, Vol. 49, No. 3, pp. 155-161, September, 1980. Original article submitted March 27, 1980.

0038-531X/80/4903-0603$07.50

Tenths of the rest energy can be released in the process of gravitational approach. For example, there exist states in the gravitational field of a rotating dense body to which a transition results in the radiation of $0.4Mc^2$ [2]. Consequently, the energy release in the process of gravitational contraction is more intense by one-two orders of magnitude than that in thermonuclear fusion.

Gravitational Energy of the Sun. It is supposed that the sun was formed out of a rarefied cloud of gas and dust. In the process of contraction of the cloud gravitational energy was released approximately in the amount $kGM_0^2/R_0 = 5.6 \cdot 10^{48}$ ergs (G is the gravitational constant, M_0 and R_0 are the mass and radius of the sun, and $k \approx 1$). This value depends in general on the final state of the sun, e.g., on the radial distribution of the mass, but reasonable variations of the distribution change the gravitational energy by less than a factor of two. If one divides the gravitational energy of the sun by the number of nucleons in it ($N = 1.2 \cdot 10^{57}$), the result can be assumed to be the average binding energy of a nucleon in the sun, which is equal to ~ 3.7 keV/nucleon.

The escape energy of a hydrogen atom from the surface of the sun (~ 2 keV) exceeds by more than two orders of magnitude the energy of the chemical bonds of hydrogen in molecules and condensed bodies but is $\sim 10^3$ times less than the energy of the nuclear bonds of a nucleon and $\sim 10^6$ times less than its rest energy.

If the luminosity of the sun were to be equal from the very start to its present luminosity $L_0 = 3.86 \cdot 10^{33}$ ergs/sec, the contraction energy of the sun would last $\approx 2 \cdot 10^{15}$ sec = $5 \cdot 10^7$ years. Special calculations with analysis of the evolution of the sun in the contraction stage do not alter the order of magnitude of this quantity. But the age of terrestrial, meteoritic, and lunar material determined by measurements of the radioactivity of uranium and other radioactive isotopes is no less than $4.5 \cdot 10^9$ years. There is no basis for assuming the sun to be younger than $4.5 \cdot 10^9$ years. It is clear that gravitational contraction to a reasonable present state could not provide the luminosity of the sun for billions of years. "Unreasonable" but conceivable states would be able to provide the luminosity of the sun by virtue of gravitational energy. For example, if one supposes that a compact object of the black-hole type were formed at the center of the sun, then one can maintain the power of the sun for billions of years due to the gradual capture by this central object of the surrounding material. During the lifetime of the sun the flow rate of capture material would amount to thousandths of the solar mass, i.e., several powers of ten less than the amount of hydrogen that would be consumed in thermonuclear reactions. The hypotheses in which the neutrino deficit is explained by the presence of black holes are based on such notions [3]. But at the present state of physics and astrophysics the introduction of black holes into the sun hardly seems necessary.

Already at the beginning of the present century guesses appeared that the source of the energy of the sun and the stars might be nuclear transformations. In the 1930s certain kinds of the necessary nuclear transformations were found, and a solid conviction developed that they are precisely what provides a lengthy and rather stable existence for the sun and the other stars in the evolutionary stage known as the main sequence. The relatively large energy release of nuclear transformations ($\sim 10^{-3}$ Mc^2), even in light of their very low probability, proves to be sufficient for the internal heating to prevent gravitational contraction for a long time. Gravitational contraction again comes into play and becomes the chief source of energy of subsequent transformations in stars of large mass after significant burning of the light nuclei. In the final stage of evolution a star may be transformed into one of three types of celestial bodies: a white (or dark) dwarf, a neutron star, or a black hole. The radius of the dwarf is ≈ 100 times less than that of the sun. The gravitational binding energy of a nucleon reaches 1 MeV in the dwarfs [4], i.e., less by approximately (in all only) an order of magnitude than the nuclear bonds of the nucleons. Just as in nuclear transformations, the binding energy is emitted in the form of quanta or particles. Upon the formation of dwarfs the gravitational energy already makes up the dominant fraction of the overall energy release of the star.

The release of gravitational energy is even more significant in connection with the formation of neutron stars. The binding of nucleons in neutron stars exceeds by one-two orders of magnitude the nuclear bonds; therefore, nuclear transformations play a secondary role in the formation of neutron stars. Actually, endothermic fissions of the most stable iron nuclei, which utilize part of the energy of gravitational contraction, predominate. Notwithstanding this fact, the formation of neutron stars leads to colossal explosions of the supernova outburst type.

The energy release in connection with the formation of black holes differs insignificantly from the energy release in connection with the formation of neutron stars. The radius of a solar-mass neutron star is three times larger in all than the so-called gravitational radius ($R_g = 2GM_\odot/c^2 \approx 3$ km), at which the gravitational force becomes irresistible.

The sun should be transformed into a white dwarf in several billion years. It does not have enough mass for transformation into a neutron star or a black hole. Consequently, in the evolution of the sun gravitational energy will add only a little bit in the late stages to what the thermonuclear burning of hydrogen will provide. Gravitational forces are important for the contemporary sun only as a counteraction to the internal pressure of the hot matter which determines its state. The equilibrium between internal pressure and gravitational contraction is usually disrupted in nonsteady stars, and vibrational or explosive phenomena are observed. The gravitational forces emerge here as an active beginning which affects the nature of the evolution.

We have become accustomed to considering the sun in its present state to be practically a stable star, although flares, vortices, spots, and so on are visible on its surface. The surface instabilities weakly affect the integrated luminosity. The so-called solar constant — the flux of solar energy per 1 cm^2 of the earth — has remained constant within 1% limits during astronomical measurements. But the duration and accuracy of the measurements of the solar constant are insufficient to exclude completely global irregularities. On the one hand, hypotheses have appeared in connection with the neutrino deficit concerning variability of the nuclear burning processes in the solar interior, and on the other hand — signs of powerful nonequilibrium processes have been detected by the latest contemporary measurements. The possibility is not excluded that some variations of the energy release are produced by mutual conversions of gravitational energy into thermal and vice versa. Theoretically possible methods of maintaining the energy release of the sun by virtue of gravitational contraction energy for billions of years seem improbable. Thermonuclear burning of hydrogen and light elements as the energy source of the sun and the stars is in such good agreement with numerous and diverse observations that there are no reasons to doubt it. Of course, refinements of the details of the process and variation of the steps of thermonuclear fusion are possible. But it is unthinkable to exclude thermonuclear fusion from the energy release and evolution of the stars.

Nuclear Transformations. Nuclear energy is released in the solar interior as a result of the conversion of hydrogen into helium. The principal cycle of nuclear reactions is as follows:

$$p + p \rightarrow d + e^+ + \nu; \quad d + p \rightarrow {}^3\mathrm{He} + \gamma;$$
$${}^3\mathrm{He} + {}^3\mathrm{He} \rightarrow {}^4\mathrm{He} + 2p.$$

Four protons are converted into an α particle. An energy of 26.7 MeV is released. The greater part of this energy is imparted to charged particles and photons and then is slowly carried out to the outer layers of the sun, from which it is emitted principally as visible light. A small part ($\sim$2%) of the energy is transported by neutrinos and carried off without hindrance by them to the far cosmos.

The initial reaction of the cycle is the β-decay of a pair of protons with their transformation into a deuteron. The decay occurs only at the brief instants of the approach of protons during collisions; therefore the probability of the decay is very small, and the transformation of hydrogen into deuterium proceeds very slowly. The sun owes its lengthy existence to this fact.

In addition to the hydrogen cycle of reactions noted above, there is still the Bethe carbon cycle. In it four protons are also transformed into an α particle with the help of catalyst nuclei of carbon and nitrogen. Also a pair of neutrinos occurs for each α particle, but their energy is somewhat larger and the spectrum is different. The role of the carbon cycle is small in the solar energy budget. This fact was clear already from the preliminary calculations of solar models and has been confirmed by the observations of Davis.

Notwithstanding the very slow process of hydrogen burning, it releases enough energy to maintain the luminosity of the sun. With a luminosity $L \approx 4 \cdot 10^{33}$ ergs/sec, $\approx 3.6 \cdot 10^{38}$ hydrogen atoms per second should be converted into helium. Their mass is $\Delta M \approx 5.7 \cdot 10^{14}$ g/sec. At this rate $\sim 8 \cdot 10^{31}$ g $= 0.04 M_\odot$ should be burned in $4.5 \cdot 10^9$ years. Consequently, in order to maintain the luminosity at the present level for $4.5 \cdot 10^9$ years, it is sufficient to convert a total mass of hydrogen of about 4% of the solar mass into helium.

The observations of Davis have raised doubts about the characteristics of the nuclear reactions occurring in the sun. Papers (e.g., [5]) have appeared in which possible errors in the calculations due to uncertainty of the original nuclear data are analyzed. The principal reason for the uncertainty lies in the fact that the majority of the values of the probabilities and cross sections of the reactions could not be verified directly by experiment but were obtained by extrapolation from known analogous phenomena or from a distant energy region.

The initial reaction $p + p \rightarrow d + e^+ + \nu$ has such a small cross section that there have not yet been attempts to observe it in the laboratory. The cross section is determined on the basis of data on pp-scattering at low energy which characterize the initial state and from an estimate of the matrix element of the β transition which has been determined for other nuclei, in particular for a free neutron. Refinement of the data on the period of neutron decay may affect the adopted value of the cross section of the reaction.

The other subsequent nuclear reactions could also not be observed directly in the laboratory, and their cross sections are obtained by a distant extrapolation in the energy. The thermal energy of particles at the center of the sun is on the order of 1 keV, but the Coulomb barrier for a proton is 100 keV in the best case, and the energy range accessible for laboratory measurements starts near 1 MeV. Uncertainty in the extrapolation can have a significant effect on the calculations for the yield of the different branches of the cascade of nuclear reactions, in particular, on the yield of ^8B nuclei, which is significant for the neutrino measurements. In this connection, a suggestion has been made about a resonance of the $^3He + ^3He$ reaction and the inaccuracy of the extrapolation of the cross section of the $^7Be + p$ reaction.

An analysis of the possible changes of the adopted nuclear data has not led to agreement of the standard solar model with the observations of the neutrino flux [6]. It has not proved possible to explain the neutrino deficit by errors in the determination of the nuclear constants.

Solar Neutrinos. The total flux of solar neutrinos ($\sim 2 \cdot 10^{38}$ ν per second) is easily estimated by knowing that a pair of neutrinos is necessary for each 26 MeV of emitted energy. A flux of $6.5 \cdot 10^{10}$ $\nu/(cm^2 \cdot sec)$ is incident on the surface of the earth. This number is known rather reliably. Neutrinos carry off only a small (2-3%) fraction of the energy, and its uncertainty is almost insignificant in the energy balance of the sun. But the nature of the neutrino spectrum is very important for their observation. The probability of recording neutrinos depends very strongly on their energy. The setup of Davis with a chlorine detector is practically insensitive to the neutrinos of the hydrogen cycle and has been designed to record the neutrinos of the clearly low-probability secondary reactions.

The threshold of the $^{37}Cl(\nu, e^-)^{37}Ar$ reaction ($\sim$0.814 MeV) exceeds the limit of the neutrino spectrum of the $p + p \rightarrow d + e^+ + \nu$ reaction (0.412 MeV), and the reaction $2p + e^- \rightarrow d + \nu$, which is less probable only by a factor of several hundred, gives neutrinos with an energy of 1.442 MeV, which exceeds the threshold of the detector. Along with the main reaction $^3He + ^4He \rightarrow ^7He + 2p$, the reactions $^3He + ^4He \rightarrow ^7Be + \gamma$ and $^7Be + p \rightarrow ^8B + \gamma$ and the decay $^8B \rightarrow ^8Be + e^+ + \nu$ are possible. An emitter of very energetic neutrinos — ^8B — is found in this chain of reactions. The limit of the spectrum of $\nu(^8B)$ is equal to 14 MeV, and the average energy is 7.4 MeV.

The neutrino deficit observed by Davis refers primarily to the ^8B neutrinos. Undoubtedly, there are fewer of them by several times than would be expected in the standard models. The newest data are as follows: 6-7 SNU were expected [7], and 2.2 ± 0.4 SNU are observed [8]. Here a SNU is the solar neutrino unit, which is equal to 10^{-36} $^{37}Cl + \nu \rightarrow ^{37}Ar$ transformation events per second on the earth.

The accumulation of observational results for 10 years has given a positive result. Although there are fewer neutrinos than expected by several times, they are undoubtedly being recorded with a noticeable excess of the effect above the background. It is true that the accuracy of the measurements is still always low, and this is not surprising when the average rate of formation of ^{37}Ar in the detector does not exceed one atom every 2 days. Nevertheless, an attempt has been made [9] to analyze the seasonal behavior of Davis' results. It turned out that from May to August, when the earth is farther from the sun, the number of detector counts is less by 1.1 ± 0.6 SNU than during the winter months. If this difference is real and if the cause is the transformation of neutrinos from one kind to another (proposed by Pontecorvo), then the difference in the neutrino masses $\Delta m^2 = 4 \cdot 10^{-10}$ eV^2.

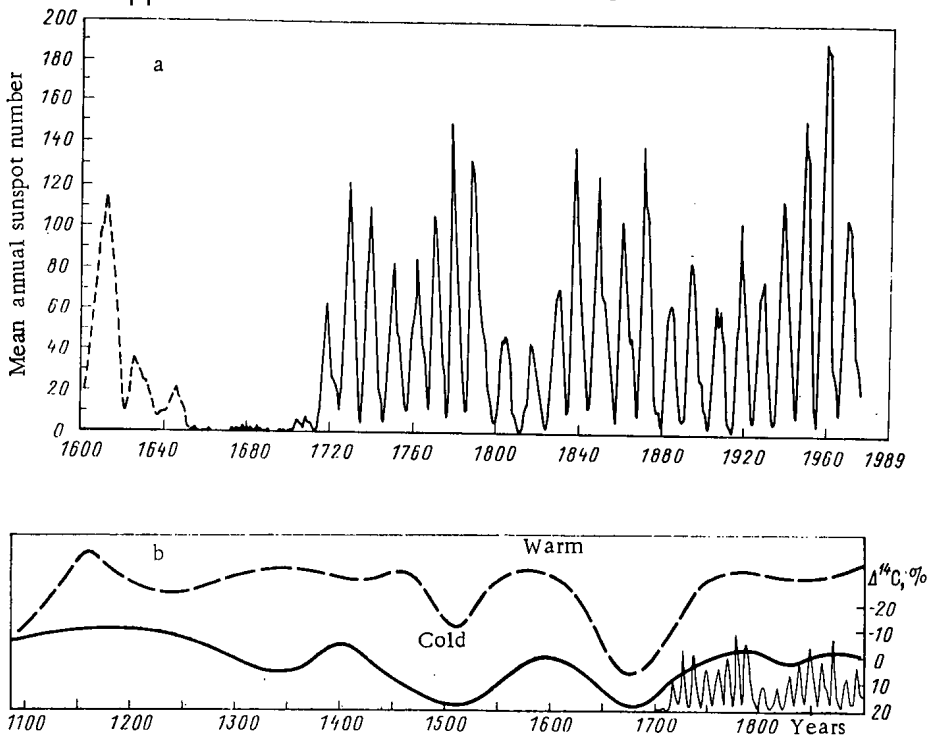

Fig. 1. a) Results of observations of solar activity for 400 years and b) the ^{14}C content in the annual rings of trees since the year 1100 (——) and variations of the terrestrial climate (---).

First of all, it follows from the observations that the temperature at the center of the sun is lower than was assumed. The yield of ^{8}B is proportional to a very high (>13) power of the temperature, therefore, a chlorine detector is similar to a sensitive thermometer for measuring the central temperature of the sun. In the first attempts to explain the neutrino deficit people were seeking a way to bring the solar model into agreement with a reduced central temperature.

First of all, the opacity of the interior material was subjected to careful calculations [10]. The flux of energy from the center to the outer layers of the sun is transported primarily by photons, which diffuse through the matter of the interior. The greater the average mean free path of a photon is, the more rapidly the diffusion proceeds and the smaller is the required temperature gradient. Consequently, a decrease of the opacity (an increase of the average mean free path of a photon) leads to a flatter temperature run, i.e., a decrease in the central temperature. The opacity depends strongly on the amount of heavy elements (heavier than helium), since the absorption of photons occurs most strongly by bound electrons (the photoelectric effect). The composition of solar matter is characterized by its content of hydrogen (X), helium (Y), and the remaining elements (Z): $X + Y + Z = 1$. Spectral analysis of the upper layers of the sun gives [11] the following values $X = 0.78$, $Y = 0.20$, and $Z = 0.02$. But even at the surface of the sun Z is not determined very reliably, and this value is taken to lie within the limits from 0.01 to 0.04 in various model calculations. If the composition of the material at the center differs from the surface only in the values of X and Y due to hydrogen burning but Z is the same, the calculations of the opacity do not yield the necessary reduction of central temperature. Then ideas are advanced to the effect that Z is less at the center than at the surface and there were less heavy elements during formation of the sun but they have then been captured at the surface from the interplanetary material or upon passage through the interstellar medium [12].

Hypotheses have been discussed about mixing of material inside the sun with this same purpose. It is assumed in connection with the construction of the standard models that the young sun was uniform in chemical composition, since it passed through a stage of strong mixing by convective motions in the process of formation. Mixing in the present sun is assumed only near the surface to a depth $\approx 0.2R_{\odot}$, but all the rest of the interior preserves its initial composition, and only near the center does hydrogen burn and helium get formed. Ap-

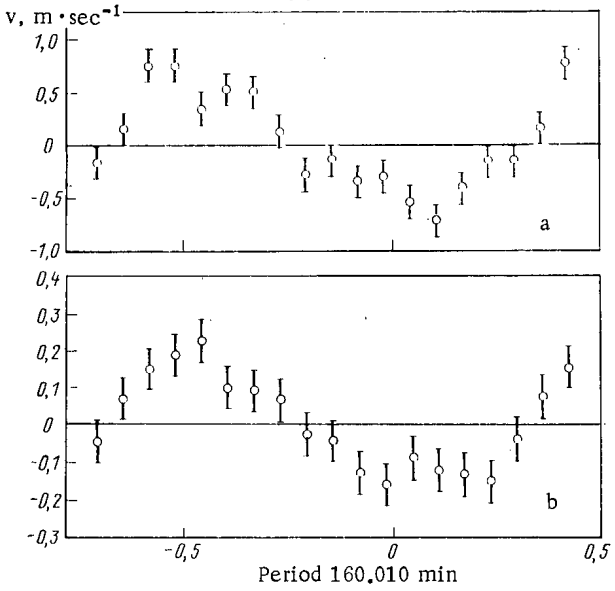

Fig. 2. Oscillations of the central region of the surface of the sun from observations (a) at Crimea in 1974-1978 and (b) at Stanford in 1976-1978. The period is 160.010 min.

preciable change in X (a decrease) and Y (an increase) start only at a radius $<0.2R_o$, and at the center X ≈ 0.35 and Y ≈ 0.63. One of the causes of the mixing could be centrifugal forces due to rapid rotation. But the observations have not confirmed the hypothesis of rapid rotation of the internal layers, and for this reason mixing is improbable.

Nonsteady mixing [13] has been proposed in the hypothesis of Fowler concerning a variable burning rate of nuclei at the center of the sun. Sudden discontinuous mixing events enrich the central region in ^{3}He nuclei, whose burning occurs without the emission of neutrinos. The relative yield of the main reaction $^3He + {}^3He \rightarrow {}^4He + 2p$ is increased, but the ^{8}B nuclei become fewer. In the outer layers of the sun this type of nonsteadiness cannot occur if their period is much less than the diffusion time for energy from the center to the surface ($\sim 10^7$ years), and rapid variations are smoothed out. In general, the hypotheses of nonsteady processes in the sun can be treated as a completely regular stage of approximation to the true physics of the sun, in which models of quiet continuous burning would be only the first approximation. The internal transients suggested by Fowler are probably one of many possibilities which are in store for further investigators to find. If extensive motions of the internal layers are observed in such a semisolid celestial body as the earth, then their absence in the hot interior of the sun is improbable.

Observed Temporal Variations. The new evidence for nonsteadiness observed in recent years is of great interest. Some astrophysicists are attempting to explain ice ages which have occurred on earth in the past by long-period secular variations of the luminosity of the sun. There is direct evidence of secular variations of solar activity. The so-called Maunder minimum observed from 1645 to 1715 is well known [14] (Fig. 1). Not a single spot was noticed on the sun for 70 years. This minimum has been confirmed by the ^{14}C observations and the D/H isotopic ratio in the annual rings of trees. Besides the Maunder minimum earlier secular oscillations are visible. It is evident that the 22-yr (2·11 years) cycles of solar activity are modulated by some kind of slower processes. No explanations have been found yet for these modulations. Possibly their causes are produced at a greater depth.

The results of processing of solar observations for the last 80 years have recently been published [15]. It has been detected that the horizontal diameter of the sun is monotonically decreasing (2 arc seconds per century). Evidence has been found in historical archives of the fact that 400 years ago the radius of the sun was greater than its contemporary value. It is possible that contraction has been continuing for several centuries. But the contraction rate is too large and cannot be monotonic for a long time. Possibly a contraction phase is periodically replaced by an expansion phase. It is true that a similar analysis of the vertical diameter gives an appreciably slower contraction (0.2 sec per century). These results will probably be subjected to verification in the near future.

A very interesting oscillation with a period of 160.010 ± 0.004 min has been discovered at the Crimean Observatory by Severnyi and his co-workers [16]. They have found (Fig. 2) that the central part of the solar disk with a radius of one-half the solar radius moves periodically

towards the observer and away from him with a velocity of 2 m/sec and a displacement amplitude of ∿10 km. The observations have already been carried out for four years, and the oscillation is maintained with a stable and now well-determined period. The large size of the circle observed indicates that the oscillation covers the enormous surface of the sun and can evidently be considered to be global. But the oscillation period is too large for the most probable global oscillations. Their periods do not exceed one hour according to calculations [17]. The interpretation of oscillations with a period of 160 min already requires a revision of the solar models [17].

A rather complicated spectrum of oscillations with a period less than 1 h has been detected in the observations of Hill [18]. In 1973 Dicke and Goldenberg [19] published observations which indicated an oblateness of the sun. Oblateness was not confirmed in the experiments of Hill et al. set up to check the earlier result, but oscillations of the solar surface with periods of about 50, 30, 22, etc. to 7 min were detected. The short-period oscillations of the sun whose observations started quite recently have already opened up a new area of solar physics similar to terrestrial seismology. The seismometry of solar oscillations will probably permit "peering into" the depths of the sun similarly to what has been done on the earth. Undoubtedly much attention will be devoted to this area of science in the near future.

There are reasons to expect that elastic oscillations propagating from the center to the surface can transport energy. The sound velocity, at which elastic oscillations are propagated, is greater by many orders of magnitude than the rate of photon diffusion. The passage time of sound is about one hour, and the photon diffusion time is $\sim 10^7$ years. Even negligible damping of a wave generated at the center can have a significant effect on the mechanism of energy tranport from the center to the surface and introduce very important changes in the solar model.

Conclusion. The observations of Davis and the neutrino deficit discovered by him indicate that fewer ^8B nuclei are formed at the center of the sun, and consequently the temperature is lower than was assumed. But the principal source of the energy — the main branch of the hydrogen cycle of reactions — cannot be recorded by the chlorine detector of Davis; therefore there is no reason to doubt the thermonuclear burning of hydrogen in the sun. The energy of gravitational contraction is the only competition to thermonuclear energy in the evolution of the stars. But there is no real possibility of including this powerful source in the present sun.

For the sake of completeness, one should mention one more conceivable source — the annihilation of antimatter with the matter of the sun. The heating power of this source is higher still than for gravitational sources [20], but the problem of supplying the sun with antimatter requires no less an ingenious fantasy than does the inclusion of black holes.

Undoubtedly, the observation of solar neutrinos with lower-threshold detectors and with better statistics is very desirable. The next one after chlorine will evidently be gallium (^{71}Ga). The threshold for the reaction $^{71}Ga(\mu, e)^{71}Ge$ is equal to 0.236 MeV in all. It is lower than the limit of the neutrino spectrum of $2p \rightarrow d + \nu$, which is equal to 0.420 MeV. This detector is being prepared in the USA and at the Baksansk Neutrino Laboratory in the USSR. Several more possible detectors have been proposed. Their physical properties have been thoroughly analyzed by Bahcall [21]. Perhaps the most interesting detector is the one made out of ^{115}In. In a reaction with it, the threshold of which is equal to 0.120 MeV in all, a neutrino is converted into an electron, and its energy is uniquely related to the neutrino energy; therefore, one can determine the neutrino spectrum and evaluate the relative role of the various branches of the reactions of the hydrogen cycle by measuring the spectrum of the electrons.

Notwithstanding the complexity of the methods of neutrino astronomy, its development is exceedingly desirable, and in the near future it will undoubtedly be intensified. The problems facing us are too important. The most probable reason for the present discrepancy of the predictions of the solar models with the neutrino observations appear to us to be nonsteady phenomena at the center of the sun. They can cause either temporary decrease in the neutrino luminosity or a reduction of the average temperature of the center as a consequence of the mixing of material or due to the participation of elastic waves in the transport of energy. Future analysis of phenomena of this type will probably eliminate the disagreements between calculations and observations.

LITERATURE CITED

1. R. Davis et al., Phys. Rev. Lett., 20, 205 (1968); in: C. L. Cowan Mem. Symp., N. Y. (1979), p. 17.
2. Ya. B. Zel'dovich and I. D. Novikov, Gravitational Theory and the Evolution of Stars [in Russian], Nauka, Moscow (1971).
3. R. Stothers and R. Ezer, Astrophys. Lett., 13, 45 (1973); D. D. Clayton et al., Bull. Am. Astron. Soc., 7, 242 (1975).
4. N. A. Vlasov, At. Energ., 39, No. 2, 103 (1975).
5. J. Bahcall and R. Sears, Ann. Rev. Astron. Astrophys., 10, 25 (1972).
6. J. Bahcall and R. Davis, Science, 191, 264 (1976).
7. J. Bahcall, Astrophys. J., 184, 1 (1973).
8. R. Davis, in: Proc. Purdue Univ. Conf. (1978), p. 53; Sci. News, 115, 103 (1979).
9. E. Robert, in: C. L. Cowan Mem. Symp., N. Y. (1979).
10. J. Bahcall et al., Astrophys. J., 156, 559 (1969).
11. E. Gibson, The Quiet Sun [Russian translation], Mir, Moscow (1977). Originally published as NASA SP-303, USGPO, Washington, D.C. (1973).
12. P. Joss, Astrophys. J., 191, 774 (1974).
13. W. Fowler, Nature, 238, 24 (1972); R. Rood, Nature Phys. Sci., 240, 178 (1972).
14. K. Frazier, Sci. News, 109, 154 (1976); J. Eddy, Science, 192, 1189 (1976).
15. J. Eddy and A. Boornazian, Sci. News, 115, 420 (1979). R. Dicker, Nature, 276, 676 (1978).
16. A. Severnyi (Severny) et al., Nature, 259, 87 (1976); A. B. Severnyi, Astron. Zh., 56, 1137 (1979).
17. V. N. Zharkov and S. V. Vorontsov, Usp. Fiz. Nauk, 128, 731 (1979); Stron. Zh., 55, 84 (1978).
18. H. Hill et al., Observatory, 96, 130 (1976); Astrophys. J., 213, L81 (1977).
19. R. Dicke and H. Goldenberg, Astrophys. J. Suppl., 27, 131 (1974).
20. N. A. Vlasov, At. Energ., 44, No. 1, 45 (1978).
21. J. Bahcall, Rev. Mod. Phys., 50, 881 (1978).

LOOP INSTALLATION WITH ORGANIC COOLANT FOR MIR REACTOR

V. A. Tsykanov, P. G. Aver'yanov, V. P. Anisimov, Yu. A. Kabanov, E. P. Klochkov, V. A. Kuprienko, A. S. Kusovnikov, L. N. Rozhdestvenskaya, Yu. G. Simonov, and V. V. Sidorov

UDC 621.039.553

There has been a sharp awakening of interest in recent years in the question of supplying heat to towns and factories from nuclear energy sources. The advantages and drawbacks of various coolants have been reassessed in connection with the operating parameters of specialized reactors intended for the generation of heat. It has been observed that the use of high-temperture coolants would provide us with the prerequisites for creating the reactors for nuclear district-heating stations.

In this regard, it is of particular importance that there should be an adequate experimental base on which to build solutions to the basic problems that arise when reactors using high-temperature organic coolants are being designed, and particularly during the development of economical and reliable fuel elements [1]. This involves carrying out a large series of reactor tests on prototype fuel elements and coolant systems.

Only one reactor is at present in operation using high-temperature organic coolant, the ARBUS [2], and this tends to limit the opportunities for testing new types of fuel elements. The reactor does not have a biological shield on its primary coolant circuit, so that we are unable to test unsealed fuel elements.

We, therefore, needed to build a large loop installation with a power of several hundred kilowatts so that we could carry out such investigations. The organic coolant loop was created on the basis of the equipment and boxes belonging to the sodium loop of a MIR reac-

Translated from Atomnaya Énergiya, Vol. 49, No. 3, pp. 161-163, September, 1980. Original submitted January 25, 1980.

 0038-531X/80/4903-0610$07.50

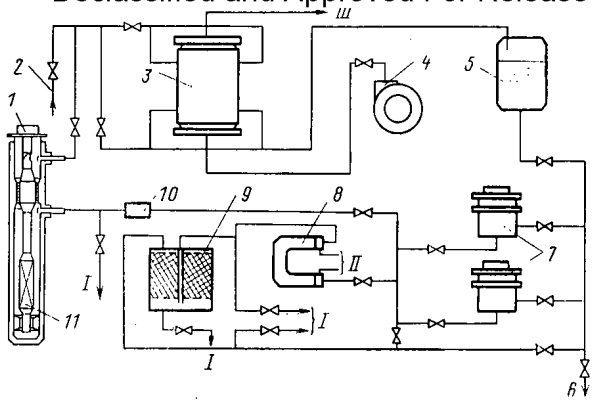

Fig. 1. Schematic of PO-1 loop: 1) loop channel; 2) DTM inlet from distillation plant; 3) heat exchanger; 4) air circuit; 5) compensation tank; 6) DTM discharge line to distillation cleaning plant; 7) pumps; 8) heat-exchanger for filter; 9) filter; 10) mechanical cleaning filter; 11) test assembly; I) sample; II) water; III) atmosphere.

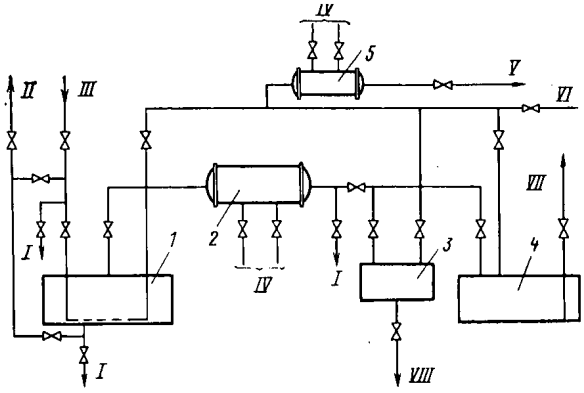

Fig. 2. Schematic of equipment for distillation cleaning of DTM: 1) tank for gradual heating and evaporation of used coolant; 2) condenser; 3) receiver tank for volatile products of dissociation; 4) receiver tank for clean DTM; 5) steam trap at inlet to vacuum-forming system; I) sample; II) in transport tank; III) from PO-1; IV) water; V) vacuum-forming system; VI) nitrogen; VII) in PO-1; VIII) drainage.

tor [3], which had largely become surplus to requirements in view of the introduction of a method of testing materials and fuel elements for high-speed reactors in the BOR-60 [4]. This design enabled us quickly and cheaply to create good experimental conditions for the necessary reactor tests in the program for the development of reactors with a high-temperature organic coolant.

Design and Parameters of the Loop. The scheme of the PO-1 loop (Fig. 1) is two-circuit in concept: the coolant for the primary circuit being ditolylmethane (DTM), while that of the secondary circuit is air. The loop has a vacuum system, a firefighting system, a system for monitoring the sealing of the fuel elements, electrical heating of the coolant circuits, a sampling system, and a system for the distillation cleaning of the DTM. This last system (Fig. 2) incorporates a tank for the gradual heating and evaporation of the used coolant, for collecting the clean DTM and the volatile products of dissociation, and also the necessary pipes and fittings.

The volatile products of dissociation of the coolant are removed from the evaporator tank after distillation in a transport tank or in a long-storage tank. The basic parameters of the loop are as follows: thermal power, up to 400 kW; flow rate of DTM through the channels, 15-25 m^3/h; temperature of DTM at inlet to channel, 453-483°K; pressure of coolant in channel, $(4-10)\cdot10^5$ Pa; density of thermal neutron flux in channel, 10^{14} neutrons/$cm^2\cdot$sec.

Technical Characteristics of Equipment. The channel of the PO-1 loop is made from a type of Field channel with an experimental volume of 4.3 liters. To reduce the heat losses from the channel to the water in the reactor basin, the channel is equipped with a gas-insulating cavity. Up to 10 transducers can be introduced for monitoring the irradiation conditions. The loop circuit is equipped with the packless hermetic pump used in the water circuits of the reactor. These pumps produce a pressure difference of $8.5\cdot10^5$ Pa at a delivery rate of 30 m^3/h when pumping DTM. The total volume of the condenser in the PO-1 loop is 1.15 m^3, while the area of free surface of the coolant is 0.6 m^2.

A mechanical full-flow filter is installed ahead of the DTM channel inlet, and takes the form of a tube, the inside of which carries a filter element in the form of a metal grid. The capacity of the DTM distillation cleaning tanks is chosen on the basis of complete emptying of the circuit. The heat exchanger, tank, filters (used for additional mechanical cleaning), the system of pipes, the fitting, the secondary circuit, and the auxiliary system were all already present in the sodium loop, and after cleaning and the appropriate preparation, these were ready for use in the newly created installation.

Purpose of the Loop. Various reactor experiments were carried out on the new loop. These were concerned with the development of new fuel elements, including life and various short-term tests, and particularly tests on the hermetic sealing of the can.

The wide investigation of coolant technology is envisaged, including the influence of the quality and composition of various additives and the products of radiation and thermal dissociation of the coolant on the behavior of materials under irradiation and on the formation of surface deposits on the heat-transmission surfaces. It is also proposed to investigate the relative effectiveness of various methods of cleaning the coolant, including cleaning from radioactive contamination. In combination with the work carried out on the ARBUS reactor, these investigations enable us to obtain the experimental results necessary to provide a basis for our design work.

After the commissioning work has been completed, the PO-1 loop was brought into operation in August 1978. The results it has achieved show that the technical characteristics of the loop are in full accord with its design characteristics.

LITERATURE CITED

1. V. A. Tsykanov et al., in: Collection of Papers from the Seminar on the Future Possibilities of Employing Nuclear Reactors to Supply Heat to Towns and Factories [in Russian], Dimitrovgard (1978), p. 45.
2. Yu. N. Aleksenko et al., in: Collection of Papers from the Seminar on the Future Possibilities of Employing Nuclear Reactors to Supply Heat to Towns and Factories [in Russian], Dimitrovgrad (1978), p. 24.
3. P. G. Aver'yanov et al., Preprint NIIAR P-121, Melekess (1971).
4. O. D. Kazachkovskii et al., At. Énerg., 38, No. 3, 131 (1975).

CALCULATION OF HYDRAULIC RESISTANCE OF CLUSTERS OF RODS WITH HEAT-EXCHANGE LATTICE-INTENSIFIERS

V. K. Ivanov and L. L. Kobzar'

UDC 536.242

Experimental studies on the hydraulic characteristics of full-scale models of fuel assemblies (FA) were conducted at the Kurchatov Institute of Atomic Energy with various types of heat-exchange lattice-intensifiers. The aim of the experiments was to find an optimal type of intensifier which would ensure a significant increase in the power of FA while the increase in the hydraulic resistance is within acceptable limits, the technological effectiveness is good, the design is reliable, and there is only a slight additional injection of metal [1].

In the present paper we analyze the experimental data. We consider the possibility of calculating the hydraulic resistance of the channel of an RBMK-type reactor by techniques used for clusters with ordinary spacing lattices and the possibility of calculating the coefficient of hydraulic resistance of lattice-intensifiers on the basis of their geometric characteristics. The technique of [2] was used. A description of the experimental equipment and the experimental data on the hydraulic resistance of the models studied are given in [1].

Various types of lattice-intensifiers were studied on full-scale models of FA, consisting of 18 tubes 1.35 cm in diameter and a central unheated rod of diameter 1.5 cm (Fig. 1). The upper part of the models (heated length 7 m) contained lattice-intensifiers while the lower part was provided with regular spacing lattices of the RBMK-1000 reactor The models were installed in a channel of diameter 8 cm.

Six types of lattice-intensifiers were studied. Apart from the first, these types were based on the regular spacing lattice of the RBMK-1000 (see Fig. 1). The lattice-intensifiers of the first type, differing substantially from the others, consist of joined segments of twisted strips which occupy the entire space around the fuel elements [3]. The distance between the lattices is 20.6 cm.

Translated from Atomnaya Énergiya, Vol. 49, No. 3, pp. 163-165, September, 1980. Original article submitted August 6, 1979.

 0038-531X/80/4903-0612$07.50

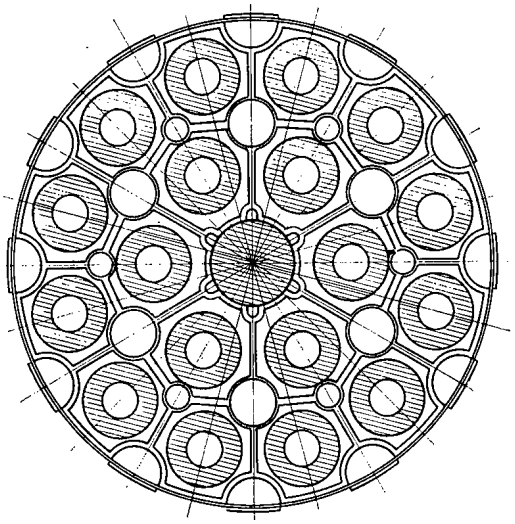

Fig. 1. Cross section of model of FA of RBMK-1000 reactor.

Lattices of the second type have on their outer rim and on their inner elements tabs formed by local cutting and bending. Two forms of such lattices are possible: with spacing of either all the fuel elements (complete lattice) or only six fuel elements (incomplete lattice). The distance between complete lattices is 36 cm while two incomplete lattices placed between them are separated by a distance of 12 cm from each other. In lattices of the third type all of the features of the second type are repeated but the bends on the rim and the inner elements are replaced by stamped lugs.

In lattices of the fourth and fifth types we used the outer rim of lattices of the third type and Archimedean screws were installed in the place of lattices corresponding to square cells of the cluster. The angle of the twist of the screws in these lattices is 3.14 and 2.705 rad, respectively. The distance between lattices is 18 cm. The model with lattices of the sixth type is analogous to the model with lattices of the third type except that only one incomplete lattice is set up between two complete lattices 36 cm apart.

The experiments were conducted with a pressure of 6-8.5 MPa at the channel outlet, a mass velocity of 1000-4000 kg/m^2·sec, a heat-release power of up to 6 MW, a thermal-flux density of up to 1.2 MW/m^2, and a relative enthalpy of up to 0.8 at the channel outlet. The pressure distribution over the length of the channel was measured under three modes of heat release: crisis-free, under crisis conditions, and in the transcritical mode. critical mode.

For cases without boiling of the water in the channel we determined the coefficients of hydraulic resistance for the different types of lattice-intensifiers. The pressure drop across the lattices was found as the difference between the total hydraulic losses and the calculated losses for friction in the smooth cluster. In cases when not all lattices of the given type were identical (types 2, 3, and 6) the hydraulic resistance coefficient was calculated for an assembly comprising one complete and one or two incomplete lattices.

It is seen from Fig. 2 that in any large range of Reynolds number ($25{,}600 < Re < 339{,}900$) the hydraulic resistance coefficients of the regular spacing lattice of the RBMK-1000 and lattice-intensifiers of all types do not depend on the Reynolds number. Using the hydraulic resistance coefficient found experimentally, we calculated the total pressure drops over the length of the models studied for all modes. The whole set of data was divided into several ranges of equilibrium mass steam content at the channel outlet (Table 1). It follows from Table 1 that the arithmetic mean error is no greater than 7%. These results substantiate the possibility of using (and improving) the technique presented in [2] for design calculations of the hydraulic characteristics of FA with heat-exchange intensifiers.

In the calculations described above we used the hydraulic resistance coefficients of spacing lattice-intensifiers, obtained from experimental data. Clearly, in choosing the optimal type of such lattices in design developments it is not always possible to find the necessary experimental data. It would, therefore, be handy to have a reliable method for calculating the resistance coefficient of a lattice from its geometric characteristics.

One such technique has been presented in [4]. In this technique the pressure drop in the spacing lattice during the flow of a single-phase liquid is described by

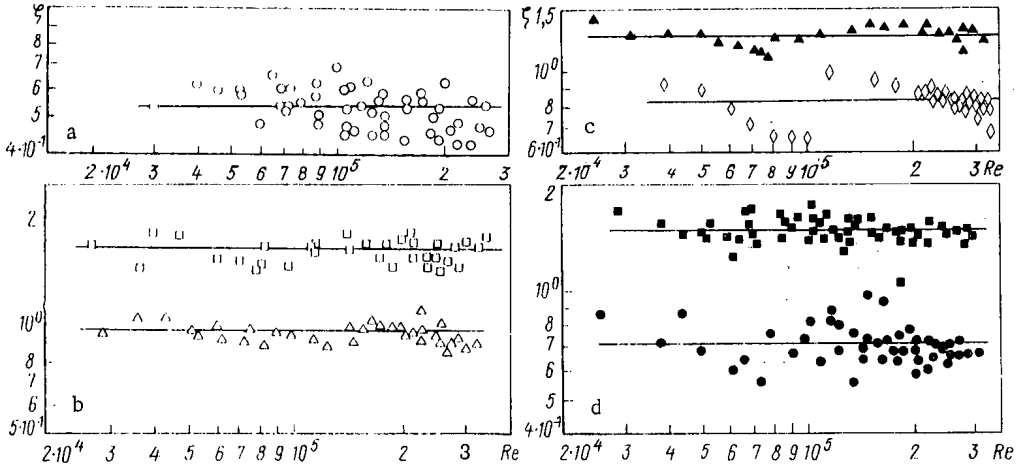

Fig. 2. Hydraulic resistance coefficient as function of Reynolds number for a) regular spacing lattice of RBMK-1000 and b, c, d) lattice-intensifiers of three types: ——) mean value; ○) lattice of RBMK-1000; □, △, ■, ●, ◇, ▲) lattice types 1-6, respectively.

$$\Delta P = C_{\text{B}} \frac{\rho W^2}{2}. \tag{1}$$

Here C_B is the hydraulic resistance coefficient of the spacing lattice,

$$C_{\text{B}} = C_V K^2, \tag{2}$$

where C_V is the modified loss coefficient; $K = F_V/F_B$, coefficient of relative narrowness of the channel cross section; F_V, lattice cross section; and F_B, total cross section of the channel.

In [4] $C_V = 6\text{-}7$ for $Re > 5 \cdot 10^4$.

For the available experimental data we solved the inverse problem: from the experimental values of the hydraulic resistance coefficients of the lattice-intensifiers we found C_V (Table 2). In this case, in accordance with the recommendations of [4] we assume that F_V is the area of all the lattice elements in the plan.

It follows from Table 2 that C_V, which Klaus [4] assumes to be constant, varies between quite wide limits. Only the value of C_V for the regular RBMK-1000 lattice lies within the range he recommends. Thus, it can be said that the technique of [4] is not applicable to the types of lattice-intensifiers studied.

A deficiency of the technique considered is that it takes no account of the slope of the lattice elements to the direction of the incoming flow. This can be taken into account as follows:

$$F_V = \int_F f(\gamma)\, dF, \tag{3}$$

where F is the area of the lattice elements in the plan (midsection) and $f(\gamma)$ is a function of the slope of the elementary area to the direction of the incoming flow (angle of attack).

The form of the function $f(\gamma)$ is determined in [5] on the basis of experimental data on the hydraulic resistance of tubes with a regular roughness which is formed by projections of regular shape, uniformly distributed over the surface:

$$f(\gamma) = \begin{cases} \sin^2 2\gamma & \text{for} \quad 0 \leqslant \gamma < \pi/4; \\ 1 & \text{for} \quad \pi/4 \leqslant \gamma \leqslant \pi/2. \end{cases}$$

Suppose that in this form function $f(\gamma)$ also correctly reflects the influence of the angle of attack for elements which are in the core of the flow and not on the wall.

In the calculation of F_V from Eqs. (3) and (4) we once again found the values of C_V for all types of lattice. The results of the calculation (see Table 2) have a small scatter.

TABLE 1. Dependence of Arithmetic Mean Error on Mass Steam Content

x	$\bar{\Delta}$, %
—0,704— —0,520	—2,93
—0,520— —0,319	—2,59
—0,319— —0,119	—3,35
—0,119—0,080	—1,35
0,080—0,300	2,69
0,300—0,500	7,00
0,500—0,700	6,03
0,700—0,882	5,92

TABLE 2. Comparison of Calculated Values of Hydraulic Resistance Coefficients of Lattice-Intensifiers with Experimental Data

Lattice type	ζ_e	Calc. of C_V		ζ_c $(C_V-7{,}18)$	$\frac{\zeta_e-\zeta_c}{\zeta_e}\cdot 100\%$
		[4]	present paper		
Regular lattice of RBMK-1000	0,55	7,03	7,03	0,562	—2,18
1	0,96	1,46	6,79	1,02	—6,25
2	1,6	7,26	7,47	1,53	4,4
3	1,47	5,68	7,07	1,49	—1,36
4	0,71	3,24	7,04	0,72	—1,41
5	0,81	3,77	7,47	0,77	4,9
6	1,25	6,06	7,40	1,21	3,2

The arithmetic mean value of C_V, equal to 7.180, was adopted for further calculations. The calculations of the hydraulic resistance coefficients of the lattices, obtained with this value of C_V, are given in Table 2. The maximum relative error of the calculation is 6.25%.

The study of the hydraulic resistance characteristics of full-scale models of FA of RBMK-type reactors permits the following conclusions to be drawn:

the technique of the hydraulic calculation of FA cooled with boiling water [2] describes the experimental data with good accuracy;

the technique of calculation of the hydraulic resistance coefficient of lattice-intensifiers from the geometric characteristics (present paper) describes the experimental data with an error not exceeding 6.25%. It can thus be recommended for use in the development of new types of lattice-intensifiers.

LITERATURE CITED

1. V. Aden et al., in: Sixth Int. Heat Transfer Conf., Toronto, August 7-11 (1978), Vol. 5, p. 41.
2. V. S. Osmachkin and V. D. Borisov, Preprint IAÉ-1957, Moscow (1970).
3. V. N. Smolin et al., in: Problems of Atomic Science and Engineering. "Reactor Construction" Series [in Russian], No. 1(12), Izd. TsNIIatominform, Moscow (1976), p. 15.
4. R. Klaus, Nucl. Technol., 17, 15 (1973).
5. L. L. Kobzar', Preprint FÉI-418, Obninsk (1973).

ELECTRON SPECTROSCOPY OF OXIDATION OF STEELS IN N_2O_4-BASED COOLANT

A. G. Akimov, L. P. Kazanskii, V. S. Zotikov,
P. P. Stanishevskii, V. K. Dubinin,
and V. V. Gladyshev

UDC 541.118:620.193.5

Nitrogen tetroxide and compositions based on it are very promising for use as a dissociating coolant and working substance for nuclear power plants being designed [1, 2]. As is known [2-5], chromium–nickel alloys have a high corrosion resistance in these media and can be used as the principal structural materials for the planned plants. Most papers, however, lack information about the mechanism of oxidation of steels in N_2O_4; in view of this, studies were made of the processes which occur on the surface and in the surface layer of chromium–nickel steels in interaction with N_2O_4.

The use of electron spectroscopy for chemical analysis (ESCA) [6] made it possible to study extremely thin oxide films and, therefore, the exposure chosen for specimens in N_2O_4 was 10 h, especially since a protective coating, which causes the sharpest decrease in the corrosion rate [7], is formed at the very beginning of the exposure. The studies were carried out in the temperature range 200-700°C on specimens of two austenitic chromium–nickel steels, 12Kh18N10T and 09Kh16N15M3B, in the form of polished plates with an area ∿1 cm^2. The electron spectra were obtained in the usual way with an ESCA-3 electron spectrometer made by Vacuum Generators [8].

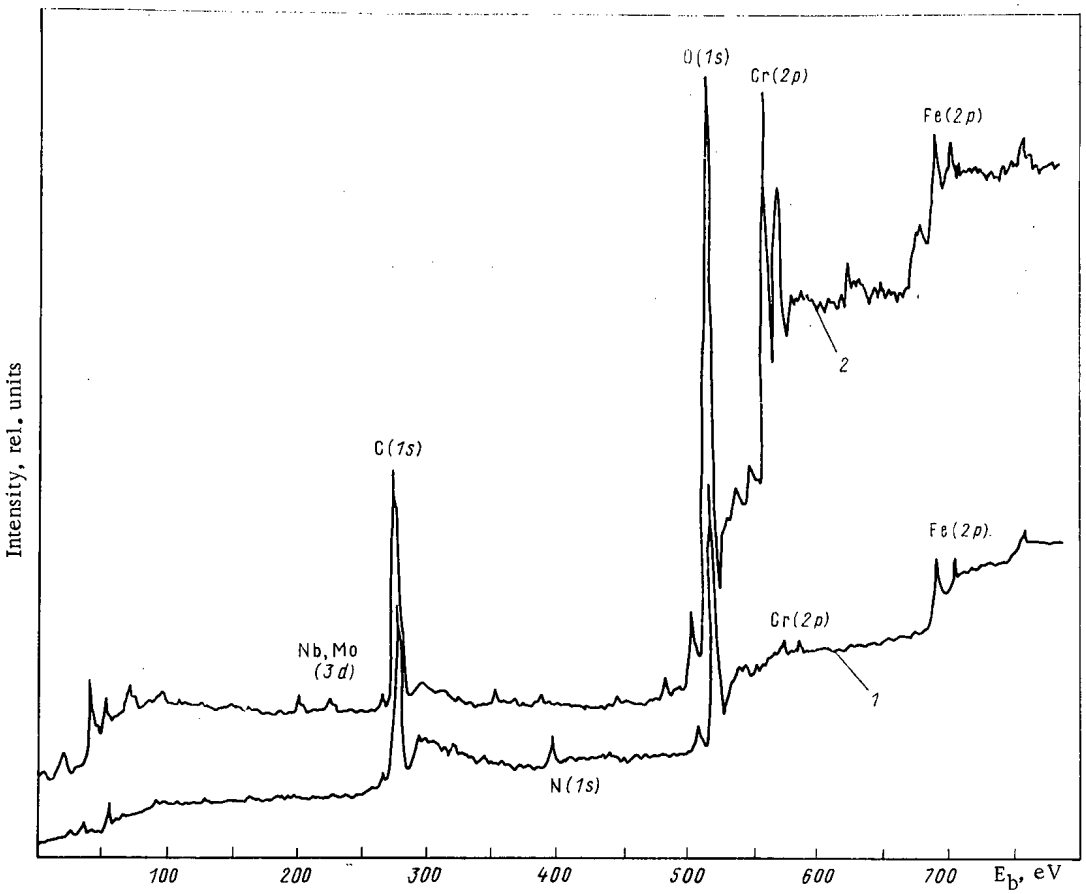

Fig. 1. ECAS spectra of surface of 09Kh16N15M3B steel, obtained at oxidation temperatures of 200°C (1) and 700°C (2).

Translated from Atomnaya Énergiya, Vol. 49, No. 3, pp. 166-169, September, 1980. Original article submitted August 13, 1979.

0038-531X/80/4903-0616$07.50

TABLE 1. Values of E_b of $Fe(2p_{3/2})$ Level at Various Temperatures for Steels 12Kh18N10T and 09Kh16N15M3B

Steel	Temperature, °C					
	200	300	400	500	600	700
12Kh18N10T	711,1	711,1	710,7	711	710,8	711,2
09Kh16N15M3B	711,6	711,2	710,6	710,6	710,8	711,3

To find the distribution of elements and phases in the surface layer we employed layer-by-layer etching of the surface with 4-keV Ar^+ ions in a chamber for the preliminary treatment of the specimens analyzed. The density of the ion current with defocusing of the beam, which was done to achieve uniform etching of the surface, was $2 \cdot 10^{-5}$ A·cm^{-2}, which ensured an etching rate of 300 nm·min^{-1}. The above approximate value of the etching rate was used to estimate the thickness of the etched layer. The quantitative processing of the ESCA spectra and the determination of the atomic concentration of elements were carried out with a PDP-8E microcomputer according to standard programs.

As follows from analysis of the ESCA spectra of the surface of steel specimens exposed to N_2O_4 (Fig. 1) after oxidation at 700°C the N(1s) line of nitrogen, characteristic of specimens oxidized at 200°C, is missing. The ratio of the intensity of the $Fe(2p_{3/2})$ and $Cr(2p_{3/2})$ lines is much smaller than 1 and is roughly equal to 1 in the case of oxidation at 200 and 700°C, respectively. Features common to the spectra of both steels are the absence of lines corresponding to nickel (although the concentration of nickel and chromium in the original alloys was practically the same) as well as the surface of segregations of niobium and molybdenum.

ESCA spectra similar to those given in Fig. 1 allow a qualitative and quantitative analysis to be made of elements without account for their degree of oxidation. To ascertain the degree (or degrees) of oxidation we used the ESCA spectra of the most intense lines of each element, obtained in a narrow range of electron binding energies E_b with a high resolution ($\sim$1.5 eV).

Analysis of the high-resolution ESCA spectra revealed that the N(1s) line as a function of the temperature can be represented with one or two peaks characterizing E_b = 399.6 ± 0.2 and 407.3 ± 0.2 eV, respectively. The maximum intensity of the N(1s) peak with E_b = 407 eV is observed after oxidation at 200°C. After oxidation at 300°C the intensity of this peak is reduced by a factor of three or four while after oxidation at a temperature above 400°C only the peak with E_b = 399.6 ± 0.2 eV is observed. The ratio of the intensities of the N(1s) and $Fe(2p_{3/2})$ peaks does not exceed 0.1, which, when account is taken of the ionization cross sections σ of the respective electronic levels, gives an atomic ratio of N/Fe $\leqslant$ 0.3. It was found that the peak of the N(1s) line with E_b = 407 eV corresponds to nitrogen which enters the compound with an oxidation degree of +5; thus, in the temperature range up to 300°C a compound of the nitrate type exists on the surface of both types of steel as a thin surface layer $\sim$2 nm thick. Raising the temperature to 400°C results in the thermal decomposition and partial desorption of the compounds, as indicated by the decrease in the intensity of the N(1s) peak. The value $E_b \approx 399.6$ eV shows that the most probable degree of oxidation of nitrogen in this case is +1 [9]. Therefore, when the temperature is raised to 400°C the following reaction can occur:

$$NO_3^- \rightarrow NO_{sorp} \rightarrow N_2O. \quad (1)$$

This is confirmed by a reduction in the intensity of the N(1s) peak, which can be interpreted as the following reaction occurring:

$$N_2O_{sorp} \rightarrow N_2 + O. \quad (2)$$

The value of E_b of the $Cr(2p_{3/2})$ line is 576.5 ± 0.1 eV and indicates that in the entire temperature range studied chromium has an oxidation degree of +3, i.e., is present in the form of the oxide Cr_2O_3 [10, 11]. The variation of E_b for the $Fe(2p_{3/2})$ level as a function of the temperature (see Table 1) indicates that the iron oxides Fe_3O_4 and Fe_2O_3 may exist on the surface of the specimens.

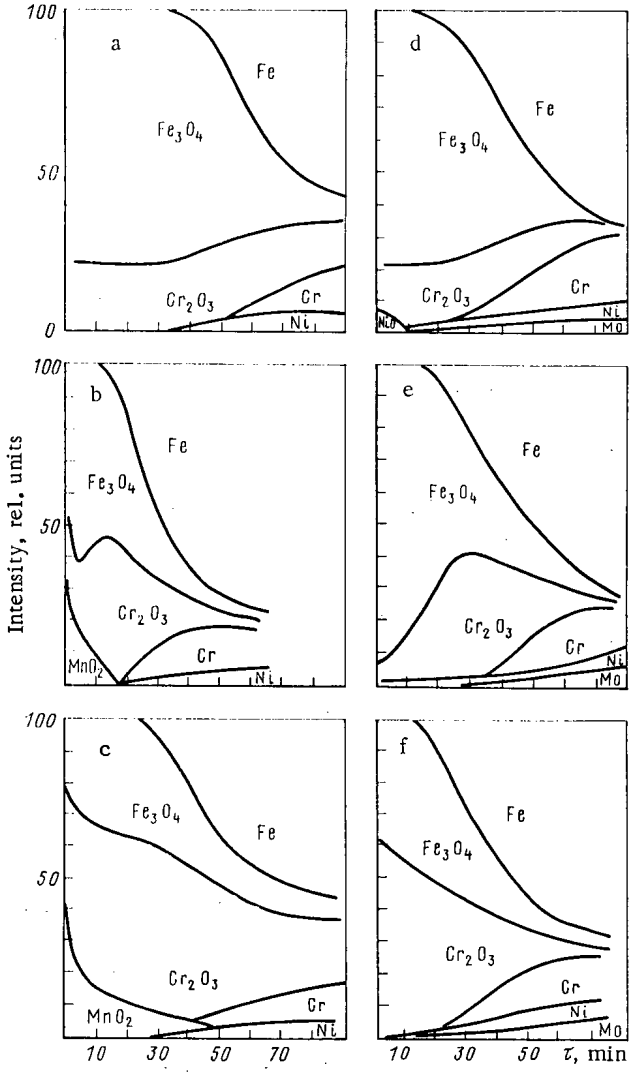

Fig. 2. Distribution curves of elements and phases in films on steels 12Kh18N10T (a-c) and 09Kh16N15M3B (d-f).

As is known [8, 10, 12], the values of E_b for electrons of the Fe($2p_{3/2}$) level, equal to 710.6 and 711.2 eV, correspond to the iron oxides Fe_2O_4 and Fe_2O_3. It may be that the observed decrease in E_b during oxidation in the temperature range from 300 to 700°C is due to reactions of type (1) of the reduction of complex iron oxonitrates; then the value of E_b obtained after oxidation at 700°C reflects the oxidation of Fe_3O_4 and Fe_2O_3. However, this should be confirmed by further investigations.

Figure 2 gives the curves of the distribution of elements and phases in the surface layer of chromium–nickel steels of both types, oxidized under the conditions described above at a temperature of 300°C (a, d), 50°C (b, e), and 700°C (c, f). These curves were obtained by layer-by-layer etching of the surface of the specimens with an Ar^+ ion beam. The sum of the phases was taken to be 100% and is represented as a function of the etching time. In constructing the diagrams corresponding to the phase distribution curves, we took account of not only the integrated intensities of the lines considered but also the ionization cross sections of these lines [13]. It follows from Fig. 2 that the distribution of the main alloying elements and the oxygen-containing phases for both steels are practically identical for one and the same exposure temperature. The nickel concentration in the oxide film is negligible and increases only in the layer adjoining the metal. And the nickel is not bound to the oxygen but is in the metallic state (the oxidation degree is equal to zero), as indicated by the E_b of electrons on the Ni($2p_{3/2}$) level, which is equal to 852.6 ± 0.1 eV [14]. The distribution of elements and phases over the depth confirmed that nitrogen is concentrated in one form or other only in the thick surface layer. Etching off 200-300 nm of this layer leads to the total disappearance of the N(1s) peak. Regardless of the oxidation temperature, the main part of the iron oxides, apart from a thin surface film with a thickness ∿200 nm, which may have the composition Fe_2O_3, has the composition Fe_3O_4, as shown by the value of E_b of the electrons of the Fe($2p_{3/2}$), not exceeding 710.6 eV. As the oxide–metal interface is approached E_b becomes somewhat smaller than the characteristic value of 710.6 eV, which corresponds to

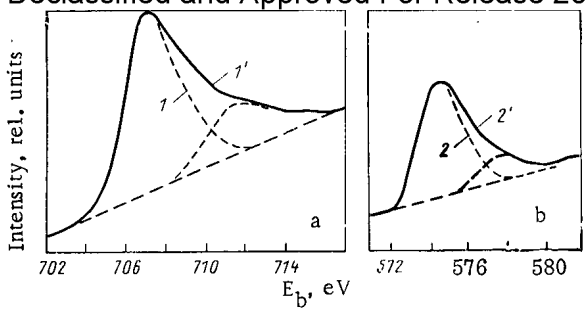

Fig. 3. ECAS spectra of electrons of a) $Fe(2p_{3/2})$ and b) $Cr(2p_{3/2})$ lines.

stoichiometric Fe_3O_4 [8]. This may indicate the enrichment of Fe_3O_4 with divalent iron as the result of the reduction of Fe_3O_4 during the ion etching. However, special experiments on the spectrometer with a rotating analyzer, making it possible to obtain the angular dependences of the electron spectra, showed that with a change in the intensity of electron yield there is a change in the E_b of electrons of the $Fe(2p_{3/2})$ level. Accordingly, the reduction in E_b as the metal–oxide interface is approached does indeed indicate an increase in the content of divalent iron in Fe_3O_4. Such an effect is not observed for the oxide Cr_2O_3.

From the data of Fig. 2 it follows that in both steels the distribution of metallic and trivalent chromium is similar and depends significantly on the oxidation temperature. If oxidation at 300°C leads only to an insignificant enrichment of the metal–oxide interface with chromium, then an increase in the temperature to 500°C is accompanied by a now substantial enrichment of the oxide with chromium. The highest chromium content (in the form of Cr_2O_3) is observed roughly in the middle of the oxide film. A further increase in the oxidation temperature to 700°C leads to the surface of the specimen being enriched with chromium oxide. In 09Kh16N15M3B steel the surface layer consists of 75% chromium oxide. This dependence of the chromium distribution in the oxide film on the oxidation temperature can be explained on the basis of the model given in [6], which considers two parallel processes: the topochemical reaction of reduction of the iron oxide with metallic diffusion,

$$3Fe_3O_4 + 8Cr = 4Cr_2O_3 + 9Fe\,, \qquad (3)$$

and chromium diffusion, which depends exponentially on the temperature. Reaction (3) leads to the accumulation of low-mobility Cr_2O_3 molecules in the reaction zone, but as the temperature rises the zone where reaction (3) occurs shifts toward the oxide–gas interface and at some temperature (600-700°C in our case) the reaction zone reaches the surface of the oxide.

An appreciable difference between the chemical composition of the oxide films on the steels of the grades indicated is that at an oxidation temperature above 500°C a considerable quantity of manganese is accumulated on the surface of steel 12Kh18N10T in the form of MnO_2. The binding energy of electrons of the $Mn(2p_{3/2})$ level is 642.2 eV [15]. In this case the atomic content of manganese on the surface surpasses the atomic content of iron, although the volume concentration of manganese in the original alloy is ∿2%. At the same time, no accumulation of other alloying elements which appear in the steels in small quantities (Ti, Nb, Mo) occurs on the surface in the surface layer.

It follows from Fig. 2 that the metal–oxide interface is not planar but rather diffuse-smeared. And in comparison with iron, chromium as a rule is oxidized in thicker layers. These facts taken together warrant the assumption that on the metal surface there is a distribution of more or less reactive segments which will oxidize to various depths. This possibility is indicated by the spectra of electrons of the $Fe(2p_{3/2})$ and $Cr(2p_{3/2})$ lines which are given in Fig. 3. Spectra 1 and 2 correspond to the unoxidized surfaces of iron and chromium, spectra 1' and 2', to the surfaces of steel 09Kh16N15M3B after etching off the oxide film with Ar^+ ions. As follows from comparison of the data, spectra 1' and 2' differ from spectra 1 and 2 by the presence of a smeared "branch" in the region of large values of E_b. This can be explained by the existence of a peak of very low intensity, corresponding to an unoxidized element. Thus, in this case it can be assumed that there exist local segments of the surface, e.g., grain boundaries, which differ as to oxidizability. These effects, however, cannot be studied by photoelectron spectroscopy and require the use of other methods of structural analysis of the component materials.

LITERATURE CITED

1. Atomic Science and Engineering in the USSR [in Russian], Atomizdat, Moscow (1977).

2. V. B. Nesterenko (editor), Physicochemical and Thermophysical Properties of the Chemically Reacting System $N_2O_4 \rightleftarrows 2NO_2 \rightleftarrows 2NO + O_2$ [in Russian], Nauka i Tekhnika, Minsk (1976).
3. A. M. Sukhotin and V. S. Zotikov, Chemical Resistance of Materials [in Russian], Khimiya, Leningrad (1975).
4. A. M. Sukhotin et al., in: Passivity and Corrosion of Metals [in Russian], Izd. GIPKh, Leningrad (1975), p. 37.
5. A. M. Sukhotin, V. S. Votikov, and A. D. Esenina, Inf. Byull. Khim. Prom., No. 3(72), 41 (1978).
6. A. G. Akimov, Zashch. Met., No. 2, 113 (1976).
7. A. M. Sukhotin et al., At. Energ., 36, No. 6, 496 (1974).
8. A. G. Akimov et al., Izv. Akad. Nauk SSSR, Ser. Khim., No. 6, 1239 (1978).
9. F. Honda and K. Hirokawa, J. Electron Spectrosc. Relat. Phenom., No. 8, 199 (1976).
10. C. Leygraf, S. Ekelund, and G. Schön, Scand. J. Metall., No. 2, 313 (1973).
11. A. G. Akimov et al., Izv. Akad. Nauk SSSR, Ser. Khim., No. 7, 1482 (1978).
12. G. Ertel and K. Wandelt, Surface Sci., 50, 479 (1975).
13. W. Carter and G. Schweitzer, J. Electron Spectrosc. Relat. Phenom., No. 5, 827 (1974).
14. A. G. Akimov, I. L. Rozenfel'd, L. P. Kazanskii, and G. V. Machavariani, Izv. Akad. Nauk SSSR, Ser. Khim., 6, 1245 (1978).
15. M. Oku, K. Hirokawa, and S. Ykeda, J. Electron Spectrosc. Relat. Phenom., No. 7, 475 (1975).

CATALYTIC FLUORINATION OF URANIUM TETRAFLUORIDE AND URANYL FLUORIDE

G. A. Yagodin, É. G. Rakov, V. I. Goncharov, S. V. Khaustov, S. A. Sharkov, and V. A. Yurmanov

UDC 546.791.161:546.16:541.128.13

Uranium tetrafluoride and oxides are important intermediates in the production of uranium hexafluoride; the reactions of their fluorination have been generalized in [1, 2]. In a study of the kinetics of the interaction of UF_4 with fluorine, it has been established [3] that for samples with different specific surfaces S_{sp}, the activation energy E is 15.5-19.9 kcal/mole (1 cal = 4.1840 J), the order of the reaction with respect to fluorine is equal to one, and the process is described by the equation of the contracting sphere.

Fluorination of uranium oxides is accompanied by a rapid formation of uranyl fluoride and a subsequent slower conversion of it to the hexafluoride. The value of E for UO_2F_2, obtained in the course of fluorination of oxides, was equal to 21.3-23.7 [4, 5] and 20.4-26.0 kcal/mole [6-8]. The order of the reaction with respect to fluorine is about one [6]. The values of the kinetic parameters for UO_2F_2 are approximately the same as for the reactions of other oxides and oxofluorides with fluorine [9].

Recently the authors of [10] found that additions of cerium, silver, tin, and antimony oxides have a catalytic effect on the fluorination of UO_2. According to their data, the catalyst does not change E, but it increases the value of the preexponential factor k_0 by more than two orders of magnitude. Earlier the possibility of catalytic oxidation of UF_4 by oxygen [11-13] and the catalytic reduction of UO_2F_3 and UO_3 by hydrogen [12, 14] was established. High catalytic activity of silver fluoride in the reactions of fluorine with CrF_3 and WO_3 was demonstrated [15, 16].

The purpose of the present work was to investigate the fluorination of UF_4 and UO_2F_2 in the presence of NiF_2 and CuF_2, which, according to [15-17], possess moderate catalytic activity and therefore are convenient for elucidating the peculiarities of processes.

Experimental Methods

The investigations were conducted by a gravimetric method on the setup described in [18]. Length of the reactor 400 mm, diameter 40 mm. Fluorine was produced by electrolysis of molten KH_2F_3 at 80-90°C and purified in a column with granulated NaF. The dilution of fluorine was performed with nitrogen dried with silica gel. The consumption of fluorine was regulated by

Translated from Atomnaya Énergiya, Vol. 49, No. 3, pp. 169-173, September, 1980. Original article submitted July 9, 1979.

 0038-531X/80/4903-0620$07.50

TABLE 1. Conditions of Synthesis and Properties of Catalysts

Catalyst	Conditions of synthesis: initial substance	reagent	temp., °C	S_{sp}, m^2/g	Color
N-1	$Ni_3(OH)_4CO_3 \cdot 4H_2O$	F_2	160	91,7	Brown
N-2	$NiCO_3 \cdot xH_2O$	HF	170	91,9	Yellow
N-3	$Ni_3(OH)_4CO_3 \cdot 4H_2O$	HF	170	74,5	»
N-4	$NiCO_3 \cdot xH_2O$	F_2	200	69,0	Brown
N-5	H-2	F_2	200	64,2	»
N-6	$Ni_3(OH)_4CO_3 \cdot 4H_2O$	F_2	200	38,7	Gray-green
N-7	$NiF_2 \cdot 4H_2O$	F_2	200	26,2	The same
N-8	$NiCl_2 \cdot xH_2O$	F_2	300	25,4	» »
N-9	$NiF_2 \cdot 4H_2O$	F_2	300	19,3	» »
N-10	$NiCl_2$	F_2	350	9,0	Yellowish gray
N-11	$NiF_2 \cdot 4H_2O$	F_2	500	8,8	The same
N-12	NiO	F_2	400	7,7	» »
N-13	$NiCl_2 \cdot xH_2O$	F_2	550	3,5	» »
N-14	$NiF_2 \cdot 4H_2O$	F_2	600	2,8	Yellow
N-15	$NiF_2 \cdot 4H_2O$	HF	700	2,0	»
CuF_2	$CuF_2 \cdot 2H_2O$	F_2	300	5,2	Colorless

varying the current strength and was periodically monitored by an analytical method; the consumption of nitrogen was measured with the aid of a preliminarily calibrated manostat–rheometer system or with an RS-3A rotameter. The processes were investigated at atmospheric pressure under conditions of the absence of external diffusion inhibition at a rate of flow of the gas mixture 1.0-2.0 liters/min.

Samples of UF_4 and UO_2F_2 with specific surface 0.8 and 1.0 m^2/g, respectively, were produced by the usual methods [3, 6] (Table 1). The specific surface was measured by the Brunauer–Emmett–Teller method; the composition of the synthesized samples was monitored by the methods of chemical and x-ray phase analysis, performed on URS-50I and Dron-1 diffractometers. Mixtures of substances to be fluorinated with catalysts were prepared by shaking precise weighed samples of the substances in glass weighing bottles. The results were treated by the least-squares method with a Mir-2 computer (at the 95% probability level).

Results and Discussion

In the treatment of the data of Table 1 it was found that S_{sp} of NiF_2 catalysts is related to the absolute temperature of their synthesis (T) by the function

$$\lg S_{sp} = (1.2 \pm 0.2) \cdot 10^3 T^{-1} - (0.9 \pm 0.3).$$

The presence of such a dependence within the entire investigated temperature range is difficult to explain only by the usual sintering, since it occurs at a temperature below the Tamman point; according to the estimate, this points lies close to 500°C for NiF_2.

The rate of noncatalytic fluorination of UF_4 (fraction with particle size 50-63 μm) at a partial pressure of fluorine p_{F_2} = 1.0 atm (1 atm = $1.01 \cdot 10^5$ Pa) is described by the equation of a contracting sphere

$$1 - (1 - \alpha)^{1/3} = 10^{(5.4 \pm 0.8)} \cdot \tau \exp\left[- (19700 \pm 1900)/RT \right] - (0.03 \pm 0.01),$$

where α is the degree of reaction by the time τ. Good correspondence to the results of [3] is observed.

The introduction of a relatively large amount of catalysts does not change the form of the kinetic equation (Figs. 1 and 2), which agrees with the conclusions of [10]. However, the addition of a catalyst changes not only k_0, but also, contrary to the data of [10], E as well.

As can be seen from the results presented in Table 2 and their comparison with the data of [1-9], catalysts increase the rate of interaction severalfold; they may increase E, decrease it, or leave it unchanged. In the case of a substantial decrease in E there is a simultaneous decrease in k_0; therefore, one can speak of the presence of compensation for the change in E by the change in k_0.

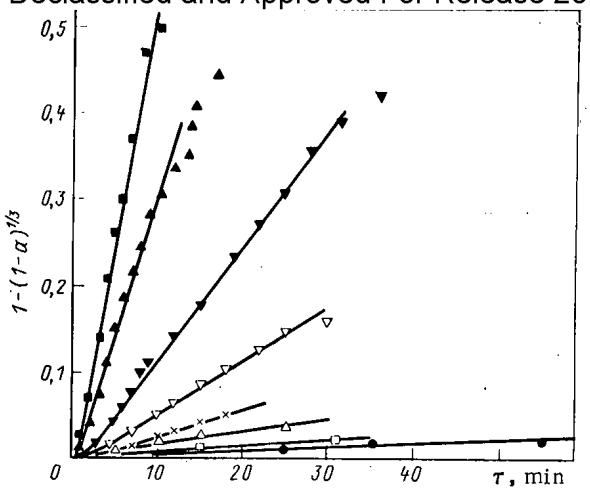

Fig. 1

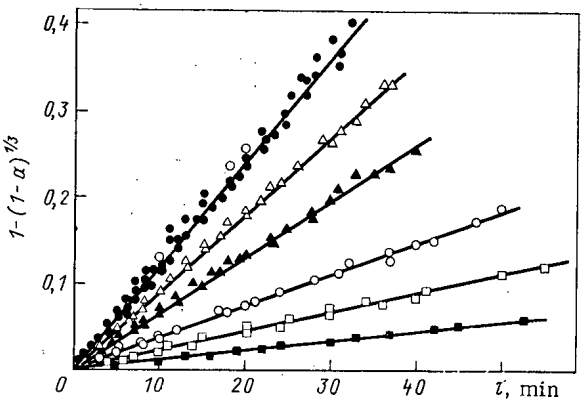

Fig. 2

Fig. 1. Catalytic curves of the fluorination of UF_4 (50-63 μm) in a mixture with N-12 (50-63 μm) at M_0 = 0.50, p_{F_2} = 1.0 atm, and temperature 140 (●), 150 (□); 160 (Δ); 183 (×), 190 (▽), 200 (▼), 220 (▲), and 230°C (■).

Fig. 2. Kinetic curves of fluorination of UO_2F_2 (40-50 μm) in a mixture with N-7 (40-125 μm) at M_0 = 1.0, p_{F_2} = 0.08 atm, the temperature 200 (■), 120 (□), 220 (○), 230 (▲), 240 (Δ), and 250°C (●).

TABLE 2. Basic Kinetic Parameters of Fluorination Reactions

Substance	Catalyst	M_0	$k \cdot 10^3$ (min^{-1}) at various temp., °C											E, kcal/mole	log k_0, min^{-1}
			140	150	160	180	200	210	220	230	240	250	260	280	
UF_4	—	—							1,0		2,1		3,7	8,2	19,7±1,9	5,4±0,8
UF_4	N-10	0,50					13,1	20	26	51					21,4±2,5	7,9±1,2
							13,5	20	27	52						
								21	28							
UF_4	N-12	0,66	0,4	0,9	1,1	3,1	12,6		33	54					22,4±2,6	8,4±1,2
UF_4	N-12	0,50	1,4		5,3	13,9	21		34		47				14,1±3,3	4,8±1,6
											51					
UF_4	N-12	0,25		1,5		2,9	13,4								16,7±8,2	5,7
UF_4	CuF_2	0,50							2,3		6,2			30	2,5±8,2	19,5
														44		
UO_2F_2	N-7	1,0					1,0	2,1	3,5	6,2	7,9	11,4		26	22,5±8,2	8,1±0,1
								2,2	3,6	6,3	8,9	11,8		28		
										6,8		11,9				
												12,4				
												12,6				

Note. The data for UF_4 were obtained at p_{F_2} = 1.0 atm; for UO_2F_2 at p_{F_2} = 0.08 atm; the rate constants for pure UF_4 at 290, 300, and 320°C are $12 \cdot 10^{-3}$, $(16\text{-}20) \cdot 10^{-3}$, and $26 \cdot 10^{-3}$ min^{-1}, respectively; M_0 is the initial mass ratio of the catalyst and substance to be fluorinated.

Catalysts lower the order of the reaction with respect to fluorine: the data of Table 3 are evidence that for UO_2F_2 it is 0.5 ± 0.1; the dependence of the reaction rate of PF_2 in logarithmic coordinates for UF_4 is not linear; however, on each portion of it the order of the reaction is lower than one. A decrease in the order of the reaction to ≈0.5 may be associated with the occurrence of dissociation of fluorine on the surface of the catalyst, although the possibility remains that this may be due to limitation of the reaction by adsorption of fluorine, occurring in the Freudlich region.

The rate of fluorination of UF_4 increases with increasing S_{sp} of NiF_2 catalysts (Table 4) according to a nearly parabolic dependence:

$$k = 10^{-(2.8 \pm 0.2)} S_{sp}^{(0.5 \pm 0.1)}.$$

Such a dependence may be due to a hindrance of the diffusion of fluorine into the grain of the catalyst, a decrease in the thickness of the outer "working" layer of the grain on account of a decrease in the diameter of the channels between primary particles comprising the

TABLE 3. Rate of Fluorination of UO_2F_2 (40-63 μm) in a Mixture with N-7 (40-125 μm) at M_0 = 1.0, t = 250°C, and UF_4 (63-125 μm) in a Mixture with N-10 (50-63 μm) at M_0 = 0.50, t = 210°C

$k \cdot 10^3$, min^{-1}	p_{F_2}, atm						
	0,01	0,02	0,04	0,06	0,08	0,10	1,00
For UO_2F_2	4,2	5,8 6,2	8,1	10,2	11,4 11,8 11,9 12,4 12,6	13,7	
For UF_4	3,3	4,7	9,4	11,9 13,0			19,4 20,5

TABLE 4. Rate of Fluorination of UF_4 (63-125 μm) in a Mixture with Catalysts (<125 μm) at M_0 = 0.11, PF_2 = 1.0 atm, and t = 200°C

Catalyst	$k \cdot 10^3$, min^{-1}	Catalyst	$k \cdot 10^3$, min^{-1}
N-1	16; 18	N-9	5,7
N-2	19; 23	N-10	7,4
N-3	18	N-11	6,9; 7,1
N-4	12	N-13	3,2
N-5	9	N-15	1,3
N-6	10; 13		

grain, with increasing S_{sp}. In an investigation of such catalytic reactions, a very strict standardization of the conditions is necessary, since k depends on the temperature, p_{F_2}, S_{sp} of the catalyst and the substance to be fluorinated, the grain size of the catalyst and particle size of the substance, the porosity of the grains of the catalyst, M_0, and even on the time of stay of the catalyst in an atmosphere of fluorine before the measurements of the rate (Table 5, Fig. 3).

When the catalyst obtained in an atmosphere of HF is used, with high S_{sp}, the kinetic curves have breaks that appear at all values of the investigated temperature. Preliminary treatment of the catalysts with fluorine lowers S_{sp} from 79.9 to 64.2 m^2/g, changes its color from yellow to brown, and leads to disappearance of the breaks on the kinetic curves. The rate of the reaction with a catalyst treated in a stream of fluorine becomes equal to the rate at the third step. It can be assumed that when a freshly prepared catalyst is used directly, there is a chemisorption of fluorine, which lowers the catalytic activity and S_{sp}.

It is interesting that the appearance of a brown color in an atmosphere of fluorine was also observed in other samples of NiF_2 with a developed surface. When the samples are heated in a stream of nitrogen or in air, the color changes to gray-green, and the mass of the samples thereupon decreases. Evidently the chemisorption of fluorine on NiF_2, described by the authors of [19], may turn into the formation of brown nonstoichiometric fluorides NiF_{2+x}. There is a compensation dependence between the values of E and k_0 cited in Table 5 (Fig. 4); therefore, a decrease in E does not cause any acceleration in the reaction.

Analyzing the data obtained as a whole, we can conclude that reactions in systems of powdered substance to be fluorinated – powdered catalysts – fluorine possess certain specific peculiarities, which have not been entirely investigated and therefore do not find an unambiguous explanation. Evidently, one of the most important stages is the interaction of fluorine with the surface of the catalyst, resulting in the formation of active particles (atoms, molecules, or ions), which migrate along the surface of the catalyst and partially in the volume of the gas toward the surface of the particle to be fluorinated, where the fluorination reaction is localized. The energy necessary for the formation of active particles is liberated in highly exothermic reactions of fluorination and is rapidly transferred from the surface of the sub-

TABLE 5. Kinetic Parameters of the Fluorination of UF_4 (63-125 μm) in a Mixture with N-2 (40-50 μm) at M_0 = 0.11 and pF_2 = 1.0 atm.

Stage of reaction	$k \cdot 10^3$ (min^{-1}) at t, °C						E, kcal/mole	$\lg k_0$; min^{-1}
	180	190	200	210	220	230		
1	3,0	5,2	9	17	25	31	22,3±3,8	8,2±1,7
2	2,2	4,8	6	10	17	20	19,9±4,0	6,9±1,8
3	2,2*	3,7	5,8	7	14	14	15,8±3,2	5,0±1,4

*The third portion of the kinetic curve is absent at this temperature.

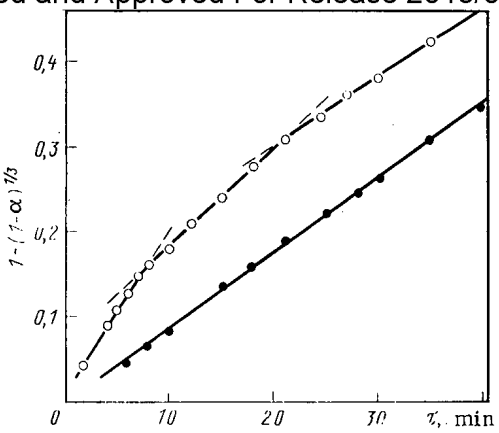

Fig. 3

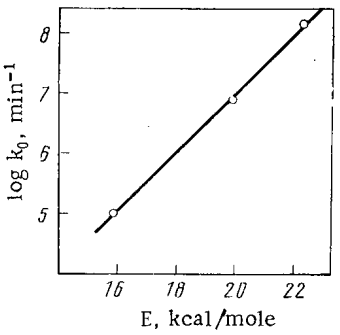

Fig. 4

Fig. 3. Kinetic curves of the fluorination of UF_4 (63-125 μm) in a mixture with N-2 (<125 μm) at M_0 = 0.11, p_{F_2} = 1.0 atm, and t = 200°C: ○) freshly prepared catalyst; ●) catalyst treated with fluorine at p_{F_2} = 1.0 atm, t = 200°C for 20 min.

Fig. 4. Compensation dependence of the kinetic paramters for various stages of fluorination of UF_4 (63-125 μm) in a mixture with N-2 (<125 μm) at M_0 = 0.11, p_{F_2} = 1.0 atm, and t = 200°C.

stance to be fluorinated to the surface of the catalyst as a result of the small distance between them.

The ability of NiF_2 to form nonstoichiometric unstable higher fluorides suggests that their decomposition proceeds with a liberation of atomic fluorine, which is such an active particle. This is also evidence by the use of nickel at a higher temperature for the thermocatalytic generation of atomic fluorine [20]. The catalysts described have a relatively low activity; a search for and investigation of more active substances will be necessary for practical use in processes of fluorination.

LITERATURE CITED

1. N. P. Galkin et al., Chemistry and Technology of Fluorine Compounds of Uranium [in Russian], Atomizdat, Moscow (1961).
2. J. Schmets, At. Energy Rev., 8, No. 1, 3 (1970).
3. V. Labaton and K. Jonson, J. Inorg. Nucl. Chem., 10, Nos.1/2, 74 (1959).
4. M. Iwasaki, ibid., 26, No. 11, 1853 (1964).
5. T. Yahata and M. Isawaki, ibid., 1863.
6. Z. B. Mukhametshina et al., in: Transactions of the D. I. Mendeleev Moscow Chemotechnological Institute [in Russian], No. 75 (1973), p. 42.
7. T. Sakurai, J. Phys. Chem., 78, No. 12, 1140 (1974).
8. N. A. Naumenko et al., in: Transactions of the D. I. Mendeleev Moscow Chemicotechnological Institute [in Russian], No. 85 (1975), p. 52.
9. É. G. Rakov and V. A. Kolzunov, Zh. Neorg. Khim., 22, No. 5, 1165 (1977).
10. T. Maeda and E. Yagi, Inorg. Nucl. Chem. Lett., 14, No. 10, 341 (1978).
11. A. Ekstrom and G. Batley, ibid., 9, No. 11, 1157 (1973).
12. A. Ekstrom, G. Batley, and D. Jonson, J. Catal., 34, No. 1, 106 (1974).
13. G. Batley and A. Ekstrom, ibid., No. 3, 360.
14. G. Batley, A. Ekstrom, and D. Jonson, ibid., 368.
15. G. A. Yagodin et al., Zh. Neorg. Khim., 23, No. 3, 832 (1978).
16. G. A. Yagodin et al., in: Transactions of the D. I. Mendeleev Moscow Chemicotechnological Institute [in Russian], No. 99 (1978), p. 127.
17. G. A. Yagodin et al., ibid., p. 11.
18. V. V. Goncharov and S. V. Khaustov, ibid., No. 97 (1977), p. 95.
19. N. Watanabe and M. Takashima, Koguo Kagaku Zassi, 74, No. 3, 321 (1971).
20. V. A. Legasov, Vestn. Akad. Nauk SSSR, No. 12, 3 (1976).

LONG-TERM STRENGTH OF ELECTRICAL CERAMIC UNDER A LOW FLUENCE

Yu. B. Zverev, V. I. Ponomarev,
N. S. Kostyukov, and Yu. F. Tuturov

UDC 539.4:666.3/7:621.039.531

An experimental study was made of the long-term strength of seven types of electrical ceramics under the conditions of steady-state and pulsed γ-neutron and steady-state γ radiation. During the study, laws governing the reduction of the long-term strength under the effect of various forms of radiation were established and the influence of the stressed state of the irradiated material was considered.

As is known, the ultimate strength and the modulus of elasticity of ceramic materials under the action of steady-state γ-neutron radiation do not change at a fluence of up to 10^{19}-10^{20} neutrons/cm^2 [1, 2]. However, the strength of ceramics under the conditions of constant mechanical loads is reduced under the influence of corrosion processes occurring at the tips of surface technological cracks [3, 4] and irradiation can accelerate and stimulate chemical reactions, thus causing the long-term strength to decrease. We studied the influence of steady-state and pulsed γ-neutron and steady-state γ radiation on the long-term strength of seven types of electrical ceramics: SK-1 and SNTs steatites, M-23 porcelain, UF-46 ultraporcelain, L-24 cordierite, microlite, and GB-7 high-alumina ceramic.

Initially, we investigated the influence of irradiation on the time to failure under the conditions of pulsed γ-neutron radiation. For this purpose we used cylindrical specimens with a diameter of 5 mm and length 50 mm, which were subjected to three-point bending with a constant mechanical stress of 0.4-0.9 of the ultimate strength as determined by testing no fewer than 50 specimens of the given batch. The loaded specimens were then irradiated with a bell-shaped γ-neutron pulse with a half-width of 2 msec. The neutron spectrum was similar to the fission neutron spectrum. The maximum neutron flux density in a pulse of energy γ 0.1 MeV did not exceed $(1.5\text{-}2.5)\cdot10^{17}$ neutrons/cm$^2\cdot$sec while the dose rate of the attendant γ radiation was $(0.7\text{-}1.3)\cdot10^5$ C/kg. The neutron fluence was 10^{12}-$4.5\cdot10^{14}$ neutrons/cm^2. The tests were conducted in air at room temperature.

As a result of the large scatter (hundreds of percents) of the experiment values, the time to failure was estimated from the plot of $\ln(1-P) = f(\tau)$, where P is the probability of failure, which is equal to the ratio of the number of fractured specimens to the total number of specimens tested and τ is the time to failure found experimentally. The mean time to failure was found from the results for 16-25 specimens at each level of applied stress, as the quantity reciprocal to the slope of the straight line of the given plot.

The averaged results of tests for all materials were used to plot $\ln\tau$ against the applied stress (Fig. 1). These plots constitute a family of straight lines with a knee at a quite high stress and if they are extended (dashed lines), they meet at one point at a stress equal to the ultimate strength. In the region of stresses beyond the bend point the irradia-

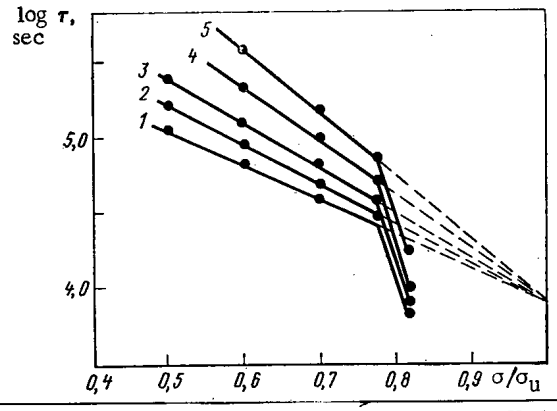

Fig. 1. Mean time to failure vs applied stress for steatite SK-1: 1) fluence $4.3\cdot10^{14}$ neutrons/cm^2; 2) $3.5\cdot10^{13}$ neutrons/cm^2; 3) 10^{13} neutrons/cm^2; 4) 10^{12} neutrons/cm^2; 5) unirradiated specimens.

Translated from Atomnaya Energiya, Vol. 49, No. 3, pp. 173-176, September, 1980. Original article submitted March 12, 1979.

0038-531X/80/4903-0625$07.50

TABLE 1. Values of F_0 and Coefficients t_0, k, and α

Material	F_0, neutrons/cm^2	t_0, sec	k	α
Steatite	10^{11}	$8 \cdot 10^3$	0,5	9,0
SNTs steatite	10^7	$1,5 \cdot 10^4$	0,67	17,5
M-23 porcelain	$2,25 \cdot 10^{10}$	$8 \cdot 10^3$	1,93	27
UF-46 ultraporcelain	$4,6 \cdot 10^{11}$	$1,26 \cdot 10^4$	0,435	9,5
L-24 cordierite	$4 \cdot 10^{12}$	$3,54 \cdot 10^4$	1,54	20,45
GB-7 ceramic	10^{13}	$1,74 \cdot 10^4$	3,24	8,82

tion has practically no effect on the "lifetime" of the specimens, which is determined only by the applied load. After processing the experimental curves we obtained the following empirical relation which is valid for all materials tested, apart from microlite:

$$\tau = t_0 (F_0/F)^{k(1-\sigma/\sigma_u)} \exp [\alpha (1 - \sigma/\sigma_u)]. \quad (1)$$

where τ is the mean time to failure (sec); σ, applied stress; F, fluence of neutrons with $E \geqslant 0.1$ MeV; σ_u, ultimate strength; F_0, threshold fluence value below which the material behaves as unirradiated material; and t_0, k, and α, empirical coefficients. The numerical values of the empirical coefficients and F_0 are given in Table 1.

The values of the mean time to failure, obtained by the technique described above, under irradiation in the stress state were compared with the mean time to failure, found for specimens preirradiated to the same fluence values and then subjected to the same stresses. The comparison showed that in tests for long-term strength, no role is played by the state, loaded or not loaded, in which the material is irradiated and that only the value of the fluence has the effect of shortening the time to failure.

To determine the influence of γ radiation in reducing the time to failure, we irradiated the specimens of all materials on a steady-state γ-ray apparatus with a ^{60}Co source at an exposure dose rate of 0.12 C·kg^{-1}·sec^{-1} to a value of 260 C/kg (the maximum dose of the attendant γ radiation in a pulse did not exceed 130 C/kg). We then tested the specimens under two different loads and found the mean time to failure; this time was then compared with the values obtained for the unirradiated specimens. The results of this comparison revealed that γ radiation within the limits indicated does not affect the mean time to failure. Therefore, the reduction of the lifetime of the material is determined entirely by the pulsed neutron flux.

For the sake of comparing the action of the steady-state and pulsed γ-neutron radiation, the specimens of SNTs steatite and M-23 porcelain were subjected to steady-state irradiation. The mean time to failure was determined for two different loads at a fluence of $3.5 \cdot 10^{13}$ and $4.3 \cdot 10^{14}$ neutrons/cm^2. The steady-state irradiation was carried out for 1 and 20 h with two values of neutron flux densities with similar spectra. As a result, it turned out that with preirradiation in both the steady-state and pulsed modes, the time to failure depends in the same way on the stress and on the fluence but does not depend on the neutron flux density and is characterized by Eq. (1).

Steady-state irradiation of ceramic in the stress state, however, can lead to different results. In this case two processes act on the material under load: stress corrosion and accumulation of defects during irradiation. The corrosion rate will increase continuously as a defect concentration grows and at low radiation intensity will be limited by the rate of defect accumulation, i.e., it may depend on the density of the neutron flux. As a parameter for comparison it is convenient to take the probability of failure during a given time interval (24 h), which is related to the time to failure by

$$1 - P = \exp(-\lambda t), \quad (2)$$

where t is the time and λ is the Poisson distribution parameter; for unirradiated specimens

$$\lambda_0 = 1/\tau = (1/t_0) \exp [-\alpha (1 - \sigma/\sigma_u)], \quad (3)$$

and for specimens irradiated in the pulsed mode.

$$\lambda_F = 1/\tau = 1/t_0 (F/F_0)^{k(1-\sigma/\sigma_u)} \exp [-\alpha (1 - \sigma/\sigma_u)]. \quad (4)$$

To sum up, it can be said that both in the initial state and after irradiation failure of the specimens occurs at a finite rate characterized by a constant parameter λ, which is found

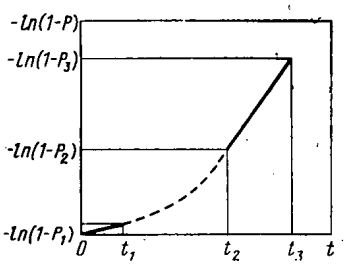

Fig. 2

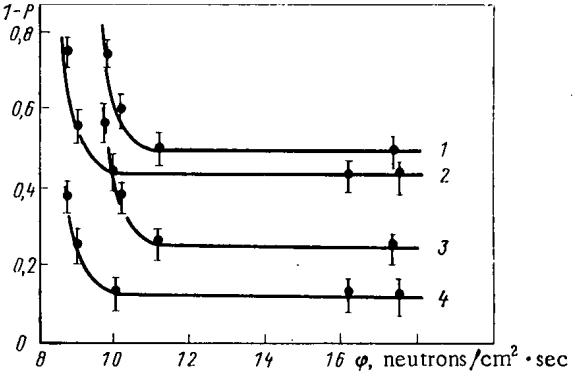

Fig. 3

Fig. 2. Time dependence of the logarithm of the failure probability under the simultaneous action of stress and steady-state γ-neutron radiation.

Fig. 3. Dependence of failure probability on neutron flux density for SNTs steatite: 1) stress $0.6\sigma_u$, F = $4.3\cdot10^{14}$ neutrons/cm^2; 2) stress $0.65\sigma_u$, F = $3.5\cdot10^{13}$ neutrons/cm^2; 3) stress $0.65\sigma_u$, F = $4.3\cdot10^{14}$ neutrons/cm^2; 4) stress $0.75\sigma_u$, F = $3.5\cdot10^{13}$ neutrons/cm^2.

from Eqs. (3) and (4). With steady-state irradiation the initial rate of failure will correspond to that observed in the unirradiated state; under irradiation the parameter λ_0 increases to a value λ_F and remains constant when irradiation ceases. The time dependence of the failure probability is shown schematically in Fig. 2. Here t_1 denotes the time during which the threshold value F of the fluence is built up ($t_1 = F_0/\varphi$, where φ is the neutron flux density). The time t_2 denotes cessation of irradiation ($t_2 = F/\varphi$, where F is the neutron fluence) and t_3 is the base time of the tests (24 h, in the given case). The relation $-\ln(1 - P) = f(t)$ in the interval $t_1 < t < t_2$ is approximated well by a function of the form bt^{α}, whence it follows that $\lambda = ba t^{\alpha-1}$. Using the boundary conditions and solving the equation for α and b, we get

$$a = 1 + k\,(1 - \sigma/\sigma_u); \tag{5}$$

$$b = \left(\frac{\varphi}{F_0}\right)^{k(1-\sigma/\sigma_u)} \frac{1}{t_0\,[1+k\,(1-\sigma/\sigma_u)]} \exp\left[-\alpha\,(1-\sigma/\sigma_u)\right], \tag{6}$$

where t_0, k, and α are constants (see Table 1). In the general form the failure probability is written as

$$P = 1 - \exp\{-[\lambda_0 t_1 + b\,(t_2 - t_1)^{\alpha} + \lambda_F\,(t_3 - t_2)]\}. \tag{7}$$

Under pulsed irradiation as well as in the case of a high flux density of steady-state irradiation, we have $t_1 \ll t_3$ and $t_2 \ll t_3$, and, therefore, Eq. (7) goes over into Eq. (2). Figure 3 shows the dependence of the failure probability on neutron flux density for SNTs steatite. The points on the curves correspond to the experimental values under irradiation in the stress state while the curves themselves were drawn according to calculated data. The experiments were performed with a fluence of $3.5\cdot10^{13}$ and $4.3\cdot10^{14}$ neutrons/cm^2; the irradiation time was $2\cdot10^{-3}$ and 10^{-4} sec in the pulsed mode and 1, 10, and 20 h in the steady-state mode. Similar results were also obtained for M-23 porcelain.

The critical neutron flux density, after which the failure probability remains constant, is determined from the condition $\exp[-b\,(t_2 - t_1)^{\alpha}] \geqslant \Delta P$, where ΔP is the error in the determination of the failure probability. Bearing in mind that in our case $t_1 \ll t_2$ and substituting the values of α and b in Eqs. (6) and (7), we get an equation in compact form

$$\varphi_{crit} = \frac{F\lambda_F}{a \ln (1/\Delta P)}. \tag{8}$$

Comparison of the results of irradiation with γ-neutron radiation and with steady-state γ radiation in increased doses was carried out with the assumption that reduction of the time to failure in irradiated ceramic is proportional to the concentration of displaced atoms. The concentration of displaced atoms under neutron irradiation was approximated from the Kin-

chin–Piza model [5], while in the case of γ radiation it was calculated by the familiar methods [6].

Computer calculations with allowance for the chemical composition of the materials studied and the mean values showed that with a dose rate of 0.12 C/kg·sec and a γ-quantum energy of 1.25 MeV the exposure dose equivalent to a fluence of $3.5 \cdot 10^{13}$ neutrons/cm^2 at a mean energy of 1 MeV is ∿15,500 C/kg.

Experimental verification confirmed the equivalence of the action of γ and γ-neutron radiation on the long-term strength of electrical ceramics.

Upon analysis of the results it was also established that a reduction of the time to failure under irradiation with identical doses is proportional to the content of the glass phase in the ceramic.

In conclusion, the authors thank A. A. Makarov for assistance with calculations of the cross section for the formation of displaced atoms under the action of γ radiation.

LITERATURE CITED

1. Radiation Resistance of Materials for Radio Engineering Equipment [in Russian], Sov. Radio, Moscow (1976).
2. N. S. Kostyukov, F. Ya. Kharitonov, and N. P. Antonova, Radiation and Corrosion Resistance of Electrical Ceramics [in Russian], Atomizdat, Moscow (1973).
3. S. Wiederhorn, in: Fracture Mechanics of Ceramics, Vol. 2, Plenum, New York (1974), p. 613.
4. W. D. Kingery, Introduction to Ceramics, Wiley, New York (1960).
5. M. W. Thompson, Defects and Radiation Damage in Metals, Cambridge Univ. Press (1969).
6. J. Deans and J. Winiard, Radiation Defects in Solids [Russian translation], IL, Moscow (1960).

MECHANISM OF RADON TRANSFER IN ROCKS AND THE DEPTH OF EMANATION METHODS OF LOOKING FOR RADIOACTIVE ORE

M. M. Sokolov, V. K. Titov, V. A. Venkov, E. E. Sozanskaya, T. L. Avdeeva, and E. I. Kuvshinnikova

UDC 550.835:553.262.4:546.296

The last few years have been characterized by a renewed interest in using emanation methods to look for radioactive raw materials. This can be partly explained by an introduction into search practice of exposure methods for measuring the concentration of radon, such as the emanation track method and the electron alphameter. The results express to a lesser degree the errors of the selection of the gas samples and the temporal variation of the radon concentration in soils connected with a classical emanation survey. By using these methods we repeatedly notice cases of the appearance of uranium–bearing ore bodies, bedded at depths of tens of meters and, in several cases, up to 100-150 m. Such a depth* of emanation methods is not explained from the viewpoint of existing ideas about the migration of radon and therefore deserves an independent discussion. According to these ideas, the depth of the emanation methods does not exceed the first few meters, even for large bodies. Given this, it will be considered that diffusion is one of the basic processes, sometimes practically the only one, conducive to the transport of radon from the ore body to the surface [1].

During convection, the range of the emanation transfer increases; however, this process proves to have a noticeable influence on the transfer of emanation only from convection velocities greater than $2 \cdot 10^{-6}$ m/sec, which are thought to be improbable. Jeter [2] simulated the migration processes of gaseous radionuclides in soils above the uranium mineralization,

*By the depth of a method we mean that vertical distance at which, given the existing levels of technology, anomalous signals may be recorded above the mineralization.

Translated from Atomnaya Énergiya, Vol. 49, No. 3, pp. 176-179, September, 1980. Original article submitted September 28, 1979.

 0038-531X/80/4903-0628$07.50

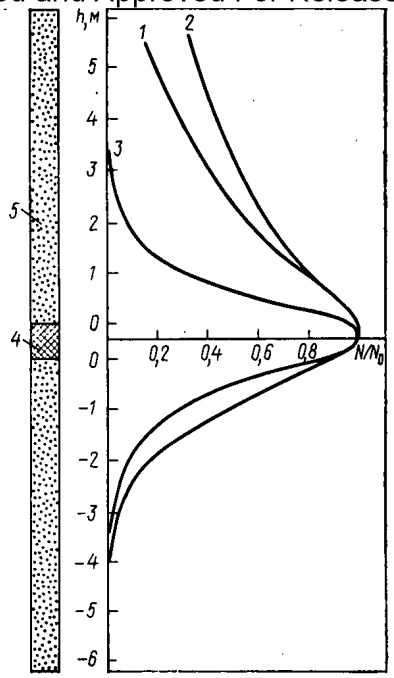

Fig. 1

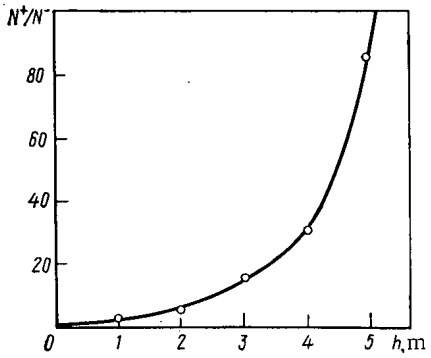

Fig. 2

Fig. 1. Radon distribution along the axis of the model, composed of detritus–sandy soil materials: 1, 3) radon distribution for the sealed and unsealed top of the model; 3) theoretical distribution accounting for diffusion; 4) emanation source; 5) detritus–sandy-soil material studied.

Fig. 2. Asymmetries of vertical transport of radon along the model axis.

assuming them to be based on molecular diffusion and convective transfer. According to the calculations, the constant transfer velocity of the soil–air is $1 \cdot 10^{-6}$ m/sec, which leads to an increase in the activity of gaseous radionuclides of several orders of magnitude above that in the diffusion model. According to Jeter, the depth of the emanation method, if one confirms the presence of this process, is essentially increased in comparison with the depth evaluated in the diffusion model. The questions of the depth of emanation methods and the mechanism of transfer of radon were illuminated by an independent discussion at the symposium in Vienna [3]. As a result, the participants came to the conclusion that the diffusion mechanism of radon transfer is insufficient to explain the empirical material.

The depth of the emanation methods was expediently measured by directly determining the velocity of radon transfer in various porous samples. The results of one of these experiments are presented in Fig. 1. The model consists of a full vertical cylinder with diameter 0.2 m and height 13 m. In the central part of the model is placed an emanation object (uranium ore of mass 60 kg with a mass fraction of uranium 0.2% and K_{em} = 30%), above and below which is the detritus–sandy-soil material (porosity 40% and bulk humidity 20%). The upper and lower parts of the model are sealed. Along the axis of the model there were film track detectors and standard cameras. The track density upon removal of the detectors from the models was counted after a month of exposure. We present the distribution of emanation along the axis of model 1, determined by the track method.

Figure 2 shows the ratio of the concentrations of emanation higher than (N^+) and lower (N^-) than the emanation source at identical distance from it. It is evident from the picture that the distribution of emanation upwards from the emanation source is essentially greater than below it. Moreover, at a distance of 5 m the coefficient of asymmetry (N^+/N^-) is already 100. Such an asymmetry of radon transfer from the emanation source indicates the probability of an essential influence of nondiffusive transfer of emanation in the model. To evaluate the influence of the convective transfer mechanism the radon was sealed in the upper part. After unsealing, the transfer of emanation in the part above the emanation source is essentially increased (see Fig. 1, curve 2). This gives evidence to a more gently sloping

TABLE 1. Velocity of Radon Transfer by Various Porous Samples

Material studied	transfer, 10^{-6} m/sec		Diffusion coeff. 10^{-6} m^2/sec	Transfer velocity due to diffusion, 10^{-6} m/sec
	max.	min.		
Air-dry sand	20	11	5	3,1
Air-dry loess	18	10	0,5	1,0
Detritus—sandy soil	29	12	1	1,4
Air-dry detritus sandy soil, humidity 20%	31	14	0,02	0,2

type of curve in the upper part of the model. Here part of the radon from the model moves away at the expense of exhalation. For comparison we now present a theoretical radon distribution curve assuming a diffusive transport mechanism (curve 3), calculated for an effective diffusion coefficient $D^* = 1 \cdot 10^{-6}$ m^2/sec, which is characteristic for the examined crushed-stone material. The comparison of the theoretical and experimental curves shows that the influence of diffusive transport of radon is essential only at distances not exceeding 2-3 diffusion lengths (in the model described 2-3 m). At distances 4-5 m from the emanation source the concentration of radon is 100-500 times greater than that predicted by the diffusion model.

One of the basic problems of this work was the establishment of the velocity of vertical transfer of radon in various porous deposits. To best approximate the natural layers, we used fine bore chinks settled at a depth of 10-12 m as models. In order to lessen the influence of extratubular processes, we used holes bored 15 years ago. The emanation ore material (200-600 kg of uranium ore with a mass fraction of 0.2% and an emanation coefficient of 20%) was placed in the lower part of the model and kept for accumulation for 3-8 days. We used dry and wet sand, loess, and detritus-loam material as the studied porous deposits. Before the arrangement of the studied material a model was flushed with atmospheric air to remove radon accumulated in air above the emanation source using a compressor for 20-50 multiple substitutions of the air in the column of the model. Essential removal of radon from the ore part of the model at this time does not occur.

In the upper part of each model at a depth of 0.8 m in the studied material we placed an electron emanation variometer, consisting of a silicon semiconductor detector of α radiation, arranged in a measuring chamber of standard volume. Variations in the concentration of radon in the measuring chamber were determined from the time of placing the material studied into the model by accumulating counts for 1 h. The results of some of the measurements obtained are presented in Fig. 3. All the curves have an identical characteristic. After placing the detectors, the count rate during the first hours grows due to radon formed in the very material being studied entering into the measuring chamber. After attainment of a stationary process, we observe a plateau region of a constant activity of the air in the chamber which is preserved until the moment when the radon from the emanation source has passed through the material studied. By knowing the distance between the surface of the emanation source and the detector and the time of the passage of the emanation from the ore into the measuring chamber, one may evaluate the transport velocity of the emanation in the conditions of the experiment. Such a value may be obtained for the maximum (at the time of passage of the first portion of the emanation, surely giving anomalous values of the calculated velocity) and the minimum (the asymptotic values of calculated velocity values) of the velocities of radon transfer in the conditions of the experiment (see Table 1).

The maximum and minimum values of the velocity of radon transfer in the experiment turned out to be 1-2 orders of magnitude higher than those values which may be attributed to diffusive transfer. The dampness of the material studied not only does not reduce the velocity of the radon transfer to the surface, but slightly increases it. The influence of water on the radon transfer was evaluated in a water model. Figure 4 shows the results of the measurement of radon concentrations using film detectors in the model filled with water and a theoretical diffusion curve for radon in water. A comparison of the curves shows that

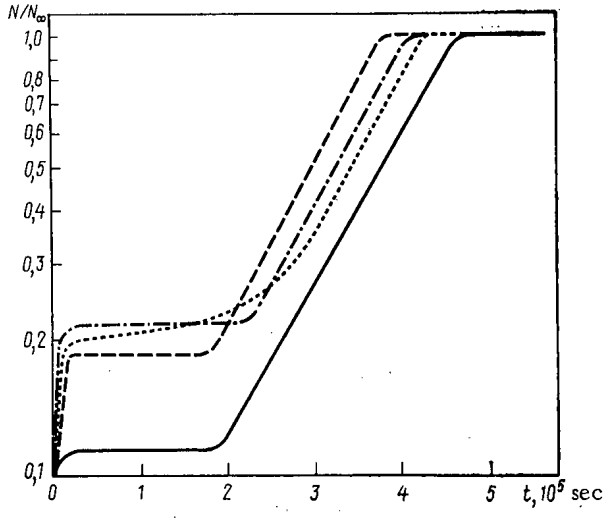

Fig. 3

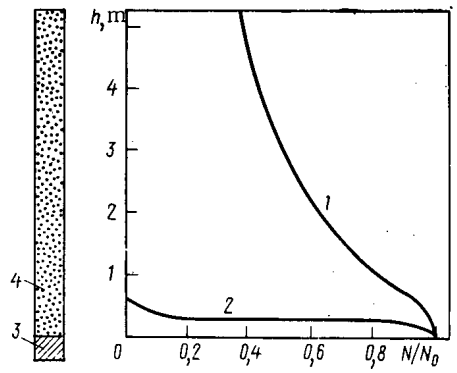

Fig. 4

Fig. 3. Growth of the count rate of the variometer during the time after placement of the model: —— and ----) air-dry crushed-loam material and the crushed-loam material with dampness 20% (h = 5.5 m); ··· and -·-·-) air-dry loess and the air-dry sand (h = 5 m).

Fig. 4. Radon distribution in a water model: 1) experimental radon distribution; 2) theoretical radon diffusion distribution; 3) emanation source; 4) water.

the transfer of emanation in stagnant water is the same as in previous cases, and cannot be connected only with a diffusion process.

Thus, one may evaluate the depth of contemporary emanation methods of searching for uranium deposits based on exposure measurements of radon concentration. For the obtained minimum and maximum values of the radon transport velocity in the porous samples studied, a 100-fold decrease in the concentration of emanation occurs for a depth at 30-50 m. Consequently, during favorable conditions emanation method depths of several tens of meters appear to be fully realizable. Still greater, evidently, may be the depth of a method due to the existence, in the earth's depths, of geothermal gradients giving rise to natural convective cells. Associated with such cells may be a steeply descending water-filled tectonic break with a high gas permeability. An increase in the depth of an emanation method may be caused by such a rising current of subsoil waters.

This work does not pretend to be a complete exposition on the question of the mechanism of radon migration in rock and soil. However, the information presented, obtained by contemporary methods of measurement, allows a reevaluation of the diffusion model foundation of the notion of the depth of one of the oldest methods of searching for radioactive raw materials — the emanation survey.

LITERATURE CITED

1. G. F. Novikov and Yu. N. Kapkov, Radioactive Methods of Prospecting [in Russian], Nedra, Moscow (1965), pp. 486, 499, 536.
2. H. Jeter et al., Energy Res. Abstr., 3, No. 8, 1749 (1978).
3. Exploration for Uranium Ore Deposits, IAEA, Vienna, pp. 185, 775.

A SEMIEMPIRICAL EXPRESSION FOR CALCULATING AVERAGE ENERGY LOSSES BY HEAVY IONS IN MATTER

E. L. Potemkin, V. V. Smirnov, and V. V. Frolov

UDC 539.186

In recent years considerable attention has been given to the calculation of average energy losses by heavy charged particles [1-10]. This interest is due to the use of beams of accelerated ions as an investigative instrument in various fields in experimental nuclear physics, solid-state physics, and radiobiology, and also to the use of ion beams for technological purposes.

At the same time, the theory of the slowing-down of charged particles does not provide a single analytic expression for the average energy losses in the energy range corresponding to the complete halting of an ion with an energy of ~10 MeV/nucleon. This has led to the development of empirical and semiempirical methods for calculating ion energy losses [4-6]. One of the most widely used is Brice's formula [6, 11]. This formula, using three free parameters, makes it possible to approximate the experimental data in the range of energies up to several MeV/nucleon. However, in the energy range above 1 MeV/nucleon and for heavy ions, Brice's formula becomes less applicable because the slowing-down model used by Brice does not match the real slowing-down mechanism. In order to remove these limitations, we proposed in [8] an expression using two slowing-down models: those of Firsov [7] and of Bethe and Bloch [2].

In the present study we analyze the results of the approximation of experimental data on average energy losses by means of this expression. We discuss the variation of the energy losses as a function of the velocities and atomic numbers of the colliding particles. The expression used in [8] takes account of the change in the number of electrons that results from overcharging and the interaction of electrons with the shielded charge of the nucleus of the oncoming particle; it has the form

$$S = S_1[(1-\gamma_1)Z_1 f(\chi') + Z_2 f(\chi'') + (\gamma_1 Z_1)^2 \gamma_2 Z_2 f(\chi''')], \quad (1)$$

where γ_1 is the relative number of electrons in the atom that have a velocity less than the velocity of the oncoming particle (in the present study we assumed in accordance with the Bohr model, that γ_1 is equal to the relative effective charge of an ion being slowed down in a medium); S_1 is the contribution made by one electron to the slowing-down cross section, determined by the formula of [6]. In [8] it was stated that the derivation of the expression for S_1 contains an error which leads to a coefficient of 8/3 in the low-energy region. Recently Brice [11] obtained a corrected analytic expression for S_1, but since in the low-energy region S_1 is proportional to 1/z and z is a free parameter, the additional coefficient does not affect the accuracy of the approximation of the experimental data. The expression for S_1 obtained in [11] has the form

$$S_1 = \frac{4\hbar^2}{5m}\left[\varepsilon^{1/2}\frac{30\varepsilon^2+68\varepsilon+46}{3(\varepsilon+1)^2} + (10\varepsilon+6)\operatorname{arctg}\varepsilon^{1/2}\right], \quad (2)$$

where $\varepsilon = (v/2Zv_0)^2$.

In order to take account of the variation of the number of electrons in the oncoming ion, the empirical function $f(\chi)$, introduced by Brice, was changed as follows:

$$\begin{gathered} f(\chi) = (1+\chi)^{-1}; \\ \chi' = (av/v_0)^n; \\ \chi'' = (av/v_0)^n/(1-\gamma_1); \\ \chi''' = (av/v_0)^4/\varphi(v); \\ \varphi(v) = 4Z^2a^4\left[\ln\frac{2mv^2}{\gamma_2 I} - (v/c)^2\right], \end{gathered} \quad (3)$$

Translated from Atomnaya Énergiya, Vol. 49, No. 3, pp. 179-182, September, 1980. Original article submitted January 8, 1979.

 0038-531X/80/4903-0632$07.50

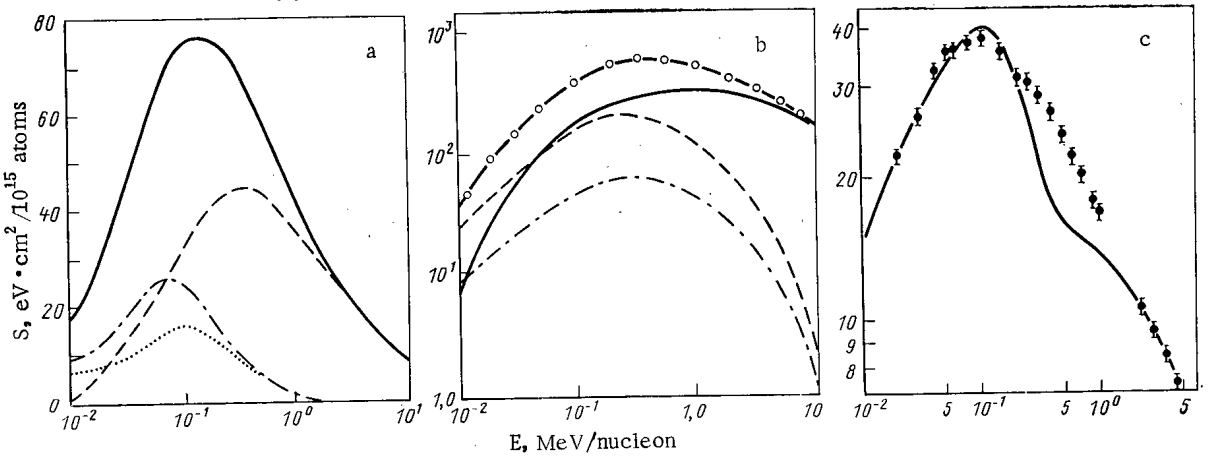

Fig. 1. Average slowing-down cross section (——) for the ions ^{8}Be in Be (a), ^{19}Fe in Ti (b) and ^{1}H in Ar (c): ....) contribution of the electrons of the slowed-down ion; -·-·-) contribution of the electrons of the target atom; ----) contribution of the nucleus-electron component; ○, ●) experimental results of [15] and [1], respectively.

where c is the speed of light and I is the average excitation potential of the target atom.

The first two terms of the sum (1) describe the electron–electron mechanism of slowing-down in accordance with Firsov's model; the third term represents the interaction of the shielded field of the nucleus of the ion with the electrons of the target atom, in accordance with the Bethe model. The first term is the sum of the contributions made by the electrons in the ion, and unlike Brice [5], we carry out the summation only over the electrons remaining in the ion at the given velocity. The second term includes a correction which takes account of the variation in the number of electrons in the slowed-down ion, and this leads to the appearance of a correction factor $(1-\gamma_1)^{-1}$ in the argument of the function f. With regard to the third term, it should be noted that it appears as a result of the consideration of "fast" collisions of the electrons of the atom with the shielded field of the ion nucleus [10].

Thus, for a sufficiently high ion velocity, the third term of the sum (1) takes account of the Coulomb excitation of the target atom and becomes the well-known Bethe–Bloch formula [2]. The variation of the numbers of interacting electrons of the target atom as a function of the velocity of the slowed-down ion actually reflects the shielding effect of the inner shells. For this reason, the factor γ_2 was introduced into the expression $\ln(2mv^2/\gamma_2 I)$.

Expression (1) corresponds to a slowing-down model which uses two slowing-down mechanisms:the Firsov mechanism and the Bethe mechanism. Consequently, we must consider the possibility that slowing-down effects are taken into account twice. However, it can be seen qualitatively that this is very improbable, since the Firsov mechanism involved electrons with a velocity much higher than that of the ion, while the Bethe model involves electrons with a velocity much lower than that of the ion. But since the Firsov surface divides the space into "spheres of influence" of the atom and the slowed-down ion, there is obviously a contribution to the cross section made by the single-electron flux S_1 in the term describing the Coulomb excitation of the atom by the field of the ion.

To analyze the variation of contributions made by the components, we used experimental data on the slowing-down of α particles [12] and slowing-down cross-sectional curves from [13], which constitute an approximation of known tables [14].

Figures 1a and b show typical curves of the total slowing-down cross section and its components. It can be seen that for an energy of $\geqslant$1.0 MeV/nucleon the contribution of the Coulomb excitation is 90% or more of the total cross section. The electron components, which play the principal role at an energy of $\leqslant$0.3-0.5 MeV/nucleon, decrease rapidly as the energy increases, and at 10 MeV/nucleon they contribute less than 0.1%. It should be noted the contribution of the Coulomb excitation of the atom by the field of the ion increases as the atomic number Z_1 of the atom increases (for constant Z_2), which is due to the quadratic variation of the interaction cross section as a function of the ion charge, while the electron part varies linearly with the number of electrons. On the other hand, the variation of the Cou-

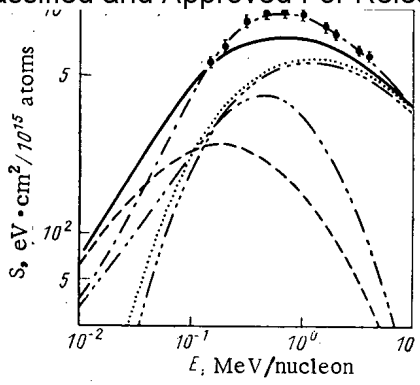

Fig. 2. Approximation of the experimental (●) [15] and tabulated (——) data [14] for ^{19}Fe in Ti ----, -·-·-·-) contribution of the electrons of the slowed-down ion and the target atom for the data of [1] and [15], respectively -·-·-, ····) contribution of the nucleus-electron component for the data of [14] and [15], respectively.

lomb excitation of the atom as a function of Z_2 is less marked, since it is analogous to the electron component, i.e., it is proportional to the "effective" number of electrons.

Figure 1c shows an "unfavorable" ion–target combination, when the ratio of atomic numbers Z_2/Z_1 is fairly high (in the present case $Z_2/Z_1 = 47$ [1]). This affects the shape of the "Firsov surface," which is very different from a plane. The clearly noticeable "two-humped" nature of the calculated curve can be attributed to the inadequate description of the interaction mechanism, i.e., when the mechanism of electron–electron interaction is no longer effective because the number of electrons in the incident ion is small, the Coulomb excitation of the atom is also ineffective, since the number of "fast" collisions is not yet large. This situation results in a considerable shift of the maxima of the various components with respect to each other, so that the behavior of the curve of the total slowing-down cross section does not agree with the physical laws.

As noted earlier, for the analysis of the behavior of Eq. (1) we use the data of [13] approximating the tables of [14], which in a number of cases diverge substantially from the

TABLE 1. Values of the Parameter z

Z_1	Z_2											
	Be	C	Al	Ti	Ni	Ge	Zr	Ag	Eu	Ta	Au	U
Be	0,817	0,940	0,916	0,048	1,179	1,201	1,204	1,183	1,544	1,644	0,863	2,067
C	0,564	0,876	0,814	0,927	1,045	1,007	1,014	1,063	1,297	1,311	1,353	1,320
Al	0,331	0,867	0,775	0,809	0,941	—	0,861	0,888	1,023	1,289	—	1,146
Ti	0,355	0,488	0,781	0,755	0,798	0,792	0,778	0,718	0,848	0,935	1,023	1,212
Ni	0,522	0,931	0,785	0,423	0,824	0,779	0,686	0,790	0,969	1,020	0,915	0,943
Ge	0,577	0,198	0,598	0,656	0,808	0,787	0,781	0,711	0,859	0,857	0,967	0,191
Zr	0,661	0,183	0,513	0,616	0,814	0,841	0,826	0,752	0,823	0,930	0,742	0,179
Ag	0,706	1,019	0,855	0,910	0,847	0,792	0,766	0,792	0,979	0,202	0,857	—
Eu	0,917	0,144	0,595	0,553	0,625	0,890	0,841	0,762	0,781	0,852	0,977	0,198
Ta	0,993	0,142	0,584	0,567	0,889	0,954	0,777	0,682	0,727	0,742	0,774	0,191
Au	0,984	0,141	0,712	0,708	0,815	0,275	0,887	—	—	—	—	—
U	1,124	—	0,250	0,649	0,693	0,645	—	0,701	—	—	0,796	0,233

TABLE 2. Values of the Parameters α

Z_1	Z_2											
	Be	C	Al	Ti	Ni	Ge	Zr	Ag	Eu	Ta	Au	U
Be	0,437	0,369	0,415	0,387	0,385	0,385	0,357	0,374	0,332	0,320	2,284	0,245
C	0,954	0,385	0,434	0,406	0,397	0,399	0,394	0,366	0,366	0,394	0,400	0,485
Al	4,094	0,452	0,476	0,462	0,406	—	0,423	0,390	0,438	0,314	—	0,435
Ti	4,500	2,226	0,585	0,539	0,564	0,513	0,478	0,480	0,563	0,491	0,380	0,540
Ni	2,546	0,564	0,552	0,326	0,549	0,540	0,573	0,447	0,385	0,559	0,569	0,561
Ge	1,946	4,500	1,024	0,814	0,601	0,553	0,492	0,496	0,530	0,559	0,461	4,500
Zr	1,746	4,500	1,670	1,051	0,639	0,512	0,451	0,395	0,659	0,493	1,065	4,500
Ag	1,562	0,647	0,600	0,454	0,653	0,647	0,416	0,481	0,413	4,500	0,682	—
Eu	1,117	4,500	1,439	1,802	1,382	0,575	0,473	0,407	0,789	0,631	0,436	4,500
Ta	1,024	4,500	1,634	1,841	0,661	0,504	0,604	0,668	1,030	1,019	0,984	4,500
Au	1,010	4,500	1,050	0,964	0,659	4,365	0,607	—	—	—	—	—
U	0,790	—	5,000	1,282	1,246	1,347	—	0,780	—	—	0,891	0,812

TABLE 3. Values for the Parameter n

Z_1	Z_2											
	Be	C	Al	Ti	Ni	Ge	Zr	Ag	Eu	Ta	Au	U
Be	3,129	2 581	2,712	2,154	1,779	2,105	1,826	1,535	1,375	1,278	0,766	1,464
C	1,531	2,752	2,868	2,189	2,150	1,901	1,792	1,850	1,534	1,293	1,296	1,095
Al	1,310	2,764	2,899	2,246	2,425	—	1,969	2,002	1,604	4,500	—	1,338
Ti	1,270	1,367	4,301	2,334	2,232	2,229	2,029	1,330	1,464	1,561	1,605	4,500
Ni	1,059	3,032	3,312	1,569	2,513	2,138	1,288	2,142	2,182	4,500	1,573	1,391
Ge	1,171	2,494	1,585	1,684	2,384	2,267	2,137	1,340	1,622	1,369	1,555	2,376
Zr	1,145	2,738	1,449	1,518	2,374	2,693	2,510	1,332	1,429	1,612	1,055	2,490
Ag	1,261	2,705	3,325	4,417	2,336	1,928	1,336	2,064	2,033	2,224	1,403	—
Eu	1,228	3,413	1,519	1,166	1,649	2,832	2,391	1,245	1,315	1,383	1,610	2,300
Ta	1,129	3,491	1,453	1,133	2,386	3,544	1,851	0,960	1,143	1,085	0,983	2,377
Au	1,150	3,528	1,671	1,436	1,866	1,877	2,530	—	—	—	—	—
U	2,260	—	1,207	1,670	1,696	1 398	—	1,478	—	—	1,140	1,172

TABLE 4. Values of the Parameters z, a, and n for α Particles in Various Media

Z_2	z	a	n	Z_2	z	a	n	Z_2	z	a	n
1	1,123	0,277	2,832	18	1,912	0,166	1,768	35	1,406	0,349	0,952
2	1,429	0,237	2,152	19	1,313	0,233	1,399	36	2,107	0,176	1,595
3	0,766	0,742	1,655	20	0,876	0,478	1,098	37	2,801	0,206	1,439
4	0,668	0,897	1,691	21	0,734	0,827	0,945	38	1,415	0,282	1,238
5	1.234	0,324	2,220	22	0,700	1,062	0,887	39	1,642	0,222	1,420
6	1,707	0,228	2,672	23	0,643	1,745	0,815	40	1,452	0,251	1,198
7	1,685	0,207	1,840	24	0,776	0,506	0,713	41	1,265	0,328	1,056
8	1,198	9,277	0,709	25	0,657	3,254	0,672	42	1,449	0,273	1,052
9	2,291	0,252	1,456	26	0,819	1,286	0,750	43	1,607	0,217	1,212
10	1,949	0,183	0,687	27	1,037	0,967	0,658	44	1,901	0,172	1,171
11	0,698	5.000	0,627	28	1,098	1,280	0,521	45	1,949	0,169	1,109
12	0,407	5,000	0,894	29	1,255	1,544	0,390	46	2,846	0,127	1,695
13	0,405	5,000	0,973	30	0,869	5,000	0,531	47	2,543	0,120	1,216
14	0,340	3,019	1,186	31	0,688	5,000	0,662	48	1,720	0,229	0,766
15	1,028	0,444	1,343	32	0,611	5,000	0,699	49	1,324	0,507	0,572
16	1,537	0,235	1,614	33	0,641	3,041	0,820	50	0,711	5,000	0,572
17	1,673	0,183	1,463	34	0,659	4,257	0,752				

experimental results. Therefore, the results given here are qualitative rather than quantitative. This can be clearly seen in Fig. 2, in which we compare the calculations made on the basis of the experimental data of [15] and the approximations of the tables of [14]. For comparison, the figure also shows the contributions of various components in each case. It can be seen that while the contribution of the Coulomb excitation depends only slightly on the initial information, the electron component is rather sensitive to the shape of the fitted curve. Despite the merely qualitative nature of the work, we tabulate the parameters for Eq. (1) for different ion–medium combinations (Tables 1-4). The mean-square deviation is less than 1% for α particles and 1-4% for other ions.

In conclusion, the authors wish to express their gratitude to B. A. Chernyshev for his useful comments and his valuable advice.

LITERATURE CITED

1. L. Northcliffe, Phys. Rev., 120, 1744 (1960).
2. U. Fauo, Ann. Rev. Nucl. Sci., 13, 1 (1963).
3. B. Srivastava and Sh. Mukherji, Phys. Rev. A, 14, 718 (1976).
4. A. Chanbey and H. Gupta, Rev. Phys. Appl. 12, 321 (1977).
5. D. Brice, Phys. Rev. A, 6, 179 (1972).
6. W. Pietch, U. Hauser, and W. Neuwirth, Nucl. Instrum. Methods, 132, 79 (1976).
7. O. B. Firsov, Zh. Eksp. Tekh. Fiz., 36, 1517 (1959).
8. E. L. Potemkin and A. V. Sannikov, Preprint IFVÉ-80-41, Serpukhov (1980).
9. N. Bohr, Philos, Mag., 25, 10 (1933).
10. N. Bohr, Passage of Atomic Particles through Matter [Russian translation], IL, Moscow (1950).
11. D. Brice, Phys. Rev. A, 19, 1367 (1979).
12. J. Ziegler and W. Chu, Atom. Data Nucl. Data Tables, 13, 463 (1974).

13. D. Brice, Ion Implantation Range and Energy Deposition Distribution, Plenum Press, New York (1975).
14. L. Northcliffe and R. Shilling, Atom. Data Nucl. Data Tables, 14, 233 (1970).
15. D. Ward et al., AECL-5313 (1976).

LETTERS TO THE EDITOR

POSSIBILITY OF USING OXALIC ACID SOLUTIONS FOR DECONTAMINATING THE COOLANT CIRCUIT OF THE RBMK-1000 (REACTOR)

L. A. Mamaev, V. K. Nazarov, A. A. Malinin,
V. V. Morozov, and E. I. Yulikov

UDC 621.039.534...24

At present, the RBMK-1000 is employed as a standard reactor on nuclear power stations with ratings of more than 2000 MW [1]. The first of these stations, Leningrad, was started in 1973. The design of this station envisages a high quality of circulating water together with structural materials with a high resistance to corrosion. However, experience in the operation of water-moderated–water-cooled reactors has shown that oxide deposits [2-7] tend to form on surfaces in contact with the coolant (the core channels, pipes, separators, etc.), and that these deposits include the products of corrosion of iron and certain other metals, with traces of radionuclides.

The deposits reduce the heat-transfer properties of the working surfaces and when present in large quantities they represent a danger to the sealing of the fuel-element cans, which could lead to a considerable increase in the level of radioactivity. Removal of the deposits from the surfaces of the multiple forced circulation circuit (MFCC) is achieved by washing out the whole circuit with solutions of various compositions [5-7]. In this regard, we need to be able to assess the methods of decontamination of power station plant existing at the present time from the point of view of whether or not they can be used for boiling-water reactors.

An investigation and analysis of published data shows that certain solutions are highly effective in dissolving deposits in boiling water reactors and in decontaminating carbon and stainless steels. The majority of these solutions are made up on the basis of oxalic and acetic acids [7].

Considerable attention has been devoted to the oxidation–reduction method, which at the present time is one of the principal methods of decontaminating nuclear power station plant [7-10]. None of the methods tested was capable of fully satisfying the requirements imposed on the method for decontaminating the circuit of an RBMK-1000. The most serious obstacle to the use of these methods is the large number of operations involved and the high content of salts in the deactivating solutions. For example, the oxidation–reduction method involves from 6 to 9 operations (2-3 cycles) and complete replacement of the solutions at each operation.

In the case of the RBMK-1000 circuit (with a volume of ∿1200 m^3) the use of concentrated solutions and repeated filling of the circuit would result in the buildup of a large quan-

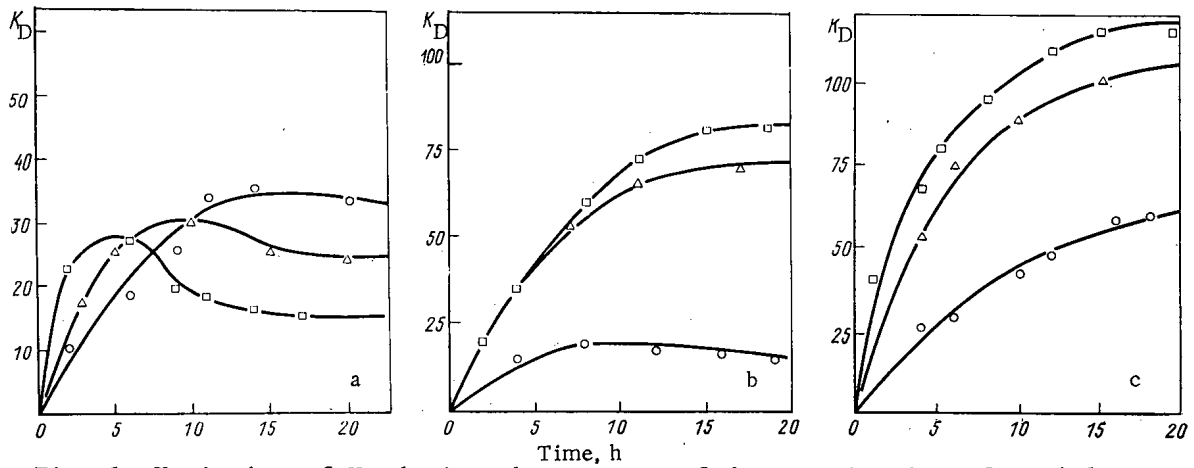

Fig. 1. Variation of K_D during the process of decontamination of stainless steel at 85°C for pH = 1, 2, and 3 (a, b, and c, respectively), and $H_2C_2O_4$ = 10 (○), 20 (△), and 39 (□) g/liter.

Translated from Atomnaya Énergiya, Vol. 49, No. 3, pp. 183-186, September, 1980. Original article submitted July 2, 1979.

0038-531X/80/4903-0637$07.50

TABLE 1. Decontamination of Carbon Steel by an Oxalic Acid Solution (V/S = 1.5 ml/cm², 90°C)

$H_2C_2O_4$, g/liter	pH	Decontamination time, h	K_D^*	Notes
10	1,1	5	3,8	Without correcting solution pH by ammonia
		10	2,5	
		15	2,6	
10	3	5	3,0	With solution pH corrected by ammonia
		10	9,1	
		15	19	
10	4	5	2,5	The same
		10	3,7	
		15	5,0	
10	5	5	2,1	» »
		10	5,7	
20	3	5	5,2	» »
		10	6,0	
20	5	5	4,4	» »
		10	5,9	

*K_D is the ratio of the β activities of the sample before and after decontamination.

TABLE 2. Effect of Hydrogen Peroxide on the Decontamination Effectiveness of Steel (V/S = 1.5 ml/cm², pH = 3, 90°C)

Composition of solution, g/liter		Decontamination time, h		K_D of the steel	
$H_2C_2O_4$	H_2O_2	full	in presence of H_2O_2	stainless	carbon
10	—	10	—	31	7,0
10	1,0	10	10	3,2	—
10	5,0	10	10	1,9	7,0
10	5,0	10	2*	5,5	12
20	—	10	—	31	6,0
20	0,1	10	10	7,4	—
20	1,0	10	10	3,9	—
20	5,0	10	2*	7,9	7,8
20	5,0	12	2*	33	—
20	5,0	15	3*	36	—

*The hydrogen peroxide is introduced into the solution 2-3 h prior to completion of the decontamination.

tity of effluent, which would greatly increase the cost of decontamination. Preliminary investigations have shown that a more promising way of decontaminating the RBMK-1000 circuit is to use solutions of oxalic acid.

Determining the Best Conditions of Deactivation for Stainless and Carbon Steels. We are already aware that decontamination is a complex physicochemical process which generates side effects having an effect on the final result (sorption and corrosion phenomena, the formation of secondary deposits, etc.). Quite apart from the purely technical side of the process (ensuring the necessary speed of filling the circuit, the speed of circulation and drainage of the solution, the use of various filters), the efficiency of decontamination is largely determined by the composition of the solutions.

To find the best composition of solution, we carried out experiments on decontaminating samples of carbon and stainless steels after these had been exposed to the circulating water of an RBMK-1000 reactor for 2 years and a VK-50 reactor for ∿1500 h, when running under normal operating conditions. When inspecting the samples of stainless steel type Kh18N10T, it was noted that their surfaces were covered by a deposit, the upper layer of which consists of a friable dark-brown deposit which was easily removed by mechanical treatment, while the lower layer adjacent to the surface of the metal took the form of a dense oxide film. No such clear division was observed in the layers on the carbon steel. Radiochemical analysis of the samples after 3 months of exposure showed that their activity was due mainly to ^{60}Co and ^{51}Mn. The chemical composition of the deposit in % by weight was as follows: Fe = 89; Ni = 5; Cr = 1.6; Mn = 1.6; Si = 1; Cu = 1; Al = 0.6; Ca = 0.1; Mg = 0.1.

The samples of steel were decontaminated in small vessels equipped with a reflux condenser. The ratio between the surface area of the metal and the volume of solution (V/S) was maintained constant; the pH of the solution was corrected with ammonia. The results of the investigation reflecting the influence of the duration of treatment and the concentrations of $C_2O_4^{2-}$ and H^+ ions on the effectiveness of the decontamination of stainless steel are given in Fig. 1. We can see that the effectiveness of the decontamination process increases with the concentration of oxalate ions and with the pH of the solution. However, the relationship of the decontamination coefficient (K_D) to time for samples with pH = 1 is quite different in character to those with pH = 2 or 3, where we observed a continuous increase of K_D over all the intervals of time studied, while a higher value of K_D was also obtained for larger concentrations of oxalate ions. The same relationship was observed up to 5 h with pH = 1. The relationship of K_D to time shows a clearly pronounced maximum, the fall after 10 h being steeper the higher the concentration of oxalate ions.

This sort of relationship is usually observed in cases where the process of decontamination is accompanied by sorption of radionuclides by the surface of the metal after the protective oxide film has been removed. This phenomenon is more characteristic of solutions of oxalic acid with concentrations of oxalate ions between 20 and 30 g/liter and occurs at a pH of 2.5-3.0 (Fig. 2).

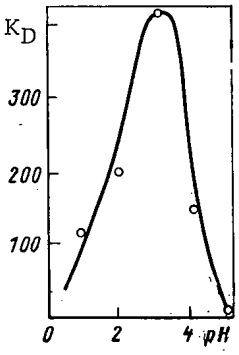

Fig. 2. Influence of solution pH on the effectiveness of the decontamination of stainless steel (samples from the VK-50 reactor) at 90°C for $H_2C_2O_4$ = 20 g/liter and a treatment time of 4 h.

The decontamination of carbon steel was investigated in a similar way. This showed that the hydrogen ion concentration and the duration of the operation affects the efficiency of the process to a lesser extent than is the case with stainless steel, while the absolute value of the decontamination coefficient is lower (Tables 1 and 2).

When the samples of carbon steel were inspected after unloading from the reactor, microflaws were observed on the surfaces of the majority of them. This gives us reason to suppose that the invasion of radionuclides when the steel was in contact with the coolant took place at a greater depth than was the case with stainless steel. It would appear that this was the main reason for the lower effectiveness of decontamination in carbon steel. We should also bear in mind that the decontamination of carbon steel is accompanied by the formation of quite a dense thinly dispersed deposit on the surface, which is basically an oxalate of ferrous iron. The surface layer of FeC_2O_4 protects the metal from corrosion and hinders the desorption of radionuclides from the surface of the metal.

With a significant concentration of Fe^{2+}, the formation of its oxalic acid salt can take place throughout the whole volume. In this connection, we studied the solubility of ferrous oxalate at 25 and 90°C and the various concentrations of $C_2O_4^{2-}$ and H^+ ions. The pH was corrected by means of ammonia. The solubility curve of FeC_2O_4 (Fig. 3) shows that the solubility of ferrous oxalate increases with an increase in pH and an increase in the $C_2O_4^{2-}$ ion concentration.

For a solution with an $H_2C_2O_4$ concentration of 20 g/liter, the yield of acid salts is determined by the value 0.223 M, while the pH, calculated by taking account of the dissociation constant of the $H_2C_2O_4$ and the activity coefficient of the salt and $C_2O_4^{2-}$ ions, equals 2.5 [11]. At lower degrees of neutralization, the pH < 2.5; at higher degrees of neutralization, the pH $\geqslant$ 2.5. We are able by calculation to estimate the approximate ionic composition of the solution of oxalic acid from the known value of pH. For example, a solution with a pH of 3 is buffered by a mixture of basic and acid salts.

Bearing this in mind, the increase in the solubility of the sediment of Fe(II) oxalate with increase in reagent concentration at constant pH can be explained by the increase in the capacity of the buffer solution and the concentration of $C_2O_4^{2-}$ ions, an excess of which forms a highly soluble complex compound [11-14]. The increase in the solubility of FeC_2O_4 with increase in pH at constant $C_2O_4^{2-}$ concentration (Fig. 4) probably results from an increase in the yield of hydrolyzed ions of iron, such as $FeOH^+$, which have a lower inclination to complex with oxalate ions. The minimum solubility of FeC_2O_4 in a solution containing 25.6 g/liter of ammonium oxalate at pH 3 and 90°C equals 0.2 g/liter. The solubility of FeC_2O_4 increases more rapidly than $H_2C_2O_4$, e.g., Trilon B, when a complexing agent is added.

A deactivation condition that excludes the formation of secondary deposits will naturally be the most efficient. When oxalic acid solutions are used, this can be achieved by adding hydrogen peroxide to the solution, which oxidizes the bivalant iron to trivalant iron, which does not form low-solubility compounds with oxalate ions.

Table 2 gives data on the effect that H_2O_2 has on the efficiency of deactivating steels. This is markedly reduced in the case of stainless steel, if H_2O_2 is present throughout the whole treatment time. However, the effectiveness is retained during the whole of the 12-15-h process in solutions with $H_2C_2O_4$ = 20 g/liter if the H_2O_2 is introduced into the solution 2-3 h prior to completion of the process. The presence of H_2O_2 in a concentration of 5 g/liter has practically no effect on the efficiency of the decontamination of carbon steel. As the temperature is increased from 60 to 90°C at pH 3 and $H_2C_2O_4$ = 20 g/liter, the decontamination coefficient increases by a factor of about 20 (from 5 to 105).

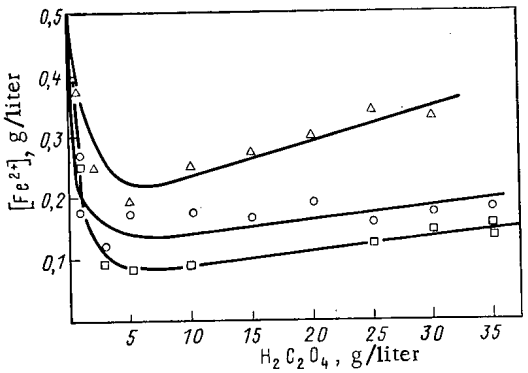

Fig. 3

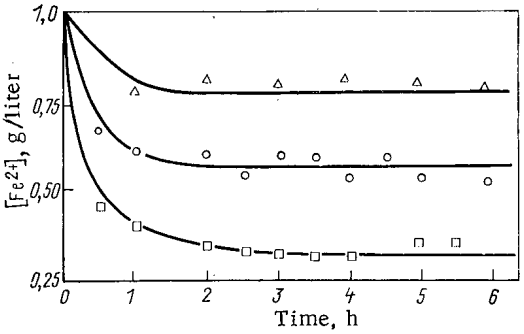

Fig. 4

Fig. 3. Solubility of Fe(II) oxalate at 25°C and $[Fe^{2+}]$ = 0.5 g/liter in relation to the concentration of $H_2C_2O_4$ and pH = 2 (□), 3 (○), and 4 (△).

Fig. 4. Speed of formation and solubility of Fe(II) oxalate in a solution of ammonia at 90°C $\varphi[Fe^{2+}]_{gen}$ = 1.0 g/liter and $H_2C_2O_4$ = 20 g/liter for pH = 4 (△), 3 (□), and 3 with the addition of 2 g/liter of Trilon B (○).

Discussion of Results. As we have seen already, the basic structural material of the coolant circuit of the RBMK-1000 reactor is stainless steel. It is this fact that has determined our lines of investigation. It has been shown that oxalic acid solutions are a sufficiently effective way of removing corrosion deposits from the surface of stainless steel. The decontamination effectiveness tends to increase with increase in the concentration of $H_2C_2O_4$ and the temperature. The hydrogen ion concentration in the solution also exerts an important influence on the process, the optimum effect being felt at pH ≈ 2.5.

It has been established that highly insoluble compounds of ferrous oxalate form on the surface of carbon steel at low values of pH in solutions of $H_2C_2O_4$. This is accompanied by a dangerous accumulation of FeC_2O_4 in stagnant zones under decontamination conditions, and leads to a reduced effectiveness of circuit decontamination. The solubility of FeC_2O_4, as we have shown, increases with increases in oxalate-ion concentration and the pH of the solution.

We can fully prevent the formation of FeC_2O_4 only by the introduction of hydrogen peroxide into the solution. The undoubted advantages of H_2O_2 as an oxidizing agent lie in the fact that, besides dissolving the FeC_2O_4, its introduction into the solution leads to a fall in the salt content, due to oxidation of the oxalic acid by the reaction $H_2C_2O_4 + H_2O_2 = 2CO_2\uparrow + 2H_2O$ with a gradual increase of the solution pH to 4-4.5 (from an initial value of pH 3, $H_2C_2O_4$ = 20 g/liter). The increase in pH has a positive influence on the concluding stages of decontamination, reducing the corrosion of carbon steel and increasing the solubility of FeC_2O_4.

The effectiveness of the method we have developed for decontaminating by oxalic acid solution has been proved under production conditions, indicating the possibility of using it for decontaminating of the main coolant circuit of the RBMK-1000 reactor.

LITERATURE CITED

1. A. M. Petros'yants et al., At. Energ., 31, No. 4, 333 (1971).
2. Corrosion of Structural Materials in Water-Cooled Reactors [Russian translation], Atomizdat, Moscow (1965), p. 330.
3. C. Bergen and I. Chupak, Ind. Eng. Chem., No. 8, 699 (1966).
4. R. Gasparini, in: Proc. Am. Power Conf., Chicago, 33, No. III, 776 (1971).
5. H. Ungler and D. Westfal, Decontamination of the Primary Coolant Circuit of an Investigated VVR-S in Rossendorf, Symposium on the Water Conditions of Water-Cooled-Water-Moderated Power Reactors in the German Democratic Republic, Gera, 10-16 November, 1968.
6. D. D. Legler et al., Proceedings of the Scientific and Technical Conference on Investigations into the Safe Disposal of Liquid, Solid, and Gaseous Effluents and the Decontamination of Contaminated Surfaces, Kolobzheg, Oct. 27, 1972, Vol. 2, p. 134.
7. I. Ayres, Decontamination of Nuclear Reactors and Equipments, Ronald Press, New York (1970).

8. R. Watkins, Energ. Nucl., 2, No. 99, 104 (1961).
9. S. Gibson, Can. Nucl. Technol., 2, No. 2, 50 (1963).
10. I. M. Plotnikov, T. V. Matskevich, and O. M. Ryazanov, Byull. Izobret., No. 3, 143 (1973) (USSR Patent No. 348118).
11. B. P. Nadeinskii, Theoretical Fundamentals and Calculations in Analytical Chemistry [in Russian], Vysshaya Shkola, Moscow (1959).
12. L. Kolthoff and R. Perlich, Phys. Chem., 46, 561 (1942).
13. V. F. Toropova, Zh. Obshch. Khim., 2, 1211 (1941).
14. J. Lingane, J. Am. Chem. Soc., 68, 2448 (1946).

FIRST-PASS NEUTRONS IN EQUATIONS FOR THE ALBEDO OF MEDIA

S. V. Voitovetskii and V. V. Orlov

UDC 621.039.51.12:539.125.52

Approximate equations for the albedo β of bodies of simple shapes were obtained in [1] with the assumption of the isotropy of the incident and reflected radiation. The calculations of [2] and comparisons with the quite exact calculations of Stuart [3], however, revealed a considerable error in Eqs. (1) for a cylinder with an optical thickness $R\Sigma \approx 1$, notwithstanding the satisfactory accuracy for small and large $R\Sigma$. Those papers also explain the probable cause of the discrepancy, i.e., consisting in the appreciable anisotropy of the angular distribution of neutrons which do not experience collisions. To take this into account we write the albedo of an infinite cylinder of radius R as the sum of β_0 (the probability of free flight of a neutron right through the cylinder) and β_1 (the probability of diffuse reflection which we assume to be isotropic):

$$\beta(R)=\beta_0(R)+\beta_1(R); \tag{1}$$

$$\beta_0(R)=\frac{\int\limits_{(n\Omega)>0}(\mathbf{n}\Omega)\exp[-l(\Omega)]\,d\Omega}{\int\limits_{(\mathbf{n}\Omega)>0}(\mathbf{n}\Omega)\,d\Omega}. \tag{2}$$

Here $\mathbf{n}$ is the normal to the surface of the rod, Ω is the direction of neutron flight, and $l(\Omega)$ is the optical path of the neutron in the cylinder. Following the principle of Ambartsumyan [4], we isolate interactions in a thin layer Δ near the surface of the cylinder. With isotropic incidence of neutrons on this layer the probability of collision is $2\Delta\Sigma$. For unscattered neutrons which passed right through the cylinder this probability is

TABLE 1. Results of Numerical Solution of Eq. (7)

$H=\Sigma_s/\Sigma$	$R=0{,}17$ cm			$R=0{,}25$ cm			$R=0{,}50$ cm		
	exact value [4]	ref. [2]	Eq. (7)	exact value [4]	ref. [2]	Eq. (7)	exact value [4]	ref. [2]	Eq. (7)
0,0	0,726	0,730	0,722	0,623	0,632	0,623	0,404	0,432	0,404
0,2	0,773	0,775	0,768	0,683	0,689	0,682	0,482	0,504	0,479
0,4	0,823	0,825	0,819	0,749	0,753	0,748	0,574	0,590	0,570
0,6	0,877	0,878	0,874	0,823	0,825	0,822	0,686	0,695	0,681
0,8	0,936	0,936	0,938	0,906	0,907	0,905	0,824	0,827	0,821
$H=\Sigma_s/\Sigma$	$R=1{,}00$ cm			$R=1{,}50$ cm			$R=2{,}00$ cm		
	exact value (7)	ref. [2]	Eq. (7)	exact value [4]	ref. [2]	Eq. (7)	exact value [4]	ref. [2]	Eq. (7)
0,0	0,186	0,245	0,186	0,095	0,166	0,095	0,053	0,125	0,053
0,2	0,263	0,317	0,261	0,165	0,233	0,164	0,115	0,179	0,117
0,4	0,363	0,407	0,357	0,256	0,319	0,254	0,199	0,270	0,202
0,6	0,499	0,529	0,488	0,389	0,437	0,379	0,324	0,386	0,322
0,8									

Translated from Atomnaya Énergiya, Vol. 49, No. 3, pp. 186-187, September, 1980. Original article submitted July 23, 1980.

0038-531X/80/4903-0641$07.50

TABLE 2. Nonmultiplying Uniform Slug with R = 1.2 cm, $\Sigma_{t_1} = 0.25$ cm^{-1}, $\Sigma_{t_2} = 1.5$ cm^{-1}, $\Sigma_{s_{11}} = 0.12$ cm^{-1}, $\Sigma_{s_{12}} = 0.03$ cm^{-1}, $\Sigma_{s_{21}} = 0$ cm^{-1}, $\Sigma_{s_{22}} = 0.5$ cm^{-1}.

β_{11}		β_{12}		β_{22}	
Monte Carlo method	Eq. (8)	Monte Carlo method	Eq. (8)	Monte Carlo method	Eq. (8)
0,7423± ±0,0045	0,7386	0,0189± ±0,0015	0,0192	0,1913± ±0,0039	0,1880

TABLE 3. Multiplying Uniform Slug with R = 1.2 cm, $\Sigma_{t_1} = 0.25$ cm^{-1}, $\Sigma_{t_2} = 1.5$ cm^{-1}, $\Sigma_{s_{11}} = 0.22$ cm^{-1}, $\Sigma_{s_{12}} = 0.03$ cm^{-1}, $\Sigma_{s_{21}} = 1.0$ cm^{-1}, $\Sigma_{s_{22}} = 0.5$ cm^{-1}

β_{11}		β_{12}		β_{21}		β_{22}	
Monte Carlo method	Eq. (8)	Monte Carlo method	Eq. (8)	Monte Carlo method	Eq. (8)	Monte Carlo method	Eq. (8)
0,9748±0,009	0,9788 (0,9784)	0,0237±0,0022	0,02284 (0,02283)	0,7900±0,007	0,7813 (0,7811)	0,2037±0,005	0,1987 (0,1986)

$$2k\Delta\Sigma = \frac{\int\limits_{(n\Omega)>0} \exp[-l(\Omega)]\, d\Omega}{\int\limits_{(n\Omega)>0} (\mathbf{n}\cdot\Omega)\exp[-l(\Omega)]\, d\Omega}\,\Delta\Sigma > 2\Delta\Sigma. \tag{3}$$

From the relation

$$\beta_0(R+\Delta) \approx \beta_0(R) + \frac{\partial\beta_0}{\partial R}\Delta = (1-2k\Delta\Sigma)\,\beta_0(R)\left(1-2k\Delta\Sigma-\frac{\Delta}{R}\right)+\frac{\Delta}{R} \tag{4}$$

as $\Delta \to 0$ we get

$$k = \frac{1}{4\Sigma}\left(-\frac{1}{\beta_0}\frac{\partial\beta_0}{\partial R}+\frac{1-\beta_0}{R}\right). \tag{5}$$

We also make allowance for the fact that the angular distribution of neutrons scattered in the layer $\Delta \to 0$, not isotropically but in proportion to $1/(\mathbf{n}\Omega)$, so that the probability of free flight of the neutrons right through the cylinder is different from β_0 and is equal to

$$\tilde{\beta}_0 = \frac{\int\limits_{(n\Omega)>0} \exp[-l(\Omega)]\, d\Omega}{\int\limits_{(n\Omega)>0} d\Omega}. \tag{6}$$

As a result, for $\beta_1(R)$ we get the equation

$$\frac{\partial\beta_1}{\partial R} = \Sigma_s - \frac{\beta_1}{R} - 2\beta_1(2\Sigma-\Sigma_s)+\Sigma_s(\beta_1+k\beta_0)^2+2\Sigma_s k\beta_0 \tag{7}$$

with the boundary condition $\beta_1(0) = 0$.

In the many-group representation

$$\frac{\partial\hat{\beta}_1}{\partial R} = \hat{\Sigma}_s+\hat{\Sigma}_s\hat{\beta}_1+\hat{\beta}_1\hat{\Sigma}_s+\hat{\Sigma}_s(\beta_0 k)-\frac{\hat{\beta}_1}{R}-2\Sigma_i\hat{\beta}_1-$$

$$-2\hat{\beta}_1\Sigma_k+\hat{\beta}_1\hat{\Sigma}_s\hat{\beta}_1+\hat{\beta}_1\hat{\Sigma}_s(\beta_0 k)_k+(\beta_0 k)_i\hat{\Sigma}_s+(\beta_0 k)_i\hat{\Sigma}_s\hat{\beta}_1+(\beta_0 k)_i\hat{\Sigma}_s(\beta_0 k)_k; \tag{8}$$

$$\beta_{0i} = \frac{\int\limits_{(n\Omega)>0} \exp[-\Sigma_i l(\Omega)]\,(\mathbf{n}\Omega)\, d\Omega}{\int\limits_{(n\Omega)>0} (\mathbf{n}\cdot\Omega)\, d\Omega};$$

$$(\beta_0 k_i) = \frac{1}{\Sigma_i}\left(-\frac{\partial\beta_{0i}}{\partial R}+\frac{1-\beta_{0i}}{R}\right). \tag{9}$$

The equations are written in matrix form, where β_{1ik} is the probability that, after entering the cylinder with an energy of group i, a neutron will emerge from the cylinder with an energy of group k. Let us note that (β_{ok}) and β_{oi} depend only on $\Sigma_i R$ and they can thus be tabulated and used in further calculations. For a sphere, the quantity 1/R in Eqs. (7) and (8) is replaced by 2/R and k_{cyl} by k_{sph}. In the equations for plane layer we have $1/R \to 0$ and $\beta_o = 0$. Table 1 gives the results of numerical solution of Eq. (7) for a uniform cylinder while Tables 2 and 3 give the results of two-group calculation of nonmultiplying and multiplying uniform cylindrical slugs. In Table 3, the values in parentheses are those of the albedo obtained by considering the given slug as a two-layer system consisting of a slug of radius 1.02 cm and a layer of thickness 0.18 cm. For comparison, Table 3 also gives the results of calculations by the Monte Carlo method. We studied the solutions of the equation for the albedo of the medium outside the cylinder and the sphere:

$$\frac{\partial\beta}{\partial R} = 4\beta - H(1-\beta)^2 - \frac{\alpha\beta}{R}(1-\beta). \qquad (10)$$

With the condition that $\beta_{R\to\infty} = \beta_\infty$ — the albedo of the half-space and $H = \Sigma_s/\Sigma$, α is equal to 0 for the plane case, 1 for the cylindrical case, and 2 for the spherical case. In the limit for nonabsorbing media (H = 1) Eq. (10) has one solution $\beta_{cyl} = 1$ for the cylinder, and two solutions $\beta_{sph_1} = 1$ and $\beta_{sph_2} = R/(1 + R)$ for the sphere. The appearance of two solutions in the latter case can be understood by considering a finite spherical nonabsorbing layer Δ. If the condition of total reflection exists on its outer surface, then $\beta = 1$ and remains the same as $\Delta \to \infty$. If total reflection does not occur on the outer surface, then part of the neutrons move off to infinity and $\beta(R) < 1$. In the cylindrical (as well as in the plane) case the neutron current through a cylindrical surface with a large radius ρ tends to 0 as $\rho \to \infty$ so that the boundary conditions at the remote surface do not affect the albedo and $\beta \equiv 1$. The validity of these assertions is easily verified by solving the respective equations in the diffusion approximation. We carried out calculations of Eq. (10) for $H \neq 1$. It was expected that the absence of unscattered neutrons in the reflected flux in this case ensures adequate accuracy of Eq. (10). Comparison with the results of [5] for R = 1 and H = 0.8, however, revealed substantial discrepancies which require further analysis.

LITERATURE CITED

1. V. V. Orlov, At. Énerg., 38, No. 1, 39 (1975).
2. V. V. Orlov and V. S. Shulepin, At. Energ., 41, No. 6, 434 (1976).
3. G. Stuart, Vopr. Yad. Énerg., No. 6, 71 (1958).
4. V. A. Ambartsumyan, Theoretical Astrophysics [in Russian], Gostekhizdat, Moscow (1953).
5. A. Kavenoky, Nucl. Sci. Eng., 65, 209 (1978).

SPECTRAL AND ANGULAR CHARACTERISTICS OF THE PROTON COMPONENT OF THE FIELD OF RADIATION BEYOND THE SHIELDING OF A SYNCHROTRON AT ENERGY 660 MeV

V. E. Aleinikov, M. M. Komochkov, A. R. Krylov,
G. N. Timoshenko, and G. Khan

UDC 539.125.4.164

Reference [1] studied the angular distribution of the flux of protons beyond the concrete shielding of the supercyclotron laboratory of nuclear studies at the JINR. The next step in studying the proton component of the radiation field beyond the shielding of this accelerator is to measure the spectral and angular distribution of protons with energy greater than 40 MeV, which we have carried out for two variants of the experimental geometry.

The goal of this work, as in [1], is to obtain the primary experimental data for checking the methods of calculating various parameters of the radiation field beyond the shielding of an accelerator.

In the first variant of the experimental geometry (Fig. 1), a collimated beam of 630-MeV protons impinged on a concrete shield of thickness 2 m (470 g/cm^2) at an angle of 30°. In the second variant, the primary beam of protons was fully stopped in a copper target with a diameter of 12 cm and a thickness of 30 cm, placed 4.8 m from the target in the direction of

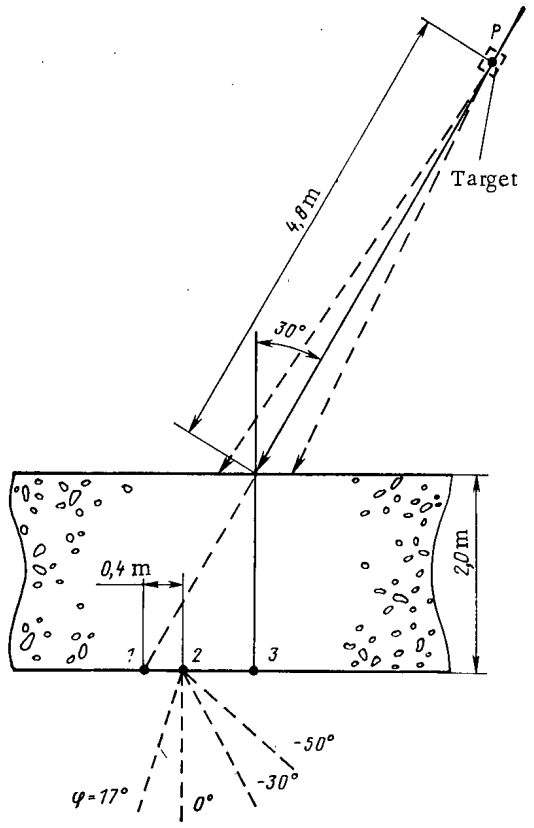

Fig. 1. Geometry of the measurements.

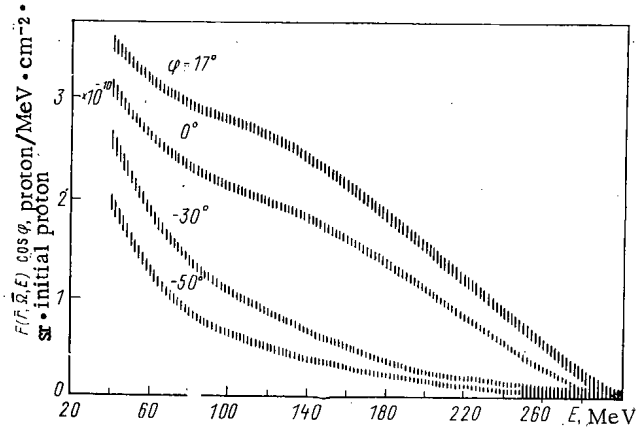

Fig. 2. Proton spectra at point 2, measured in the first variant of the experimental geometry.

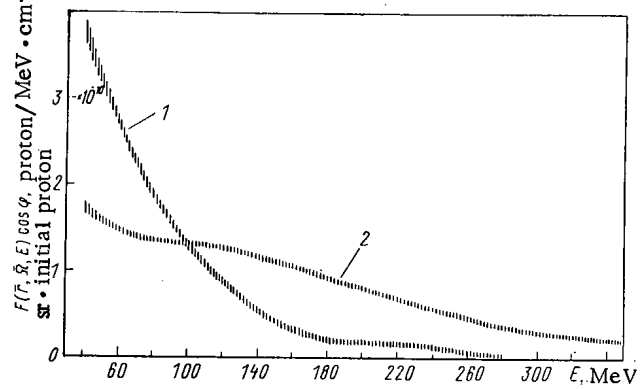

Fig. 3. Proton spectra at points 1 and 3, measured in the first variant of the experimental geometry: 1) point 3, φ = 0°; 2) point 1, φ = 30°.

Translated from Atomnaya Énergiya, Vol. 49, No. 3, pp. 188-189, September, 1980. Original article submitted September 28, 1979.

0038-531X/80/4903-0644$07.50

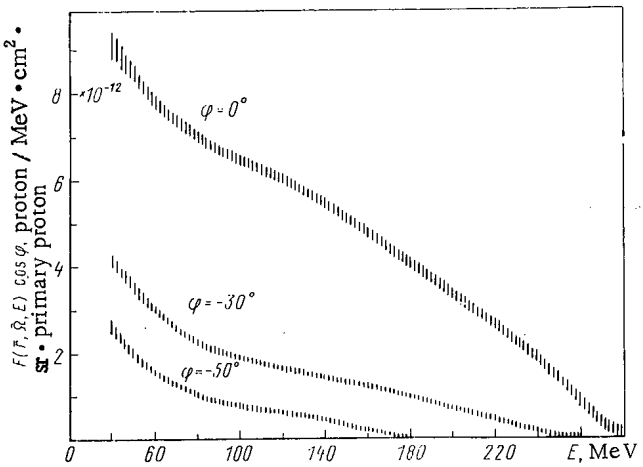

Fig. 4. Proton spectra at point 2, measured in the second variant of the experimental geometry.

the beam, which served practically as a plane monodirectional source of the radiation incident on the shield [2]. The proton spectra were measured by a ΔE spectrometer. The protons exited the shield at points 1, 2, and 3 at various angles φ to the normal in the horizontalplane. The physical angle and angular acceptance of the spectrometer for measurements in the first and second variants were, respectively, $19.5 \cdot 10^{-3}$ sr, 4.5°, and $33.3 \cdot 10^{-3}$ sr, 12.1°. The initial construction of the spectrometer and the method of reconstruction of the proton spectra from the experimental data were described in [3, 4]. The evaluation of the fractions of electron and π-meson components of the total charged particle flux was accomplished as in [1]. To determine the error in the measurements, the statistical error in the analyzer channels and the apparatus error were calculated. Figure 2 shows the dependence of the proton spectra measured in the first variant of the geometry at point 2 at angle φ. The ordinate is the differential angle and energy proton flux, $F(\mathbf{r}, \Omega, E)$, for energies from E_{min} and E_{max} at point $\mathbf{r}$ on the surface of the shield, multiplied by $\cos\varphi$ and normalized per primary proton [1]. Here Ω is the direction of motion of the proton detected by the spectrometer. The hardest of the spectra shown is that measured at $\varphi = 17°$, at the maximum of the angular distribution of the proton flux at the given point. The proton spectra at points 1 and 3, measured, respectively, at $\psi = 30$ and 0° in the first variant of the experimental geometry, are shown in Fig. 3. The spectrum at point 1, measured in the direction of the incident protons, is the hardest of all those obtained. On the other hand, the spectrum at point 3 is essentially softer than that at point 2, measured at $\varphi = 0$. Figure 4 shows the proton spectra measured at point 2 in the second variant of the experimental geometry.

In conclusion, we note that to analyze the systematics of the radiation spectra beyond the shielding of accelerators, it is necessary to further accumulate data for various experimental geometries and various sources of primary radiation, particularly for a higher energy of the accelerated protons.

The authors wish to thank A. N. Resunik and V. A. Kulikov for help in carrying out these experiments.

LITERATURE CITED

1. V. E. Aleinikov et al., JINR Preprint P16-11891, Dubna (1978).
2. V. E. Aleinikov et al., JINR Preprint P16-8179, Dubna (1974).
3. V. E. Aleinikov et al., JINR Preprint P16-94006, Dubna (1975).
4. G. N. Timoshenko et al., Kernenergie, 21, 181 (1978).

SLOW-NEUTRON DISTRIBUTION IN POLYCRYSTALLINE AND SINGLE-CRYSTAL SILICON SAMPLES

O. N. Efimovich, S. P. Solov'ev, E. S. Stariznyi,
A. A. Stuk, V. V. Sumin, and V. A. Kharchenko

UDC 621.315.592

At present the method of nuclear transmutations [1] is being more and more widely used to produce semiconductor silicon. This method permits quite accurate control of the phosphorus impurity introduced in the reaction $^{30}Si(n,\gamma)^{31}Si \rightarrow {}^{31}P$. The material obtained in this way is much more uniform than that produced by conventional doping methods [2]. This is very important in the manufacture of semiconductor devices.

With increasing size of the crystals being doped the uniformity of the distribution of the impurity introduced is decreased as a result of the self-shielding of the neutron flux by the sample. Therefore, in the practical application of the nuclear transmutations method it is necessary to know and to take account of the slow-neutron flux density distribution in the silicon samples. This problem is becoming very urgent in view of the trend toward the use of larger and larger silicon single crystals in the manufacture of semiconductor devices.

The slow-neutron flux density distribution in a sample can be determined by knowing the total interaction cross section and its components – the absorption and scattering cross sections. For materials in which the scattering cross section is larger than the absorption cross section the analysis of the distribution also necessitates taking account of the state of the crystal structure and the temperature of the bombarded sample. However, there are practically no such data in the literature for silicon single crystals.

In the present article we present measured values of the total interaction cross section of neutrons with silicon nuclei as a function of the neutron energy and the temperature and crystal structure of the sample. The attenuation of the neutron flux in silicon samples of various sizes was investigated also.

The experimental arrangement was described in [3]. The intensities of the slow-neutron beam incident upon and transmitted through the sample were measured as functions of energy. The interaction cross section was found from the relation

$$I/I_0 = \exp(-N\sigma x), \quad (1)$$

where I_0 and I are, respectively, the intensities of the incident and transmitted neutron beams; N, number of silicon nuclei per unit volume; σ, interaction cross section; and x, length of the sample.

In the neutron energy range investigated the change in flux density in the polycrystalline samples is independent of energy, as might be expected. In the single-crystal samples the attenuation depends on the neutron energy. The attenuation the maximum at ∿0.4 eV and

TABLE 1. Nuclear-Physical Characteristics of Polycrystalline and Single-Crystal Silicon

Neutron energy, eV	Single-crystal silicon, T = 300°K			Polycrystalline silicon, T = 300°C		
	σ_t, b	σ_a, b	σ_s, b	λ_{tr}, cm	σ_t, b	λ_{tr}, cm
0,4	1,68±0,08	0,04	1,64±0,08	11,9	2,25	11
0,054	0,54±0,02	0,11	0,43±0,02	37,0		
0,0256	0,42±0,02	0,16	0,26±0,02	47,6		
0,016	0,40±0,02	0,20	0,20±0,02	47,7		

Translated from Atomnaya Énergiya, Vol. 49, No. 3, pp. 189-191, September, 1980. Original article submitted November 12, 1979; revision submitted February 18, 1980.

 0038-531X/80/4903-0646$07.50

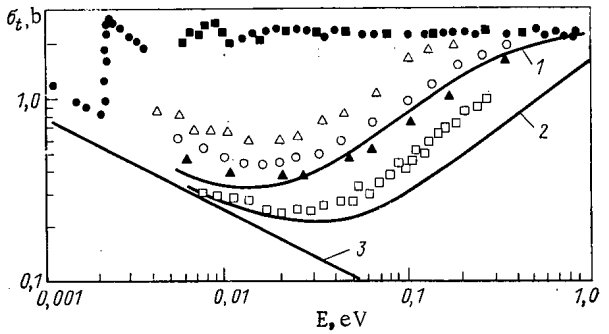

Fig. 1

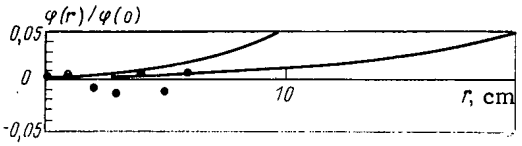

Fig. 2

Fig. 1. Energy dependence of total cross section in polycrystalline and single-crystal silicon samples at temperatures of 700 (Δ), 500 (○), 300 (▲), and 80°K (□); ■) experimental data for polycrystalline silicon; ●) data from [4]; 1, 2) calculated in [8] for single-crystal samples; 3) σ_a as a function of neutron energy [8]. The dimensions of the symbols correspond to the statistical errors of the measurements.

Fig. 2. Relative radial neutron flux density distribution in (1) polycrystalline and (2) single-crystal silicon samples; ●) experiment; ——) calculation.

above, and decreases markedly with decreasing neutron energy.

It should be noted that the attenuation of the neutron flux in our experiment was determined mainly by scattering processes, in the first place because $\sigma_a \ll \sigma_s$ for silicon, and secondly because the geometry of the experiment was such that a single scatter of a neutron was sufficient to prevent its being recorded by the detector. Thus, the experimental data yield the value of the transport length λ_{tr}, which for silicon is close to the scattering length λ_s. The actual data are shown in Table 1.

Figure 1 shows the energy dependence of the total cross section σ_t for polycrystalline and single-crystal silicon. For a polycrystal σ_t is practically independent of energy, and is in satisfactory agreement with the known data [4]. For single crystals the situation is different. For neutron energies $\geqslant 0.4$ eV σ_t is the same as for a polycrystal. With a decrease in neutron energy σ_t decreases from 2 to 0.45 b (1 b = 10^{-28} m^2). The calculated values of σ_t, σ_s, and σ_a for polycrystalline and single-crystal silicon are summarized in Table 1. In the calculations it was assumed that σ_a varies with neutron energy as $E^{-1/2}$. The absolute value of σ_a was taken equal to 0.16 b at E = 0.025 eV [8].

The difference in the energy dependence of σ_t in polycrystals and single crystals results from the difference in scattering processes. Taking account of coherent and incoherent elastic scattering and the fact that $\sigma_s \gg \sigma_a$ in silicon suggests that in a polycrystal effects due to neutron diffraction predominate in the energy range investigated. This assumption is rather well confirmed by the energy dependence of σ_t.

In a single crystal, on the other hand, the neutron flux is attenuated mainly as a result of inelastic scattering. Elastic coherent scattering makes only a small contribution to the total attenuation, since in oriented single crystals in the geometry of the present experiment the conditions for Bragg reflection are satisfied for only specific groups of neutrons. The values of the diffusion length for a polycrystal calculated from the tabulated data are in satisfactory agreement with published data (L = 22 cm [4]), but differ appreciably from our value L = 44 cm for a single crystal.

The calculated values of L were used to find the slow-neutron flux density distribution in cylindrical samples along the z axis, which coincides with the direction of the generators of the cylindrical sample, and along the radius of a two-region cylindrical cell composed of the silicon sample and water. In the first case the calculation was performed by the formula [5]

$$\varphi(0, z) = \sum_{n=1}^{\infty} \frac{2\varphi_0}{j_n J_1(j_n)} \frac{sh[\gamma_n (H - z)]}{sh(\gamma_n H)}, \qquad (2)$$

where $\gamma_n = (j_n/R)^2 + 1/L^2$, J_1, first-order Bessel function of the first kind; j_n, n-th root

of the zero-order Bessel function of the first kind φ_0, slow-neutron flux level at the end of the sample; H and R, extrapolated length and radius of the sample [5]; and L, slow-neutron diffusion length. The calculated values of the attenuation of the flux density in polycrystalline and single-crystal samples are in satisfactory agreement with the measured attenuation of the neutron flux as a function of the length of the samples investigated.

The radial distribution of the flux density can be found in the P_1-approximation from the relation [6]

$$\frac{\varphi(r)}{\varphi(0)}=\frac{AI_0\left(\frac{r}{L}\right)\Sigma_c+\xi\Sigma_s}{A\Sigma_c+\xi\Sigma_s}, \quad (3)$$

where A is a coefficient determined from the boundary conditions; Σ_c, macroscopic cross section for the capture of thermal neutrons by the material of the sample; $\xi\Sigma_s$, slowing down power of the sample material; and I_0, zero-order Bessel function of imaginary argument.

Equation (3) can be considerably simplified. To do this we expand the function $I_0(r/L)$ in a series and retain only the first two terms, since $r/L \ll 1$ for the actual silicon samples. Taking account also of the fact that $\xi\Sigma_s/\Sigma_c \approx 0.1$, we obtain finally an expression of the form given in [7]:

$$\frac{\varphi(r)}{\varphi(0)}\approx 1+\frac{r^2}{4L^2}. \quad (4)$$

The character of the radial flux density distribution in polycrystalline and single-crystal samples is shown in Fig. 2. From this follows the very important conclusion for practical doping that in the slow-neutron bombardment of single-crystal samples of silicon with diameters up to 200 mm, the attenuation of the neutron flux can be neglected [$\varphi(r)/\varphi(0) \leqslant 1\%$], while the attenuation of the neutron flux by a polycrystalline sample can be as much as 5%. It should be noted that these values can depend on the temperature of the samples bombarded. This results from the fact that σ_s, which is a component of σ_t, depends on the temperature, and L in turn depends on σ_t. Figure 1 shows the dependence of σ_t on neutron energy for various temperatures of the same sample. The character of the σ_t energy dependence remains practically the same, but the absolute values of the total cross section are quite different.

LITERATURE CITED

1. Neutron Transmutation Doping in Semiconductors, Proc. Second Int. Conf., Univ. of Missouri, April 25-26, 1978, Plenum Press, New York (1979).
2. V. A. Kharchenko and S. P. Solov'ev, Izv. Akad. Nauk SSSR, Ser. Neorg. Mater., 7, No. 12, 2137 (1971).
3. V. É. Komarov, O. L. Kukhto, and S. P. Solov'ev, Prib. Tekh. Eksp., No. 4, 29 (1970).
4. I. V. Gordeev, D. A. Kardashev, and A. V. Malyshev, Nuclear-Physics Constants [in Russian], Gosatomizdat, Moscow (1963).
5. S. Glasstone and M. Edlund, The Elements of Nuclear Reactor Theory, Van Nostrand, New York (1952).
6. I. A. Stenbok (editor), Physics of Nuclear Reactors [Russian translation], Atomizdat, Moscow (1964).
7. H. Janus and O. Malmros, IEEE Trans. Electron Devices, ED-23, 797 (1976).
8. R. Brugger and W. Yelon, in: Proc. Conf. on Neutron Scattering, Vol. 11, Gatlinburg, June 6-10 (1967), p. 1117.

MUTUAL INFLUENCE OF HOT-LOOP CHANNELS IN WATER REFLECTOR

N. I. Rybkin, E. S. Stariznyi,
R. B. Novgorodtsev, and V. V. Tishchenko

UDC 621.039.553:621.039.573

The working medium of hot loops (HL) as a rule contains good thermal-neutron absorbers. Thus, ^{115}In, which is the main component of indium–gallium and indium–gallium–tin alloys, has a microscopic cross section of ∿190 b (1 b = 10^{-28} m^2) for thermal-neutron absorption. The activity generators (AG) of such HL, therefore, strongly perturb the field of thermal neutrons.

Methods of calculating perturbations introduced by absorbing bodies of classical geometry (sphere, cylinder, plane) were considered in [1]. Real AG constructions are implemented, as a rule, in the form of multichannel assemblies, the calculations for which are involved because of the consideration of the mutual influence of the channels; this does not always ensure the required accuracy in the determination of radiation, technological, and economic parameters in the process of designing a facility with HP.

Accordingly, in the HL designing process multilayer AG were simulated experimentally [2, 3], which made it possible to obtain a high γ-ray power in irradiators with an insignificant expenditure of working medium. Experience gained in the construction and long operation of a series of HL in nuclear research reactor facilities demonstrated the technical and economic feasibility of HL in atomic power plants with reactors of the VVÉR and RBMK types [4].

The activity generators of HL in atomic power plants should be located in the reflector so that their effect on the reactivity of the reactor would be minimum. Design studies showed that technologically the most appropriate are tubular channels forming bunches or grids of rods since in this case the working medium, in essence, forms an absorbing rod (such channels will be called rod channels). The search for ways to increase the γ-ray power in the irradiator of HL in facilities with channel-type nuclear reactors led to the construction of AG in the form of coaxial cylindrical layers of working medium alternating with layers of water. Execution of such AG does not entail any major technical difficulties (the working substance moves in the gap between two coaxial tubes). It is therefore of great interest to have information about the mutual influence of AG channels in a moderator, especially in water which is the reflector and coolant in VVÉR reactors and the moderator in the AG of hot loops of RBMK reactors.

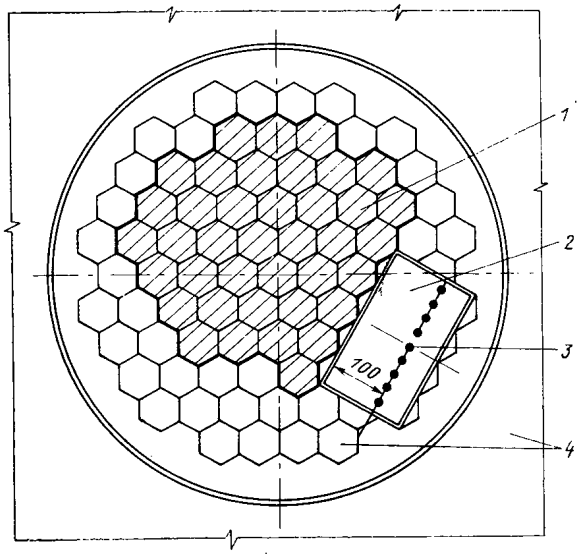

Fig. 1. Diagram of arrangement of rod channels of AG in water chamber of critical stand: 1) core; 2) water chamber; 3) grid of rod channels of AG; 4) water reflector.

Translated from Atomnaya Énergiya, Vol. 49, No. 3, pp. 191-193, September, 1980. Original article submitted November 27, 1979; revision submitted February 29, 1980.

0038-531X/80/4903-0649$07.50

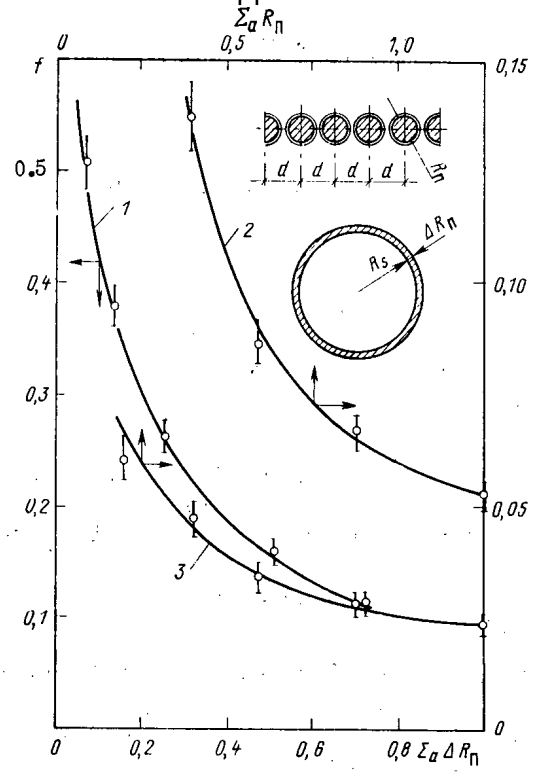

Fig. 2

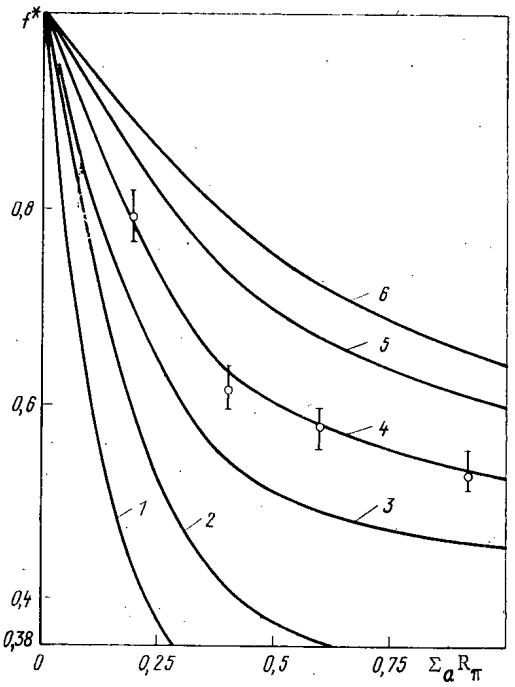

Fig. 3

Fig. 2. Coefficients $f = f(\Sigma_a, \Delta R_т, {}_a R_т)$, taking account of the self-screening of the density of thermal-neutron flux by: 1) a hollow cylinder; 2) a rod channel; 3) a grid of rods with a pitch of $(2R_т + 0.2)$ cm.

Fig. 3. Dependence of f_i^* of grid of rod channels of AG on $\Sigma_a R_т$ and $\Sigma_{sd} = 1.72$ (curve 1), 3.45 (curve 2), 5.17 (curve 3), 6.90 (curve 4), 8.62 (curve 5), and 10.35 (curve 6).

The present paper gives the results of experimental studies of the mutual influence of the channels of AG (forming either a grid of rods or one to three cylindrical layers of a working substance) in a water moderator. The mutual influence coefficient f_i^* for the i-th channel of an AG is construed to be the ratio of the mean activity $\bar{A}_i^*$ of the working medium in that channel to the mean activity $\bar{A}_i$ of the working medium in the same, but isolated, channel, i.e.,

$$f_i^* = \bar{A}_i^*/\bar{A}_i = \bar{\varphi}_i^*/\bar{\varphi}_i,$$

where $\bar{\varphi}_i^*$ and $\bar{\varphi}_i$ are the mean values of the thermal-neutron fluxes in the working substance in the i-th channel in the proximity of the other channels and in the isolated channel, respectively.

The experiments were conducted on a critical stand with the same kind of fertile medium as in the VVR-Ts reactor [5] and a water reflector. The rod channels were made of quartz tubes filled with indium–gallium alloy (inner radius $R_т$ = 1.5-10 mm, height 600 mm) and placed in a Plexiglas housing with a pitch of $\Sigma_s d$ = 0-1 (Σ_s is the macroscopic scattering cross section of the moderator and d is the distance between the rod axes).* The grid was assumed to be infinite if the peripheral rods had no influence on the rod under consideration, surrounded by the other rods of the grid.

The hollow cylindrical channels were made in the form of Plexiglas shells (wall thickness 1 mm, height 350 mm) between which was inserted indium foil with a thickness of $\Sigma_a \Delta R_т$ = 0.1-0.75 (Σ_a is a macroscopic cross section for thermal-neutron absorption and $\Delta R_т$ is the foil thickness).

*Here and in what follows we express the linear dimensions in terms of their products on the corresponding macroscopic sections.

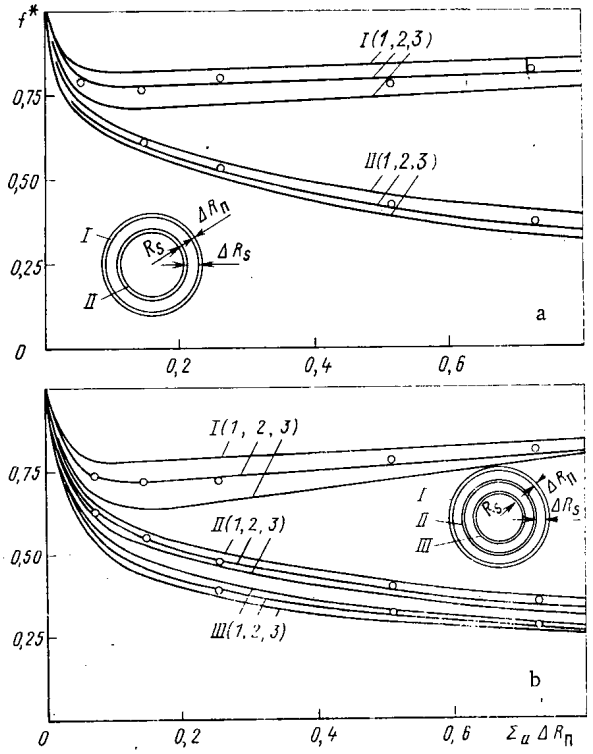

Fig. 4. Dependence of coefficients of mutual influence of two (a) and three (b) coaxial hollow cylindrical channels of AG on the thickness of the interlayers of absorber $\Sigma_a \Delta R_п$ and moderator $\Sigma_s \Delta R_s$ = 6.90 (curve 1), 3.45 (curve 2), and 1.72 (curve 3) for $\Sigma_s R_s$ = 6.

The irradiation was carried out in a special water chamber of 273 × 165 mm, situated in the reflector of the critical stand (Fig. 1), at a constant power for ∿30 min. The irradiation zone in all experiments was chosen with a predominance of thermal neutrons with a density of $\varphi_{oi} \approx 5 \cdot 10^7$ neutrons/cm^2·sec in the unperturbed flux ($R_{Cd} > 10$ with respect to indium when the cadmium can is 0.8 mm thick). Normalization to the power level of the critical stand was performed by using an indium monitor of constant mass, immersed at one and the same point of the reflector. The mean density of the thermal-neutron flux in indium-gallium alloy was found from the activity of a specimen taken after mixing the alloy in the volume of the channel while in indium foils it was found from the activity of indicators cut from the foil along their perimeter at mid-height of the cylinders. The mean unperturbed density φ_{oi} was found from the activity of the indium indicators of diameter 10 mm with an indium concentration ∿3 mg/cm^2, placed on a Plexiglas substrate, corresponding to the channel geometry as $\frac{1}{l}\int_l \varphi_{oi}\, dl$ (l is the channel length). The activity of the specimens and indicators were measured in a fixed geometry on a spectrometric apparatus with a plastic scintillator as a detecting element [6]. In this case the maximum error of measurement did not exceed 10%.

Figure 2 gives the experimental values of the coefficients, taking account of the self-screening and perturbation of the thermal-neutron flux density, $f_i = \varphi_i/\varphi_{oi}$, for a rod channel, one hollow cylinder, and a finite grid of rods with a pitch of $(2R_п + 0.2)$ cm. When the inner radius of the cavity in the cylinder is $6 \leqslant \Sigma_s R_s \leqslant 10$, then, as shown by measurements, the values of $f_i = f(\Sigma_a \Delta R_п)$ are practically independent of $\Sigma_s R_s$ (R_s is the inner radius of the hollow cylinder).

Figure 3 presents the values of the coefficients f_i^* of mutual influence for rod channels in an infinite grid as a function of their pitch and radius while Fig. 4 gives the values of f_i^* for two or three hollow coaxial cylinders as a function of the thickness of the absorbing layers and interlayers of moderator between them.

The results obtained are useful not only for calculating and optimizing activation generators of hot loops with nonfissionable materials but also for working out other experimental devices with the given geometry.

The authors express their gratitude to I. T. Gavrilenko, V. P. Savina, and N. I. Goncharov for their assistance in preparing and performing the experiments on the critical stand.

LITERATURE CITED

1. V. A. Zharkov, T. P. Zorina, and G. M. Fradkin, At. Energ., 24, No. 4, 369 (1968).
2. E. S. Sakharov and I. P. Chuchalin, At. Energ., 35, No. 6, 432 (1973).
3. G. I. Kiknadze et al., At. Energ., 31, No. 2, 113 (1971).
4. A. Kh. Breger, Radiation-Chemical Technology. Problems and Methods [in Russian], Atomizdat, Moscow (1979).
5. P. P. Moiseenko and V. L. Karpov, in: Proc. Second Geneva Conference. Papers of Soviet Scientists [in Russian], Vol. 6, Gosatomizdat, Moscow (1959).
6. M. A. Markina, E. S. Stariznyi, and A. Kh. Breger, At. Energ., 44, No. 6, 525 (1978).

DYNAMICS OF REACTORS WITH POSITIVE REACTIVITY FEEDBACK

E. F. Sabaev

UDC 621.039.514

As is known, that which passes into infinity in a finite time is called a solution of the explosive type. If such a solution exists in any arbitrarily small neighborhood of the equilibrium state, then the instability is called an explosive instability. In the present paper we consider the problem of the existence and estimates of solutions of the explosive type for any general model of reactor dynamics, including a description of the reactor kinetics, the reactivity feedback, and the reactor control or safety system.

The reactor dynamics in the one-point model of kinetics will be described by the following system of quite general form:

$$\begin{gathered} l\frac{dn}{dt}=n\left[\delta k_0(\sigma)+\mathbf{b}^{\mathrm{T}}\mathbf{x}\right]+\sum_{i=1}^{6}\beta_i(n_i-n);\\ dn_i/dt=\lambda_i(n-n_i),\ i=1,\ 2,\ \ldots\ 6;\\ d\mathbf{x}/dt=A\mathbf{x}+\mathbf{a}n;\\ d\sigma/dt=-V\ \mathrm{sign}\ (n-1). \end{gathered} \tag{1}$$

Here n and n_i are the relative neutron flux density and the concentration of sources of delayed neutrons; $\mathbf{x}$, a vector from R^N describing the state of the reactivity feedback; $\delta k_0(\sigma)$, reactivity introduced by the control rods; σ, position of the absorbing rods; V, rod velocity; A, a constant $N \times N$ matrix; $\mathbf{a}$ and $\mathbf{b}$, constant vectors from R^N; and $\delta k_0(\sigma)$, a nondecreasing bounded function.

For convenience in further study we introduce the equation

$$d\tau/dt=-r\tau+n,$$

where r is a constant. The solution for $r \neq 0$ is reduced to the case $r = 0$ by an appropriate change of variables. Accordingly, the discussion which follows will be for $r = 0$. In this case τ is proportional to the quantity of heat liberated in the time t.

In the space R^N we introduce a cone C, i.e., we write $x \in K$ (or $\mathbf{x} \geqslant 0$) if for all $t \geqslant 0$ the inequality

$$\mathbf{b}^{\mathrm{T}}\exp(At)\,\mathbf{x}\geqslant 0 \tag{2}$$

is satisfied.

Let us assume that C is a normal solid cone (see [1, 2] for the definition of a normal solid angle). Some limitations on the matrix A follow from this assumption. For example, if $\mathbf{b}$ is a vector with nonnegative components and A is a matrix with nonnegative off-diagonal elements, then inequality (2) defines a normal solid cone. If $a \in K$, then inequality (2) means that the reactivity response to a δ-like perturbation of the neutron flux is a positive function; it is natural to call such a feedback positive. Suppose that

Translated from Atomnaya Énergiya, Vol. 49, No. 3, pp. 193-195, September, 1980. Original article submitted February 6, 1980.

 0038-531X/80/4903-0652$07.50

where $-A\mathbf{a}^+ \in K$ and $-A\mathbf{a}^- \in K$. If $\det A \neq 0$, then such a representation is possible for any $\mathbf{a} \in R^N$ since AC is also a normal solid cone. If A is a Hurwitz matrix (spectrum A belongs to the left half plane), then $-A^{-1}$ is an operator which is positive with respect to cone C, i.e., puts an element from C in correspondence with an element from C. In this case the condition $-A\mathbf{a}^+ \in K$ implies that $\mathbf{a}^+ \in K$.

Further we assume that $\mathbf{x} = \mathbf{x}^+ + \mathbf{x}^-$ and examine the solution of the equations

$$\begin{aligned} d\mathbf{x}^+/d\tau &= A\mathbf{x}^+/n + \mathbf{a}^+; \\ d\mathbf{x}^-/d\tau &= A\mathbf{x}^-/n - \mathbf{a}^- \end{aligned} \tag{3}$$

with initial conditions from S^+ and S^-, respectively:

$$\begin{aligned} S^+ &= \{\mathbf{x}^+ \in R^N: -A\mathbf{x}^+ \in K\}; \\ S^- &= \{\mathbf{x}^- \in R^N: A\mathbf{x}^- \in K\}. \end{aligned}$$

In Eqs. (3) n is a positive continuous function of τ. Since $-A\mathbf{a}^+ \in K$ and $-A\mathbf{a}^- \in K$ we have $\mathbf{x}^+ \in S^+$ and $\mathbf{x}^- \in S^-$, provided that the above inclusion holds only for the initial instant. The proof follows from the monotonicity of the displacement operator over cone C for Eqs. (3). For example,

$$\frac{d}{\partial\tau} A\mathbf{x}^+ = \frac{1}{n} A(A\mathbf{x}^+) + A\mathbf{a}^+,$$

but $A\mathbf{a}^+ \leqslant 0$ and $A\mathbf{x}^+ \leqslant 0$ for $\tau = \tau_0$ and, therefore, $A\mathbf{x}^+ \leqslant 0$ for $\tau > \tau_0$.

Let $n(\tau)$ and $p(\tau)$ be some positive nondecreasing functions, let $dn/d\tau = p(\tau)$, and let A be a Hurwitz matrix. Then, for any $n \geqslant n(\tau)$ and all $\tau \geqslant \tau_0$ inequalities

$$\begin{aligned} \mathbf{x}^+ &\geqslant (pI - A)^{-1} \mathbf{a}^+ n(\tau), \\ \mathbf{x}^- &\geqslant -\mathbf{a}^- \tau \end{aligned}$$

are satisfied only if they are satisfied at the initial moment $\tau = \tau_0$. Indeed, suppose that $\mathbf{x}^+ = (pI - A)^{-1}\mathbf{a}^+ n(\tau) + \mathbf{z}$. Then

$$\frac{d\mathbf{z}}{d\tau} = \frac{A\mathbf{z}}{n} + (pI - A)^{-2} \mathbf{a}^+ n(\tau) \frac{dp}{d\tau} + (pI - A)^{-1}(-A\mathbf{a}^+) \frac{n - n(\tau)}{n} = \frac{A\mathbf{z}}{n} + Q,$$

where $\mathbf{z}(\tau_0) \in K$. Since $(A - pI)$ is a Hurwitz matrix, $(pI - A)^{-1}$ is a positive operator and, moreover, $[n - n(\tau)]/n \geqslant 0$, $dp/d\tau \geqslant 0$, $\mathbf{a}^+ \in K$, $-A\mathbf{a}^+ \in K$, whereby $Q \in K$. This and the positiveness of the displacement operator with respect to the trajectories imply that $\mathbf{z} \in K$, i.e., that the first inequality (for $\mathbf{x}^+$) holds. The second inequality is proved in similar fashion.

It follows from the definition of the cone C that $\mathbf{b}^T\mathbf{x} > 0$ on C and the inequalities proved above for $\mathbf{x}^+$ and $\mathbf{x}^-$ lead to the estimate

$$\mathbf{b}^T\mathbf{x} \geqslant \mathbf{b}^T(pI - A)^{-1}\mathbf{a}^+ n(\tau) - \mathbf{b}^T\mathbf{a}^-\tau. \tag{4}$$

Inequality (4) can be used to estimate n_i. In this case $R^N \equiv R^1$, $\mathbf{a}^+ = \lambda_i$, $\mathbf{a}^- = 0$, $A = -\lambda_i$, and $\mathbf{b} = \beta_i$ and, therefore,

$$\beta_i n_i \geqslant \frac{\beta_i \lambda_i}{p + \lambda_i} n(\tau), \quad i = 1, 2, \ldots 6. \tag{5}$$

Let us point out that the substitution $n_i = \frac{\lambda_i}{p + \lambda_i}(n + z_i)$ was used earlier (see [3, 4]) in solving the problem of bringing a reactor up to power from the subcritical state. Thus, inequality (4) can be considered as a generalization of estimates of the type of Eq. (5).

The estimates obtained make it possible to go over from the initial equations to differential inequalities [5-7]:

$$\begin{aligned} lp + \sum_{i=1}^{6} \beta_i \frac{p}{p + \lambda_i} &\geqslant \delta k_0(\sigma) + \mathbf{b}^T(pI - A)^{-1}\mathbf{a}^+ n - \mathbf{b}^T\mathbf{a}^-\tau; \\ dn/d\tau &= p; \quad d\sigma/d\tau = (V/n)\,\mathrm{sign}\,(n - 1). \end{aligned} \tag{6}$$

For $n \geqslant 1$, upon removing the inequality sign in Eq. (6) we arrive at a system of comparison in R^2 with a displacement operator along the trajectories which is monotonic over the cone $[0, \infty) \times (-\infty, 0]$. Any solution of these equations which satisfies the conditions $p \geqslant 0$,

$dp/d\tau \geqslant 0$, and $n(\tau) \geqslant 1$, yields the sought estimate of the solutions of the initial system. Estimates of the other variables are constructed with the aid of inequalities obtained in deriving Eqs. (6).

Let $\mathbf{b}^T\mathbf{a}^+ > \mathbf{b}^T\mathbf{a}^-$ and let s be some positive number satisfying the condition $s > s^*$; then $\mathbf{b}^T \times (pI - A)^{-1}\mathbf{a}^+ s^* = \mathbf{b}^T\mathbf{a}$. Assuming that $n = s\tau$ and bearing in mind that $\delta k_0(\sigma) \geqslant \delta k_0$, we can easily ascertain that the $p \geqslant s$ estimate is valid for all τ greater than some τ_0. With this estimate we find that the solutions of the comparison system and, therefore, of the initial system satisfy the inequality $n \geqslant s\tau$ for $\tau \geqslant \tau_0$. Since $d\tau/dt = n$, we have $\tau \geq \tau_0 \exp st$ and, therefore, $n \geq s\tau_0 \exp st$.

Thus, for $\mathbf{b}^T\mathbf{a}^+ > \mathbf{b}^T\mathbf{a}^-$ system (1) has solutions which go into infinity with an exponential growth factor greater than that preassigned. Such solutions lie in the region $p \geqslant s^*$, where $1/p$ is the reactor period.

We investigate to see whether or not this contains a set of solutions of the explosive type. First of all, let us note that if the estimate $n \geqslant (\tau/T)^{1+\gamma}$, $T > 0$, $\gamma > 0$, is valid, then all trajectories satisfying this estimate are of the explosive type. Indeed, from the inequality

$$d\tau/dt \geqslant (\tau/T)^{1+\gamma}, \quad \tau(0) = \tau_0$$

it follows that $\tau^\gamma \geqslant \tau_0^\gamma / \left[1 - \gamma \frac{t}{T}\left(\frac{\tau_0}{T}\right)^\gamma\right]$. The estimate means that n goes to infinity in a finite time.

Thus, it is necessary to verify the inequality $pT \geqslant (1 + \gamma)(\tau/T)^\gamma$ for all $\tau \geqslant \tau_0$; here, γ and τ_0 are numbers which we can choose as we see fit and $n = (\tau/T)^{1+\gamma}$.

Using the first equation of the comparison system, we reach the conclusion that if

$$\sigma k_0 + \mathbf{b}^T\left[\frac{1+\gamma}{T}\left(\frac{\tau}{T}\right)^\gamma I - A\right]^{-1}\mathbf{a}^+\left(\frac{\tau}{T}\right)^{1+\gamma} - \mathbf{b}^T\mathbf{a}^-\tau \geqslant \frac{l}{T}(1+\gamma)\left(\frac{\tau}{T}\right)^\gamma + \sum_{i=1}^{6}\beta_i \frac{(\tau'/T)^\gamma}{(\tau/T)^\gamma + \lambda_i T/(1+\gamma)} \tag{7}$$

for all $\tau \geqslant \tau_0$, then $pT \geqslant (1 + \gamma)(\tau/T)^\gamma$. Since $\mathbf{b}^T\mathbf{a}^+ > \mathbf{b}^T\mathbf{a}^-$, inequality (7) will be satisfied if we put the constraint $0 < \gamma \leqslant 1$ and $\mathbf{b}^T\mathbf{a}^+ > \mathbf{b}^T\mathbf{a}^-(1 + \gamma)$ on the choice of γ. Clearly, these inequalities can be satisfied by the choice of γ_1 and τ_0.

Example. Let us consider a reactor in respect of self-regulation, characterized by the following parameters: $N = 2$; $\lambda_0 > r$; $b_2 > b_1$

$$A = \begin{Vmatrix} -\lambda_0 & 0 \\ 0 & -r \end{Vmatrix}; \quad a^+ = \begin{Vmatrix} \lambda_0 \\ 0 \end{Vmatrix}; \quad a = \begin{Vmatrix} 0 \\ r \end{Vmatrix}; \quad b = \begin{Vmatrix} b_1 \\ b_2 \end{Vmatrix};$$

$$\lambda_0 b_1 > b_2 r.$$

The comparison equations for such a reactor are of the form

$$lp + \sum_{i=1}^{6}\beta_1 \frac{p}{p+\lambda_i} = b_1 \frac{\lambda_0}{p+\lambda_0} n - b_2 r\tau;$$

$$p = dn/d\tau; \quad d\tau/dt = n.$$

In the given case $s^* = \lambda_0 / \left(\frac{b_1\lambda_0}{b_2 r} - 1\right)$. The comparison system is conveniently studied over the phase plane (p, n). To this end it is necessary to eliminate the variable τ. Differentiating the first equation with respect to n, we have

$$\left[l + \Sigma\beta_i \frac{\lambda_i}{(p+\lambda_i)^2} + b_1 \frac{\lambda_0}{(p+\lambda_0)^2} n\right] \frac{dp}{dn} = \frac{b_1\lambda_0}{p+\lambda_0} - \frac{b_2 r}{p}.$$

From this system we establish that the half space $p > s^*$ is filled with trajectories of the explosive type. Indeed, for $p > s^*$ the variable p grows markedly with n and for large n and p the estimates $T_p > n^\gamma$ with $\gamma > 0$ is valid.

In the general case, including when allowance is made for the control and safety system of the reactor, the arrangement of the trajectories of the explosive type can be studied in greater detail by computer from the comparison equation.

Conclusions. The condition $\mathbf{b}^T\mathbf{a}^+ > \mathbf{b}^T\mathbf{a}^-$ means that the reactivity feedback transfer coefficient $K(p) = \mathbf{b}^T(pI - A)^{-1}\mathbf{a}$ is positive for sufficiently large positive real values of the

parameter p; such reactors can be called reactors with a predominant positive reactivity feedback at high frequencies. An important feature of the dynamics of such reactors is the existence of a system of trajectories of the explosive type in phase space.

LITERATURE CITED

1. M. A. Krasnosel'skii, Positive Solutions of Operator Equations [in Russian], Fizmatgiz, Moscow (1962).
2. M. G. Krein and M. A. Rutman, Usp. Mat. Nauk, 3, No. 1(23), 4 (1948).
3. D. L. Hetrick, Dynamics of Nuclear Reactors, Univ. of Chicago Press (1971).
4. H. Hurwitz, Nucleonics, 5(1), 61 (1949).
5. S. A. Chaplygin, Collected Works [in Russian], Vol. 1, Ob'ed. Gos. Izd., Moscow (1948).
6. N. V. Azbelov, Dokl. Akad. Nauk SSSR, 89, No. 4, 589 (1956).
7. M. A. Krasnosel'skii, Operator of Translation along Trajectories of Differential Equations, Amer. Math. Soc. (1968).

CROSS SECTIONS FOR (n, p) AND (n, α) REACTIONS ON CHROMIUM, IRON, COPPER, AND MOLYBDENUM NUCLEI AT A NEUTRON ENERGY OF 14.8 MeV

O. I. Artem'ev, I. V. Kazachevskii, V. N. Levkovskii, V. L. Poznyak, and V. F. Reutov

UDC 539.172.4

The cross sections for (n, p) and (n, α) reactions on Cr, Fe, Cu, and Mo nuclei have been measured in many works. The published data, however, are still incomplete and contradictory [1, 2]. Insofar as these elements enter into the composition of the proposed construction materials of a thermonuclear reactors, it would be useful to measure the cross sections of these reactions.

This work measured the cross sections for (n, p) and (n, α) reactions by an activation method using a semiconductor γ spectrometer. The cross sections were determined by comparing the intensity of the characteristic γ lines produced by the studied and standard reactions.

TABLE 1. Cross Sections for the (n, p) and (n, α) Reaction, mb*

Reactions	This work	Data [1, 2]
$^{52}Cr(n, p)^{52}V$	84±8	118±16; 105±10; 90±10; 83±6; 78±11; 74±10; 73±5
$^{53}Cr(n, p)^{53}V$	47±6	44±5; 44±7; 36±6
$^{54}Cr(n, p)^{54}V$	15±2	16±3; 15±2; 13,5±1,5
$^{54}Cr(n, \alpha)^{51}Ti$	9±2	12,5±1,3; 8±0,8; 7±1
$^{54}Fe(n, p)^{54}Mn$	310±30	382±13; 368±28; 333±67; 310±25; 300±20; 259±26; 254±23
$^{54}Fe(n, \alpha)^{51}Cr$	90±15	131±34; 109±10; 92±37; 90±10
$^{63}Cu(n, \alpha)^{60}Co$	41±8	36±2,5; 34±2,4; 34±4
$^{65}Cu(n, \alpha)^{62}Co$	5,7±0,6	14±10; 7,5±2
$^{65}Cu(n, \alpha)^{62m}Co$	8,0±1,6	1,9±0,6
$^{92}Mo(n, p)^{92m}Nb$	53±5	62±4; 60±15; 14,5
$^{92}Mo(n, \alpha)^{89}Zr$	19±2	25±15; 20±8; 19±1,5
$^{95}Mo(n, p)^{95}Nb$	40±5	—
$^{95}Mo(n, p)^{95m}Nb$	7±2	—
$^{96}Mo(n, p)^{96}Nb$	22±2	37±9; 21±7; 21±1,5; 16±3
$^{97}Mo(n, p)^{97}Nb$	17±2	110±20; 108±54; 68±14; 17,1±1,5; 15,9±1,3
$^{97}Mo(n, p)^{97m}Nb$	7,0±0,7	7,4±0,8
$^{98}Mo(n, p)^{98}Nb$	9±1	19±3; 9±2; 6,7±0,5; 4,1±0,5
$^{98}Mo(n, \alpha)^{95}Zr$	5±1	8,1±1,0
$^{100}Mo(n, \alpha)^{97}Zr$	2,5±0,3	14±6

*1 b = 10^{-28} m².

Translated from Atomnaya Énergiya, Vol. 49, No. 3, p. 195, September, 1980. Original article submitted December 17, 1979.

0038-531X/80/4903-0655$07.50

Copper (reactions $^{65}Cu(n, 2n)^{64}Cu$) and aluminum (reactions $^{27}Al(n, \alpha)^{24}Na$) foils were used as standards. Irradiation was conducted on the neutron generator at the Institute of Nuclear Physics of the Academy of Science Kazakstan, USSR [3]. Isotopically enriched targets were used to measure the cross sections of Cr and Mo. The determination of the cross sections of the Mo isotopes was complicated by a large γ background from the matrix and the presence of γ lines of similar energy (e.g., ^{99}Mo and ^{97}Zr have, respectively, 739 and 743 keV; ^{95}Zr and ^{95}Nb have 758 and 764 keV, respectively), in connection with this the products of the (n, p) and (n, α) reactions on Mo were chemically separated from the target by a somewhat modified method which is described in [4].

The measurements of the cross sections of the reactions (n, p) on Cr, Fe, and Mo, in the majority of cases, satisfactorily agreed with the mean values of the published data (see Table 1). The measurements of the cross sections for the (n, α) reaction on ^{65}Cu, ^{98}Mo, and ^{100}Mo do not confirm the well-known values. The cross sections of the reactions on ^{95}Mo were measured for the first time in this work.

LITERATURE CITED

1. N. Bormann, H. Neuert, and W. Scobel, in: Handbook on Nuclear Activation Cross Sections (1974), p. 87.
2. P. Cuzzocrea, E. Perillo, and S. Nottarigo, Nuovo Cimento, 4A, 251 (1971).
3. V. V. Sokol'skii, Thesis of the Reports of the Second All-Union Conference on Activation Analysis [in Russian], Tashkent (1968), p. 25.
4. D. Hume, Radiochemical Studies: The Fission Products, Paper 245, New York (1951), p. 1499.

NEW RUSSIAN JOURNALS

IN ENGLISH TRANSLATION

BIOLOGY BULLETIN

Izvestiya Akademii Nauk SSSR, Seriya Biologicheskaya

The biological proceedings of the Academy of Sciences of the USSR, this prestigious new bimonthly presents the work of the leading academicians on every aspect of the life sciences—from micro- and molecular biology to zoology, physiology, and space medicine.

Volume 7, 1980 (6 issues) $195.00

SOVIET JOURNAL OF MARINE BIOLOGY

Biologiya Morya

Devoted solely to research on marine organisms and their activity, practical considerations for their preservation, and reproduction of the biological resources of the seas and oceans.

Volume 6, 1980 (6 issues) $115.00

WATER RESOURCES

Vodnye Resursy

Evaluates the water resources of specific geographical areas throughout the world and reviews regularities of water resources formation as well as scientific principles of their optimal use.

Volume 7, 1980 (6 issues) $215.00

HUMAN PHYSIOLOGY

Fiziologiya Cheloveka

A new, innovative journal concerned *exclusively* with theoretical and applied aspects of the expanding field of human physiology.

Volume 6, 1980 (6 issues) $195.00

SOVIET JOURNAL OF BIOORGANIC CHEMISTRY

Bioorganicheskaya Khimiya

Features articles on isolation and purification of naturally occurring, biologically active compounds; the establishment of their structure, methods of synthesis, and determination of the relation between structure and biological function.

Volume 6, 1980 (12 issues) $245.00

SOVIET JOURNAL OF COORDINATION CHEMISTRY

Koordinatsionnaya Khimiya

Describes the achievements of modern theoretical and applied coordination chemistry. Topics include the synthesis and properties of new coordination compounds; reactions involving intraspheral substitution and transformation of ligands; complexes with polyfunctional and macromolecular ligands; complexing in solutions; and kinetics and mechanisms of reactions involving the participation of coordination compounds.

Volume 6, 1980 (12 issues) $255.00

THE SOVIET JOURNAL OF GLASS PHYSICS AND CHEMISTRY

Fizika i Khimiya Stekla

Devoted to current theoretical and applied research on three interlinked problems in glass technology; the nature of the chemical bonds in a vitrifying melt and in glass; the structure-statistical principle; and the macroscopic properties of glass.

Volume 6, 1980 (6 issues) $145.00

LITHUANIAN MATHEMATICAL JOURNAL

Litovskii Matematicheskii Sbornik

An international medium for the rapid publication of the latest developments in mathematics, this quarterly keeps western scientists abreast of both practical and theoretical configurations. Among the many areas reported on in depth are the generalized Green's function, the Monte Carlo method, the "innovation theorem," and the Martingale problem.

Volume 20, 1980 (4 issues) $175.00

PROGRAMMING AND COMPUTER SOFTWARE

Programmirovanie

Reports on current progress in programming and the use of computers. Topics covered include logical problems of programming; applied theory of algorithms; control of computational processes; program organization; programming methods connected with the idiosyncracies of input languages, hardware, and problem classes; parallel programming; operating systems; programming systems; programmer aids; software systems; data-control systems; IO systems; and subroutine libraries.

Volume 6, 1980 (6 issues) $115.00

SOVIET MICROELECTRONICS

Mikroelektronika

Reports on the latest advances in solutions of fundamental problems of microelectronics. Discusses new physical principles, materials, and methods for creating components, especially in large systems.

Volume 9, 1980 (6 issues) $160.00

Send for Your Free Examination Copy

PLENUM PUBLISHING CORPORATION, 227 West 17th Street, New York, N.Y. 10011
In United Kingdom: 88/90 Middlesex Street, London E1 7EZ England
Prices slightly higher outside the U.S. Prices subject to change without notice.